M.Sc. Fernando Otaviano Campos

Modeling Atrial Activation Sequences in the Rabbit Heart in Macroscopic and Microscopic Dimensions

DISSERTATION

in partial fulfillment of the requirements for the degree of
Doktor der Technischen Wissenschaften

Submitted to the

Graz University of Technology

Univ.–Prof. Dipl.–Ing. Dr.techn. Paul Wach
Institute of Medical Engineering
Graz University of Technology

Ao. Univ.–Prof. Dipl.–Ing. Dr.techn. Ernst Hofer
Institute of Biophysics
Medical University of Graz

Graz, May 21th 2012

Abstract

Severe atrial conduction disturbances are the most common arrhythmias in the elderly population. The heart undergoes a remodeling process with normal aging. Among all age related changes, increased fibrosis, which alters cardiac structure and the excitation spread at a microscopic scale, may play an important role in the genesis of atrial flutter (AFL) and fibrillation (AF). Research on the atrial electrical activation sequence comprising microstructural aspects of fibrosis is therefore of great interest. This thesis is focused on the modeling and simulation of the electrical excitation spread in the right atrial isthmus which is seen as a critical region for AFL and AF. The computer models are based on signals from electrophysiological *in vitro* experiments with Rabbit hearts and on histological tissue samples provided by cooperating research groups. Simulating cardiac excitation spread with realistic ion kinetics and in microscopic details is a very challenging task due to the tremendous computational effort involved. In this work, state of the art kinetic models for atrial cells and meshing techniques were employed to build up tissue models in the range of some centimeters in 2D and for some aspects of 3D. In addition to that, a new method to accelerate the simulations using graphic-hardware has been implemented. The computer models were employed to study and elucidate some key questions of electrophysiological mechanisms. It could be shown that superfusion technique with oxygenated solution is an adequate experimental protocol for studying the spread of depolarization in thin-walled tissue preparations. The structure-related computer models developed here allowed to investigate the impact of macro- and microstructures on depolarization waveforms at the surface of the tissue. The microscopic model showed in detail the directional dependence of electrogram morphology in regions representing different types of microstructures. These findings can be used to discriminate different classes of fibrosis. The implementation of a numerical solver to simulate cardiac cellular dynamics on graphics processing units (GPUs) outperformed the parallel implementations of the same algorithm on a small cluster of computers. The results of this work can be seen as a promising step towards whole heart simulations performed at relatively low costs compared to high performance computing facilities.

Keywords:
Cardiac electrophysiology, Computational modeling, Extracellular potentials, High performance computing

Zusammenfassung

Atriale Überleitungsstörungen zählen zu den häufigsten Herzrhythmusstörungen im fortgeschrittenen Lebensalter. Die mit dem normalen Alterungsprozess einhergehende zunehmende Fibrose verändert Mikrostruktur und mikroskopische Erregungsausbreitung und ist möglicherweise Auslöser für Vorhofflattern und -flimmern. Die Erforschung der atrialen elektrischen Aktivierungssequenz im Zusammenspiel mit mikrostrukturellen Aspekten der Fibrose ist daher von großem Interesse. Im Mittelpunkt dieser Dissertation stehen die Modellierung und Simulation der elektrischen Erregungsausbreitung im rechtsatrialen Isthmus, welcher als kritische Region das Entstehen von Vorhofflattern und -flimmern betrachtet wird. Die verwendeten Computermodelle basieren auf Signalen von *in vitro* Experimenten mit Hasenherzen und auf histologischen Gewebeschnitten, die von kooperierenden Forschungsgruppen bereitgestellt wurden. Die Simulation der elektrischen Herzerregung mit realistischer Ionenkanal-Kinetik unter Einbeziehung mikroanatomischer Details ist mit enormem Rechenaufwand verbunden. In dieser Arbeit wurden „state of the art" Kinetikmodelle atrialer Zellen und Finite Element-Netzgenerierungstechniken eingesetzt, um zwei- und dreidimensionale Gewebemodelle von wenigen Zentimetern Größe aufzubauen. Darüber hinaus wurde eine alternative Methode zur Beschleunigung der Rechenzeiten mittels Grafikprozessoren entwickelt. Die Computermodelle wurden eingesetzt, um einige wichtige Fragestellungen zu elektrophysiologischen Mechanismen zu studieren. Es konnte gezeigt werden, dass die Überströmung mit oxigenierter Nährlösung ein adäquates experimentelles Protokoll zur Erforschung der Signalweiterleitung in dünnwandigen Gewebepräparaten darstellt. Die neu entwickelten mikroskopisch detailgetreuen Computer-Modelle erlauben die Untersuchung des Einflusses von Makro- und Mikrostrukturen auf Depolarisationssignale an der Oberfläche von Geweben. Im Besonderen konnte mit dem Modell die Richtungsabhängigkeit der Elektrogramm-Morphologie in verschiedenen Regionen gezeigt werden. Diese Befunde können verwendet werden, um verschiedene Klassen von Fibrose zu charakterisieren. Die Implementierung eines numerischen Lösungsverfahrens für kardiale zelluläre Dynamik auf Graphikkernen (GPUs) übertrifft geschwindigkeitsmäßig die parallel-programmierte CPU Implementierungen des gleichen Algorithmus. Die Ergebnisse dieser Arbeit können als ein vielversprechender Schritt in die Richtung von Ganzherz-Simulationen gesehen werden, durchgeführt bei relativ niedrigen Kosten im Vergleich zu Hochleistungsrechnern.

Schlagwörter:

Statutory Declaration

I declare that I have authored this thesis independently, that I have not used other than the declared sources / resources and that I have explicitly marked all material which has been quoted either literally or by content from the used sources.

....
date

....
signature

Acknowledgments

Contents

List of Figures

List of Tables

List of Abbreviations

ADP	adenosine diphosphate concentration
AF	atrial fibrillation
AFL	atrial flutter
AP	action potential
APD	action potential duration
APD_{90}	action potential duration at 90% of repolarization
ATP	adenosine triphosphate
AVN	atrioventricular node
BCL	basic cycle length
bpm	beats per minute
BZ	border zone
CARP	cardiac arrhythmia research package
CFAE	complex fractionated atrial electrogram
CHF	congestive heart failure
CIZ	central ischemic zone
CNF	cardiac near field
CP	observation point
CPU	central processing unit
CS	coronary sinus
CT	crista terminalis
CV	conduction velocity
DT-MRI	diffusion tensor magnetic resonance imaging
ECG	electrocardiogram
FE	finite element
FI	fractionation index
GHK	Goldman-Hodgkin-Katz
GPU	graphic processing unit
HSL	saturation and lightness
IVC	inferior vena cava
LA	left atrium

LAT	local activation time
LCV	local conduction velocity
LDA	linear discriminant analysis
LOOM	leave-one-out method
LCV	local conduction velocity
LV	left ventricle
MSH	Mahajan-Shiferaw
NZ	normal zone
ODE	ordinary differential equation
PDE	partial differential equation
PM	pectinate muscle
RA	right atrium
ROI	region of interest
RV	right ventricle
SAN	sinoatrial node
SR	sarcoplasmic reticulum
STIM	stimulus
STV	septum tricuspidal valve
SVC	superior vena cava
TMF	time of maximum field
UAE	uniform atrial electrogram
UCMO	uncoupled tissue with multidirectional arrangement of uncoupling structures
UCPO	uncoupled tissue with uncoupling structures oriented parallel to the cardiac fibers
VE	vestibule
WCDP	well coupled densely packet tissue

Chapter 1

Introduction

Atrial conduction disturbances such as atrial flutter (AFL) and atrial fibrillation (AF) are the most common tachyarrhythmias in adults, particularly in the elderly population.[13] It is well known that the cardiac histology undergoes a considerable remodeling with growing age due to the formation of fibrotic connective tissue, which in turn influences physiological properties as well as the electrical propagation.[14–16]

Fibrosis can separate adjacent myocardial bundles electrically over large lengths, leading thus to a discontinuous conduction between neighboring bundles. These discontinuities may become a substrate for slow conduction, since they form complex pathways which in turn delay the electrical activation. At the endocardial surface, this change in conduction turns uniform atrial electrograms (UAEs) into complex fractionated atrial electrograms (CFAEs), which have been used as potential targets for catheter-based AF ablation procedures.[17,18]

The lateral and posterior part of the lower right atrium (RA) is seen as critical substrate for the genesis of intermittent* block of conduction and, occasionally, it is the target for catheter ablation.[19] This region of interest (ROI) exhibits a large range of macro structures (cable-like bundles, branchings, crossings, junctions), thus posing a significant technological challenge for experimental techniques. Moreover, recent studies on the tissue matrix in several regions of the atria suggest, that excitation spread at a sub-millimeter size scale may differ substantially from activation maps taken from clinical recordings at a coarser size scale.[19–21] Histological examinations of the ROI revealed an overwhelming diversity of microstructural topologies, which may function as conduction barriers in patients with AFL.[19] However, clinical mapping systems capable of resolving activation sequences in the sub-millimeter range are not available at the moment.

In isolated animal heart preparations, *in vitro* experimental ultra-high resolution techniques, such as the cardiac near field (CNF) measurement, may be suited to study macro-

---

*Marked by intervals of complete quietude occurring between two periods of activity.

as well as micro-propagation of the cardiac electrical impulse[*] in the ROI.[22] However, limitations in the experimental protocols, such as the use of superfusion with oxygenated solutions, could lead to misinterpretation of the results.

Mathematical models have been widely used to study the behavior of the electrical propagation at a sub-cellular[†] level and its relation with cardiac arrhythmias.[4,16,23–25] In such approaches, the structural complexity can be varied step by step starting from the endocardial macro anatomy[‡] with appropriate anisotropic properties corresponding to the respective fiber directions. Subsequently, microscopic details (average size of $315\,\mu$m)[16] can be added by introducing barriers of conduction at a size scale found in histological images. The downside of the latter approach is that very fine and computationally expensive meshes are required to capture all microscopic details found in the cardiac tissue.

This thesis is focused on different aspects within the modeling of the electrical activity in the rabbit right atrial isthmus. Macro and micro activation sequences, cell electrophysiological parameters and depolarization signals measured at the endocardial surface have been investigated. As a preliminary study, a radially symmetric model representing a thin muscle bundle ($1\,$mm diameter) from the ROI was established. The model aimed to quantify possible limitations of the use of superfusion as a method to provide the tissue with proper oxygen supply and waste removal. More specifically, to quantify the impact of superfusion-induced heterogeneities occurring in the depth of the tissue upon impulse propagation in superficial layers.

Subsequently, 2D models of the ROI were developed with two different levels of details, a less detailed model which accounts for the visible macrostructure only, and a very detailed model which takes into account all microstructural heterogeneities found in serially section histographs[§]. The histologically detailed model was used to determine how the microstructural organization of fibrosis in the ROI correlates with fractionation of electrograms and the CNF. The tissue model was paced in different virtual sites and directional effects of wavefronts on electrogram morphology were analyzed in different atrial regions representing three types of microstructure:

- Well coupled densely packed tissue

- Uncoupled tissue with uncoupling structures oriented parallel to the cardiac fibers

- Uncoupled tissue with multidirectional arrangement of uncoupling structures

Finally, the computational cost of simulations using the models proposed here is high due to the spatio-temporal characteristics of electrical impulse propagation in cardiac

---

[*]In electrophysiology, an "electrical impulse" is the response to an external stimulus (applied current).

[†]This scale corresponds to a cell length ($< 0.1\,$mm).

[‡]This scale accounts for visible anatomical structures ($> 0.1\,$mm).

[§]High-resolution images showing the microscopic anatomy of thin slices of tissue.

tissue. Large systems of equations have to be solved thousands of times in order to simulate a single heart beat. The adoption of parallel computing have relaxed the constraints of the use of very detailed *in silico* models of the heart.[26,27] However, access to high performance computing centres are usually restricted to a number of research groups, and local computer clusters with high end CPUs are still pricey to build and maintain. New computing paradigms are currently being discussed as an alternative to the classical CPU computing. Among them, the graphical processing unit (GPU) is of particular interest in this thesis. The demand for real-time high-definition 3D graphics turned the GPUs into highly parallel processors with tremendous computational power[*]. This parallel computing paradigm is a promising alternative to solve the models proposed in this work. Thus, the performance of a GPU solver to accelerate the simulations of the atrial electrical activity was also evaluated.

The rest of this thesis is structured as follows: chapter 2 provides the necessary foundations of the conduction in the right atrial isthmus. In chapter 3, a short overview of cardiac modeling is given. Chapter 4 introduces the methods that were employed for the development and simulations of all macro- and microscopic models. Chapter 5 presents and discuss the results of all modeling and simulation studies. The thesis concludes with a summary and an outlook on possible future work in chapter 6.

---

[*]Today GPUs have up to 30 multiprocessors per graphics chip with peak performance of about 1 TFLOPS (floating-point operations per second).

Chapter 2

Basic Foundations

This chapter aims to provide the physiological foundations necessary for most of the technical explanations following hereafter. The description regarding the electrical conduction in the right atrial isthmus (epidemiological aspects, clinical aspects, anatomy, electrophysiological basics and histology) was restricted to the essential minimum. However, references on more specialized literature to which the interested reader is kindly referred. Finally, the need of very detailed computer models of the heart is discussed, and a brief overview of the state of the art in modeling excitation spread in atrial tissue is also given.

2.1   Basic Physiology of the Heart

The function of the heart is to transport blood throughout the body delivering oxygen and nutrients required by the cells. The heart of rabbits, the species considered in this thesis, possess the typical anatomy of a mammal with two atria and two ventricles (Fig. 2.1). When the cardiac muscle contracts (systole), blood is pumped out of the heart. This process is divided into two stages: initially, the atria contract at the same time pumping blood into the ventricles. Then the ventricles, which have a greater ability to contract, pump blood out of the heart. After this process, the heart muscle relaxes (diastole) before contracting again. The right and left sides of the heart have different functions. The right side collects blood low in oxygen and sends it to the lungs. The left side receives blood rich in oxygen from the lungs and sends it to the whole body. Fig. 2.1 illustrates this process. A complete and detailed anatomical description of the heart is outside the scope of this thesis. The interested reader is referred to Guyton and Hall[1] for further details.

The contraction of the heart is preceded by an electrical discharge within each cell of the cardiac muscle (myocytes). For the heart to function as a pump, the myocytes in the ventricles must contract shortly after the atria. This timing is obtained through the propagation of electrical impulses, which act as messages between cardiac cells. The spread of
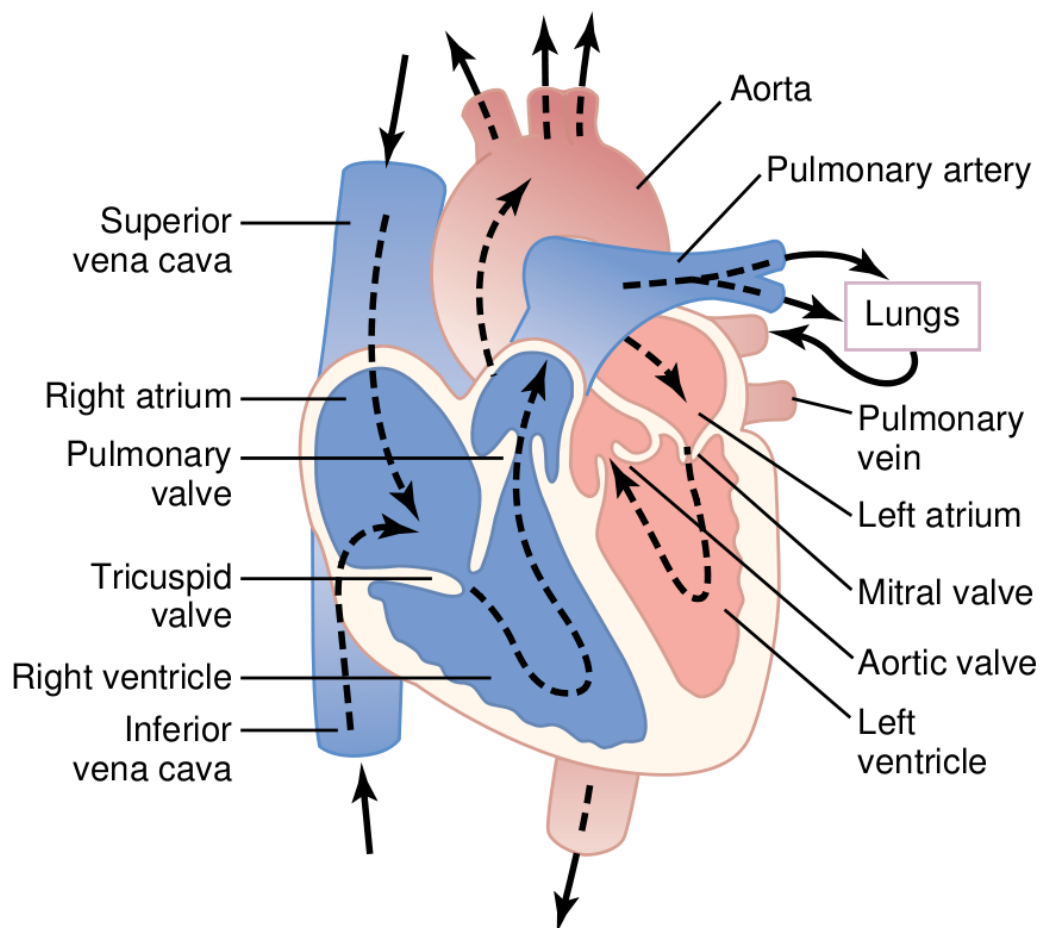
Figure 2.1: Structure of the heart. Blood flow through the chambers and heart valves. Figure extracted from Guyton & Hall.[1]

the depolarization* wave is initiated and controlled by a specific group of myocytes that possess the ability to generate regular electrical impulses. The region responsible for this "pacemaker" activity is called the sinoatrial node (SAN) and is located on the wall of the right atrium (RA), near the entrance of the superior vena cava (SVC). The electrical impulse generated in the SAN is transmitted into the right and left atria (via the Bachmann's bundle), but not to the ventricles due to non-conducting fibrous tissue found in the interventricular septum. It travels further to the atrioventricular node (AVN) where it is delayed to prevent the atria and ventricles to contract at the same time. Finally, the electrical impulse is propagated down the ventricles through the specialized excitation conduction system formed by the bundle of His and the Purkinje fibers.[28] Under normal conditions, this process is repeated several times causing rhythmic beats of approximately 80 beats per minute (bpm) in humans and 130 bpm in rabbits.

---

*In biology, depolarization is a change in potential across the cell membrane, making it more positive.

2.1.1 Atrial Conduction Disturbances

Abnormal generation and conduction of electrical impulses may result in arrhythmias and irregular contractions that can lead to death. For instance, sometimes the contraction of the atria is not coordinated with the the ventricles, in such cases the atria no longer work as primer pumps for the ventricles.

Severe atrial conduction disturbances, namely atrial flutter (AFL) and atrial fibrillation (AF), are the most common arrhythmias contributing substantially to cardiac morbidity and mortality, particularly in the elderly population.[2,13] In AFL, the electrical impulse travels as a single large wave always in one direction around and around the atrial muscle.[1] AFL causes a rapid rate of contraction of the atria, but since one side of the atria is contracting while the other side is relaxing, the amount of blood pumped to the ventricles is slight.[1] AF, on the other hand, is characterized by rapid and chaotic activation of the atrium.[2] In AF, as shown in Fig. 2.2, the normal electrical impulses are overwhelmed by disorganized focal ectopic electrical impulses that originate in areas other than the SAN. This leads to conduction of irregular impulses to the ventricles that generate the heartbeat.[2] A brief period of AF may cause palpitations, chest discomfort and light-headedness. Sustained AF, on the other hand, can cause severe congestive heart failure* (CHF) after several weeks to months. The loss of atrial contraction also leads to stasis of blood in the atria, which promotes clot formation increasing the risk of stroke.[2]
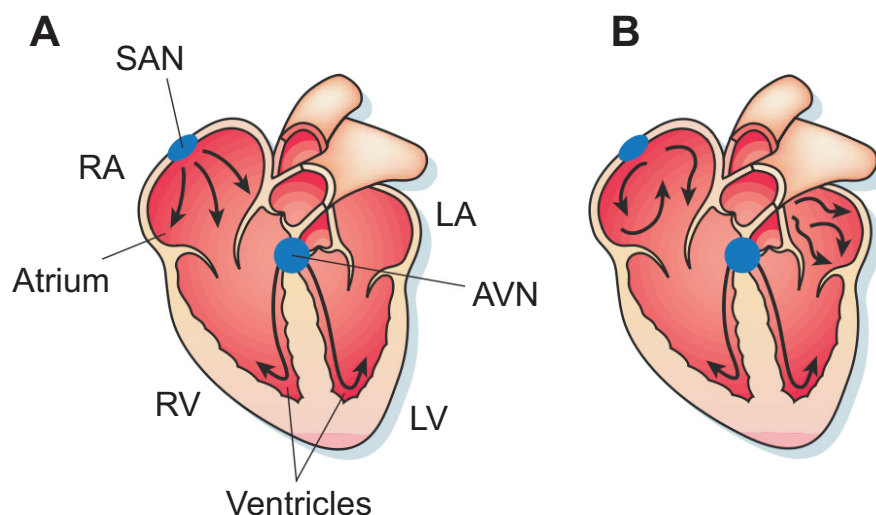
Figure 2.2: Diagram of electrical conduction in the heart. (A) Normal rhythm. Showing the sinoatrial node (SAN), right atrium (RA), right ventricle (RV), left atrium (LA), atrioventricular node (AVN) and left ventricle (LV). (B) Atrial fibrillation. Figure adapted from Nattel.[2]

Cardiac arrhythmias have been treated traditionally with antiarrhythmic drugs that

---

*Heart failure, also called congestive heart failure, is a condition in which the heart can no longer pump enough blood to the rest of the body.

control the heart rhythm by altering cardiac electrical properties. However, the available drugs are not specific for atrial electrical activity and can have profound effects on ventricular electrophysiology. The effects of such antiarrhythmic drugs can themselves paradoxically lead to life-threatening rhythm disorders increasing mortality.[29] There has been, therefore, a shift towards non-pharmacological therapies for atrial arrhythmias, such as controlled destruction of arrhythmia-generating tissue via catheter ablation therapy. Nonetheless, the success rates of ablation procedures for AF are still low, particularly in aged patients: for paroxysmal* AF, the 5-year single procedure success rate is 60% whereas the multiple procedure success rate is 80% (average 2 procedures). This rate is even lower in the case of persistent† AF being about 30-50% after 1 and 50-87% after multiple procedures (information kindly provided by M.D. Daniel Scherr‡). AF nowadays affects 2.2 million U.S. citizens, 6% of the population elder than 65 years suffer from AF.[13] This number will have increased to 5.6 million by the year 2050.[30] A detailed mechanistic exploration of intra-atrial conduction and its disturbances comprising age-related functional and structural aspects is therefore of increasing interest for basic researchers as well as for clinical electrophysiologists.

2.1.2 The Right Atrial Isthmus - The Region of Interest (ROI)

The lateral and posterior part of the lower RA has been identified as a critical link for the macro-reentrant circuit of isthmus-dependent AFL as well as AF and, is the target of catheter ablation techniques that have become the treatment of choice for these arrhythmias.[19, 21]

The right atrial isthmus forms a network of cable-like muscle bundles comprising the ramifications of the crista terminalis (CT), pectinate muscles (PMs) and the tricuspidal valve vestibule (VE). In a healthy heart, the electrical impulse generated in the SAN propagates onto the CT, spreading then to the PMs until the VE. This region of interest (ROI) exhibits a large range of macro structures (cable-like bundles, branchings, crossings and junctions) and, is seen as critical substrate for the genesis of intermittent block of conduction close to the junction of CT and PMs[20] (see Fig. 2.3).

Recent histo-anatomical studies provided detailed data on the cellular composition of the tissue matrix in several regions of the atria.[19–21, 31] In rabbit hearts, macro morphological discontinuities may arise within distances smaller than 1 mm (see Fig. 2.4 A). Beyond this, at a microscopic level, complexity is exceeded by far as shown in Fig. 2.4 B. At this level, particularly in the aged heart, connective tissue structures§ underneath the

---

*Recurrent episodes that self-terminate in less than 7 days.

†Recurrent episodes that last more than 7 days.

‡Hôpital de Haut-Lévèque, Bordeaux, France.

§An adverse accumulation of connective tissue (fibrosis) compromises tissue stiffness and separates adjacent myocardial bundles electrically.

endocardium may disrupt the electrical coupling network of myocytes within distances of 90 to 830 μm.[16] Extensive preliminary data obtained by spatio-temporally high resolution recordings in the ROI suggest that conduction patterns observed at the microscopic size scale are strikingly different from those expected from a macroscopic (clinical) point of view. The overwhelming diversity of microstructural topologies found in the ROI may play an essential role in normal and abnormal conduction. Consequently, the ROI is an ideal substrate to examine mechanisms of conduction at the macroscopic as well as at the microscopic level in order to explain discrepancies found between expected (clinical macro-view) and the biophysically underlying conduction patterns that actually occur in the tissue.
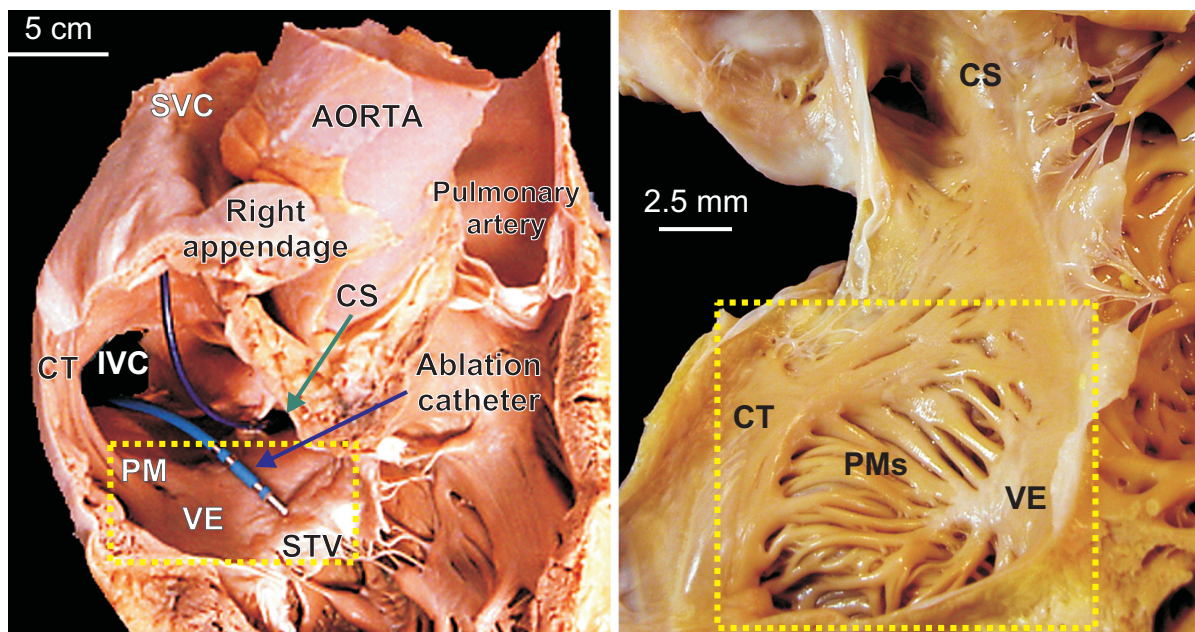
Figure 2.3: The human right atrium (RA). (A) Open RA showing an ablation catheter in the region of interest (ROI) assigned with an yellow rectangle: superior vena cava (SVC), inferior vena cava (IVC), crista terminalis (CT), pectinate muscle (PM), vestibule (VE), septum tricuspidal valve (STV) and coronary sinus (CS). (B) Detailed view on the pectinate muscle ensemble. Figure kindly provided by Dr. Damián Sánchez-Quintana[¶].
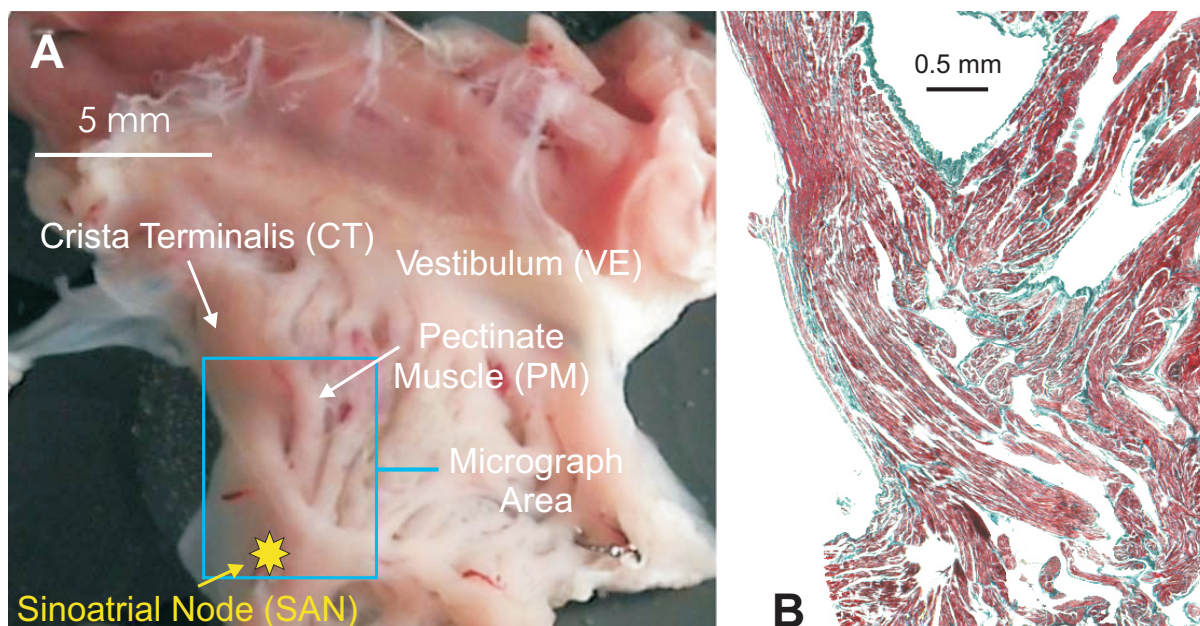
Figure 2.4: The rabbit right atrial isthmus. (A) Macro-image of the region of interest (ROI). (B) High resolution histological image of the selected area. The staining (Masson's trichrome) resulted in a coloring of myocytes (red), connective tissue (blue) and interstitial cleft spaces (white). Figure adapted from Hofer *et al.*[3]

2.2 Cardiac Electrophysiology

Myocytes, as any living cell, have their inside delimited by a selectively permeable membrane that controls the flow of substances into and out of the cytoplasm. The membrane consists of a double layer (a bilayer) of phospholipid molecules, which maintain an ambivalent relationship with the water. Both the intracellular and extracellular environments consist of, among many other things, a dilute aqueous solution of dissolved salts, primarily NaCl and KCl, which dissociate mainly into Na^+, K^+ and Cl^- ions. The cell membrane acts as a barrier to the free flow of these ions, maintaining thus concentration differences between the two environments.[32]
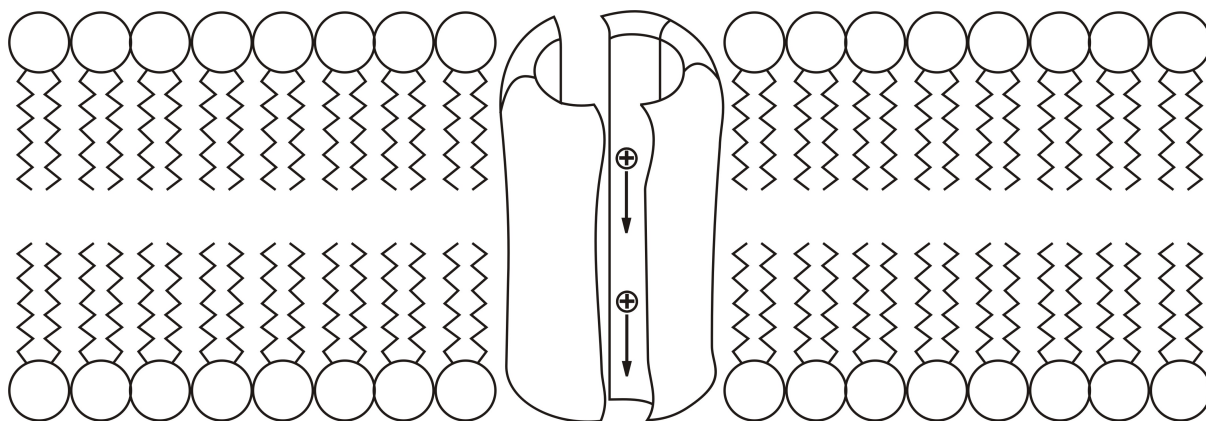
Figure 2.5: Schematic diagram of the cell membrane containing an ionic channel.

Molecules can be transported across the membrane by active or passive processes. The former requires energy expenditure, while the latter is the result of inherent random movement of molecules. The water and other substances such as oxygen and carbon dioxide cross the phospholipid bilayer by passive processes (osmosis and facilitated diffusion). Sodium and potassium ions, however, pass through ion-specific channels driven by diffusion and electrical forces.[32] Fig. 2.5 shows a schematic view of how proteins form channels through which ions can pass. The channels are specialized structures that exhibit a high degree of selectivity. Differences in the concentrations are created and maintained by active mechanisms that use energy to pump ions against the concentration gradient. One of the most important of these processes is the Na^+-K^+ pump, which uses energy stored in the form adenosine triphosphate (ATP) molecules to pump Na^+ out of the cell and to capture K^+ from the external environment. Differences in ionic concentrations create a potential difference across the membrane, the transmembrane potential, that drives ionic currents in and out of the cell.

Cardiac myocytes belong to the group of electrically excitable cells. In this type of cells, if an external stimulus in the form of an applied current is sufficiently strong, the

membrane potential* (V_m) goes through a large excursion, called action potential (AP), before eventually returning to rest. The most obvious advantage of excitability is that an excitable cell either responds in full to a stimulus or not at all, and thus a stimulus of sufficient amplitude may be reliably distinguished from background noise. In this way, noise is filtered out, and a signal is reliably transmitted.[32]

The amplitude of the AP in rabbit ventricular myocytes, like shown in Fig. 2.6 A, is about 125 mV, which means that the intracellular potential rises from a very negative value, about -85 mV, between beats to about +40 mV (*overshoot*), during each beat. The rise in the transmembrane potential (depolarization phase) is caused mostly by the opening of large numbers of so-called fast sodium channels. These channels are called "fast" channels because they remain open for only a few thousandths of a second and then close. After the initial spike, (the *upstroke*) the membrane remains depolarized for about 250 ms exhibiting a *plateau* as illustrate in Fig. 2.6 A. This phase is characterized by an entirely different population of slow calcium channels. These channels are slower to open and, even more important, remain open for a longer period. During this time, a large quantity of Ca^{2+} ions flows through these channels to the interior of the cardiac cell maintaining a prolonged period of depolarization (the plateau). Further, the Ca^{2+} ions that enter during this phase activate the muscle contractile process. Finally, the repolarization follows the end of the plateau. In this last phase, the permeability for potassium ions increases rapidly; this rapid loss of K^+ from the cytoplasm combined with the close of the Ca^{2+} channels returns the membrane potential to its resting level, thus ending the AP.
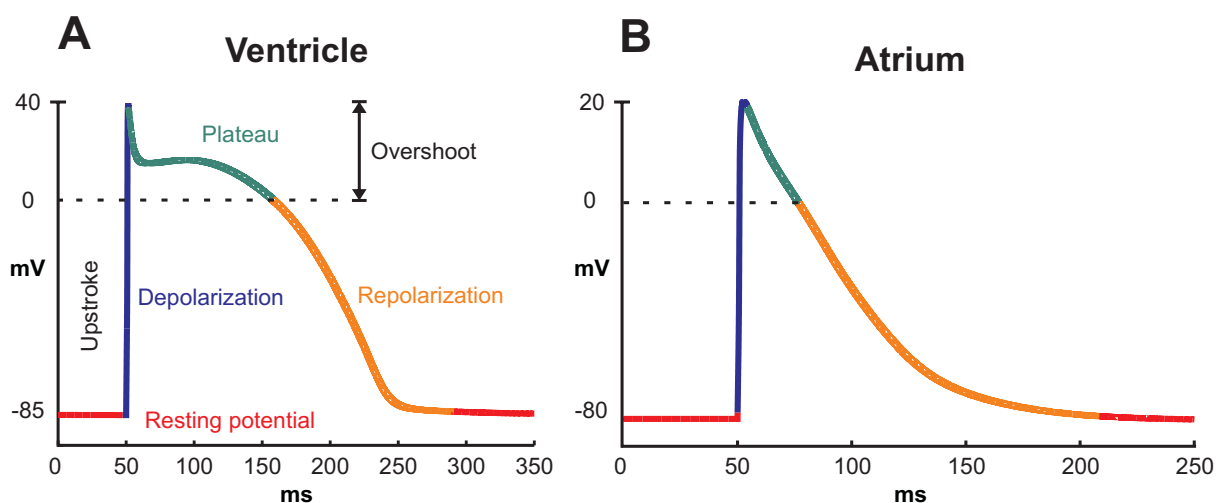
Figure 2.6: Morphology of the action potential in rabbit (A) ventricular and (B) atrial myocytes.

---

*Membrane potential (or transmembrane potential) is the potential difference between the interior and exterior of a cell.

The AP from the rabbit atrium, as shown in Fig. 2.6 B, has a rather triangular morphology when compared to the ventricular AP (Fig. 2.6 A). The AP has a rapid upstroke, a modest plateau, and a noticeable increase in repolarization velocity during late repolarization. Shortly, the AP has a smaller amplitude when compared to the ventricular, averaging about 100 mV. Intracellular potential rises from about -80 mV to a slightly positive value, about +20 mV, during each beat. The rise in the transmembrane potential is also caused by the opening of large numbers of fast Na^+ channels as well as by particular calcium channels. The latter population of channels differs from the former in number and kinetics, providing thus only a tiny contribution to the AP upstroke. The membrane remains depolarized for about 100 ms exhibiting a modest plateau. The end of the plateau is followed by a long "tail" representing the repolarization phase.

2.2.1   Electrophysiological Heterogeneities

It is commonly accepted that some of the ion channels involved in the formation of the AP have heterogeneous densities or biophysical properties throughout the cardiac tissue (usually referred as functional heterogeneities).[33–35] The RA is characterized by significant heterogeneities in AP morphology, which are due to variations in the density of several ionic currents.[36–38] A gradient of AP morphology with the longest action potential duration (APD) near the SAN and decreasing along the ROI has been reported.[4,36] Fig. 2.7 illustrates the differences in AP waveform in the ROI of the rabbit. Furthermore, changes in the physiological configuration of heterogeneities can facilitate the formation of a substrate that could trigger arrhythmogenic events.[39]
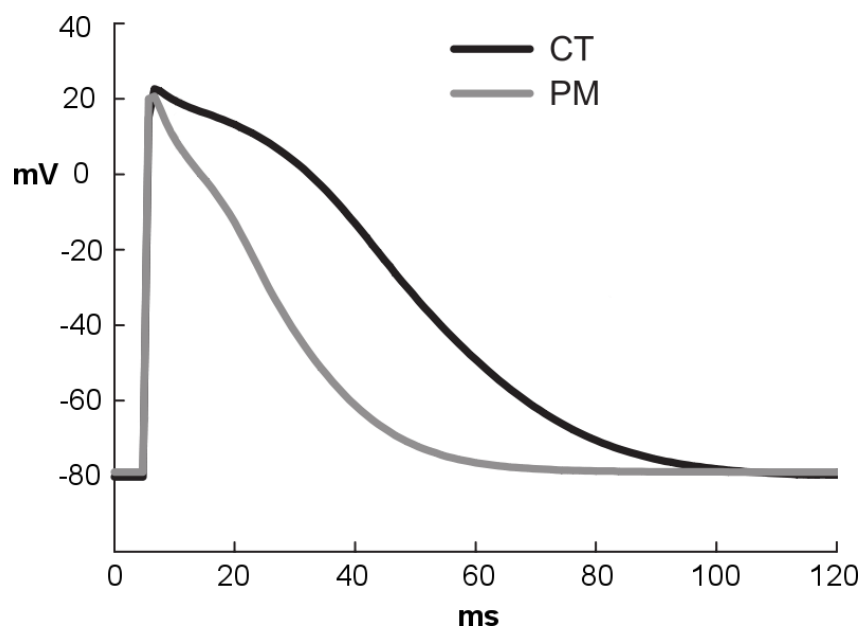
Figure 2.7: APs recorded in experiments with myocytes from the rabbit crista terminalis (CT) and pectinate muscle (PM). Figure adapted from Aslanidi *et al.*[4]

The relationship between the macrostructure (structural heterogeneities) of the RA (CT and PM bundles) and conduction block leading to AF in the RA has long been recognized.[40,41] On one hand, several intracardiac echocardiography studies have suggested that atrial arrhythmias are related to the endocardial anatomy of the CT.[42] On the other hand, it has been proposed that differences in repolarization times in the canine RA gave rise to block and provided a substrate for generation of arrhythmias.[39] Therefore, functional as well as structural inhomogeneities have to be considered in any study concerning electrical conduction in the ROI.

2.3 Electrical Excitation Spread

It is known from electron microscopic studies that cardiac cells are arranged in a brick-like structure. Each myocyte is somewhat cylindrical in shape and roughly $100\,\mu$m long and $15\,\mu$m in diameter.[8] Fig. 2.8 depicts how cardiac muscle fibers are arranged in a latticework. In this representation, the fibers are dividing, recombining, and then spreading again. The intercalated discs (dark areas crossing the myofibers in Fig. 2.8) separate individual myocytes from one another. That is, cardiac muscle fibers are made up of many individual cells connected in series and in parallel with one another.[1]
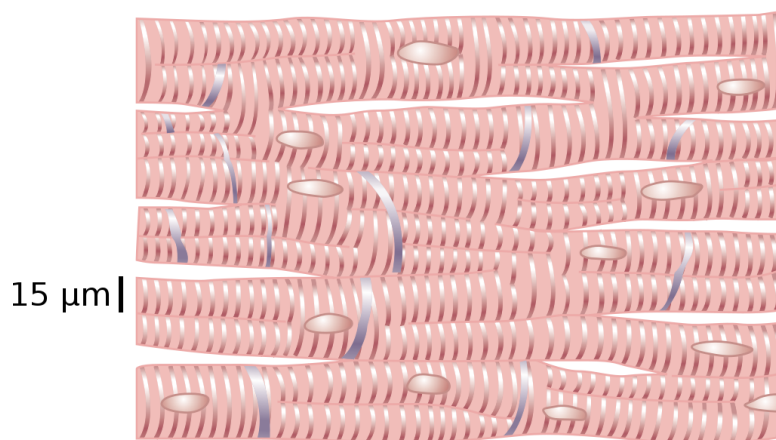
Figure 2.8: Interconnected cardiac muscle fibers. Figure extracted from Guyton & Hall.[1]

At each intercalated disc, the cell membranes connect to one another through special proteins called gap junctions, which provide cell-to-cell transfer of ions and hence electric current. Thus, the AP can travel from one myocyte to the next with ease along the longitudinal axes of the fibers. Since these junctions are mostly located at the ends of the cells and more sparsely along their length, electrical conduction is faster in the fiber axial direction than across the fiber axis. Therefore, the cardiac tissue is strongly anisotropic, with wave speeds that differ substantially depending on their direction. For example, in human myocardium, propagation is about $0.5\,$m/s along fibers and about $0.17\,$m/s transverse to fibers.[32]

2.3.1 Activation Sequences - A Question of Scaling

The cardiac depolarization process and its propagation represented as electrical activation sequences can be seen in different spatial scales ranging from the whole organ down to the subcellular level. Electrical impulse propagation in cardiac tissue is the result of a well-orchestrated interplay of many factors, such as cell excitability, coupling between myocytes and conduction pathways predefined by the macro- and micro anatomies. Perturbations of any of these functional or structural factors may have detrimental effects on the cardiac electrical activation sequence. As a result, zones of slow conduction may appear due to complex activation patterns, increasing the risk of life threatening arrhythmias. Furthermore, it is widely accepted, that impulse conduction, when observed at a microscopic size scale, is always complex and discontinuous by nature,[43] even under normal conditions in perfectly healthy tissue. The discreteness of propagation at this size scale, however, does not have a noticeable signature at a coarser size scale. Under pathological conditions, on the other hand, microscopic conduction disturbances may become severe enough to influence the activation pattern on the macro scale, which may lead to a noticeable impairment of the organ function. Consequently, impulse propagation has to be seen at different scales:[44]

1. A **"global" size scale** describing activation sequences in whole heart or in one of its chambers, the RA for instance. This size scale corresponds to the clinical perspective, which falls in the centimeter range and disregards fine and complex architecture of fibers.

2. A **macroscopic size scale** characterizing propagation along and within the visible macro anatomical structures (like the CT and PMs) in a range $> 1\,\mathrm{mm}$.

3. A **microscopic size scale** that describes conduction of APs within and between groups of fibers in the submillimeter range ($0.1 - 1\,\mathrm{mm}$).

4. A **subcellular size scale** elucidating the transfer of excitation within and between myocytes through gap junctions ($< 0.1\,\mathrm{mm}$).

Since conduction mechanisms may differ substantially depending on at which size scale the processes are contemplated (continuous syncytial conduction versus discrete and discontinuous conduction), a decision has to be made which size scale is the most appropriate for a particular question. In this thesis, the focus of investigation lies on the size scales 2 and 3, since it can be expected that most age-related structural modifications occur at this size scale by fibrotic processes.

2.3.2   Mapping of Conduction

The propagation of the electrical wavefront in the heart is commonly measured by temporal and spatial recording of potentials resulting from cardiac current flow.[45] The electric field potential in the surrounding volume conductor arises from the cardiac current sources within the region. Thus, such potentials can be sampled outside cells, or even at a distance, without damage to the electrically active cells, or signal perturbation resulting from electrode penetration into the cardiac tissue.[8] Even body surface electrodes detect the small currents that flow as part of membrane depolarization deep within the torso volume. The electrocardiogram (ECG) is the most popular non-invasive diagnostic tool for assessing cardiac functionality. The ECG is an easy and helpful test for assessment of possible underlying problems. However, the results of an ECG examination are often unspecific, meaning that abnormal findings do not refer to one condition, but could be the result of different problems. Furthermore, a normal ECG does not rule out heart diseases. Therefore, additional tests, such as clinical diagnosis intracorporal methods, are recommended. Such methods allow a simplified spatial discrimination and deliver additional information. Hereby, potentials are measured within the cavities of the heart via multi-electrode catheters.[46] Extracellular electrograms, recorded directly at the endocardial surface, are the hallmarks of minimal invasive cardiac electrophysiology and provide information about the electric status of the underlying myocardium.[6]

Unipolar Extracellular Electrograms

Extracellular electrograms ϕ_e arise because of differences in local currents that occur due to a high potential gradient at the interface between depolarized ($+20\,$mV) and quiescent ($-85\,$mV) myocytes.[6] Fig. 2.9 illustrates the genesis of the extracellular field potential just above a cardiac muscle bundle (spatial distributions of potentials, depicted by + and - close to the cell membrane, refer to the time instant in which cells located at site B trigger an AP). Electrical activation (or depolarization) starts on the left end of the cardiac tissue as a result of an external applied current. The wavefront moves towards the opposite end causing an intracellular voltage gradient between depolarized and quiescent sites. The amplitude of the intracellular current is large at the position of the wavefront, as depicted by 2 large red arrows at site B in Fig. 2.9, due to the steep voltage gradient. At sites A and C, on the other hand, the gradient is less steep and thus, the current amplitudes are lower (depicted by sole small red arrows). Since the sum of the currents at any point of the tissue has to be zero, this implies that there must be an inward current flow across the cell membrane at the back of the wavefront, which is balanced by and an outward flow at its front. Note the orange arrows at the membrane pointing inward (mainly sodium I_{Na} current) and outward (potassium I_K currents) in Fig. 2.9. Thus, the depolarization front operates as a current dipole, which injects current into extracellular space at the front

and retrieves current from extracellular space at the back.[6] Current through extracellular space, which has electric resistance, generates an extracellular potential difference.
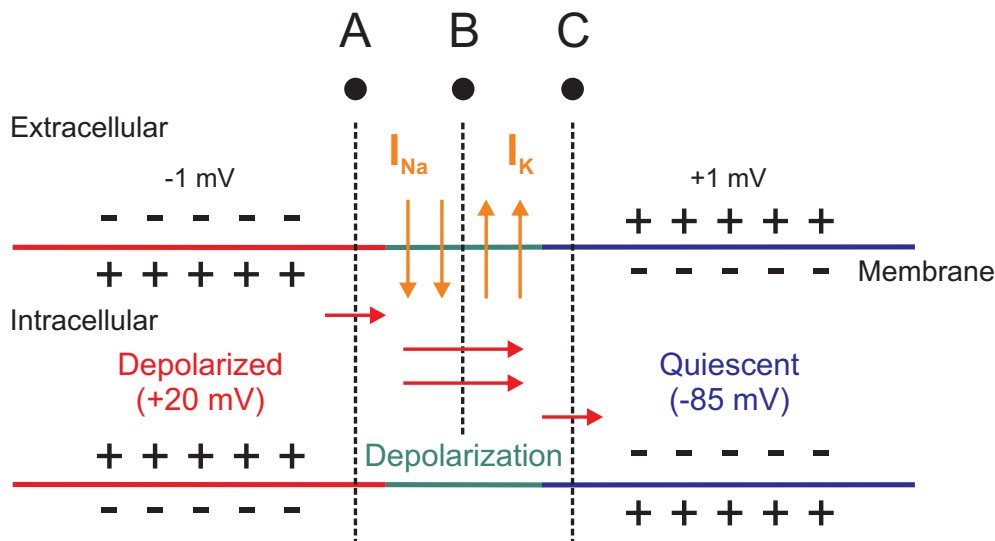
Figure 2.9: Schematic drawing of the genesis of the extracellular field potential caused by differences in local inward (I_{Na}) and outward (I_K) currents just above the cardiac tissue. The distribution of potentials (intra- and extracellular) are depicted by + and - close to the membrane. It corresponds to the activation time of myocytes located at site B (instant when the cells trigger an AP). The corresponding values of extracellular potentials just above the cell membrane have been determined by Spach *et al.*[5]

Extracellular potentials exhibit a biphasic morphology, being positive in front of the depolarization front, zero at the wavefront, and negative at the back of the depolarization front. A recording electrode positioned at a site where the electrical wavefront is passing will record an increasing potential when the front is approaching. The potential reaches a maximum when the depolarization front is very close to the recording site. Then, the potential rapidly decreases to zero and becomes negative with its minimum just as the wavefront has passed. Finally, the negative potential returns to zero as the wavefront proceeds. However, such biphasic morphology is only verified in the so called "free running signals", i.e., signals measured far from the ends of the myocardial bundle.[5] This is illustrated in Fig. 2.10, where ϕ_e was measured at sites where impulse conduction was initiated (A), free running propagating (B) and at the collision (C). In Fig. 2.10 B, the electrical wavefront is passing and a simple biphasic deflection is generated. At the left, where depolarization starts, there is no approaching wavefront and the local electrogram only has a negative deflection. At the far right, (C), the depolarization front collides. The recording site just faces the area with positive potentials and consequently the electrogram only has a positive deflection. Thus, in principle, the unipolar electrogram is simple and comprises only a biphasic or monophasic complex.[6]
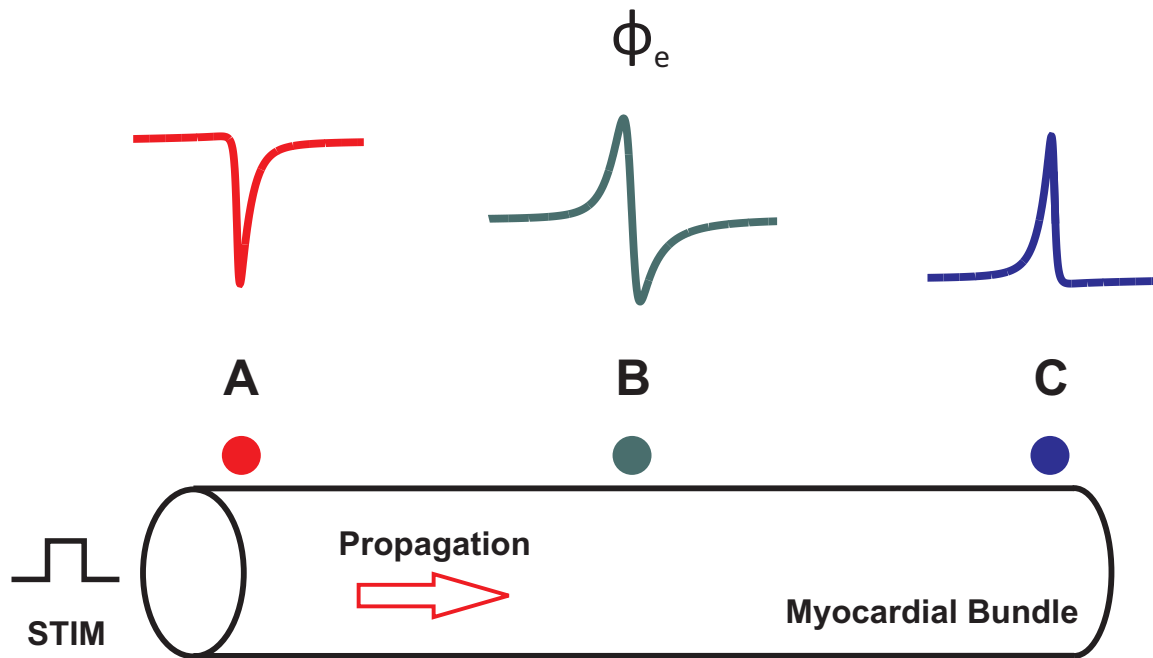
Figure 2.10: Unipolar extracellular electrograms ϕ_e generated by an electrical wavefront traveling along a myocardial bundle from the left to the right. Signals recorded at three different sites in respect to the wavefront: (A) Beginning, (B) Propagating and (C) Colliding. Figure adapted from de Bakker & Wittkampf.[6]

Fractionated Electrograms

In healthy myocardium, the basic configuration of the extracellular electrogram is simple. Under pathological conditions, however, electrograms may consist of multiple components, which have been attributed to abnormal conduction and arrhythmogenicity. Indeed, recent studies reported a novel ablation strategy targeting atrial areas with complex fractionated atrial electrograms (CFAEs) that are thought to represent substrates responsible for initiation or maintenance of AF.[17,18]

CFAEs can be caused by artifacts, such as movements between the electrode and the cardiac muscle; filter characteristics of amplifiers; remote activation of muscle bundles anatomically located close to each other (or even activation of the ventricles); or peculiar behavior of the wavefront, due to structural and electric complexity of the underlying myocardium.[6] Fig. 2.11 shows a CFAE, and its derivative, obtained during electrophysiological experiments with right atrial isthmus of an adult rabbit. Note that compared to an uniform atrial electrogram (UAE), also shown in Fig. 2.11, the CFAE has a lower amplitude and multiple peaks which are easily identified in the time derivative of the signal.
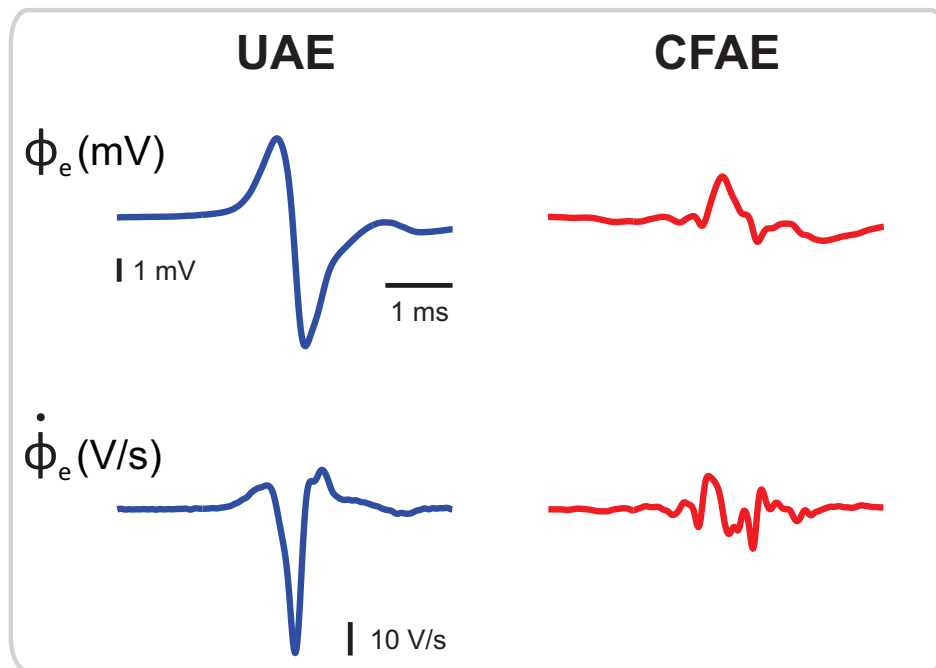
Figure 2.11: Examples of uniform (UAE) and complex fractionated (CFAE) atrial electrograms obtained in experiments with the ROI of an adult rabbit. Temporal derivatives $\dot{\phi}_e$ are also shown, since they are often used as a tool to reveal complexity with more ease. Experimental data kindly provided by Dr. Ernst Hofer[†].

Role of Spatial Distribution of Fibrosis in Conduction

Structural complexity due to fiber disarray and the formation of fibrotic connective tissue give rise to discontinuous conduction, which is associated with CFAEs.[6, 24, 47] Fibrosis, which involves a disproportional accumulation of collagen, is an integral feature of remodeling in the diseased heart. Collagen not only stiffens the myocardium, thereby reducing the contractile integrity, but also impairs electrical coupling between myocytes by separating them.[48] In fact, ischemia, myocardial infarction and CHF have been shown to be associated with a substantial remodeling of cardiac collagen extracellular matrix.[25, 49, 50] Furthermore, interstitial collagen content also increases with age,[14–16] which has been suggested to increase the vulnerability to AF.[48]

Fibrosis separates adjacent myocardial bundles electrically over considerable lengths, thus preventing a direct propagation of APs between neighboring bundles. Since the wavefront may follow a zig-zag course, activation delays arise simply because of the increase of the route that the wavefront has to travel.[7] Such a tortuous route increases the path length of activation giving rise to apparent conduction slowing along the fiber direction. Besides the amount of fibrosis, its texture plays a crucial role in propagation of the electrical impulse. Fibrosis may be compact, patchy or diffuse[7] (see Fig. 2.12). With

---

[†]Institute of Biophysics, Medical University of Graz, Austria.
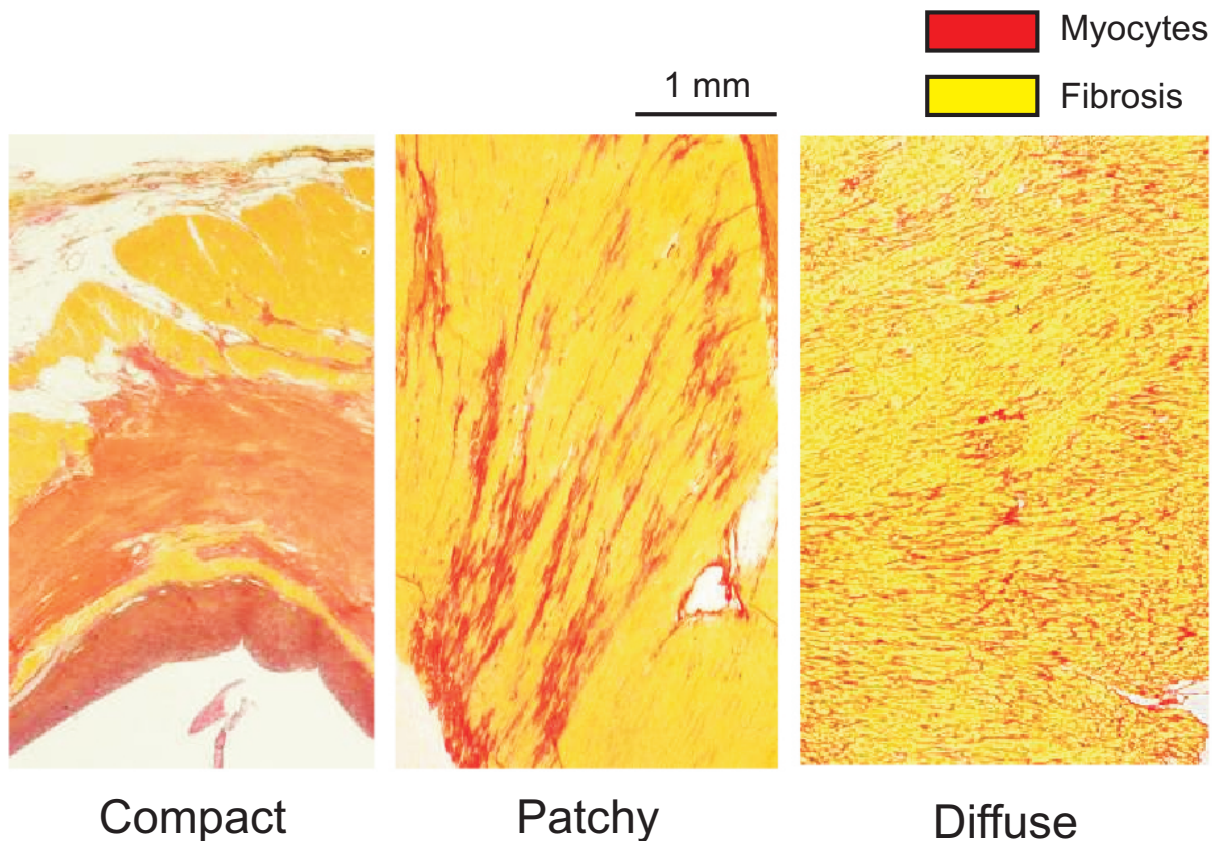
Figure 2.12: Different textures (spatial distributions) of fibrosis in the heart. The staining (Picrosirius red) resulted in a coloring of myocytes (yellow) and connective tissue (red). (A) Compact fibrosis consisting of areas of dense collagen deprived of any myocardial tissue. (B) Patchy fibrosis characterized by a mixture of myocardial and collagen bundles. (C) Diffuse fibrosis, which involves areas where myocardial and collagen fibers merge. Figure adapted from de Jong *et al.*[7]

regard to arrhythmogenicity the effect of the different types of fibrosis highly varies. Compact fibrosis comprises a fibrotic area that is completely deprived of myocardium. Although it looks severe, is the least arrhythmogenic of the different types since reentry can only occur as circus movement around the fibrotic area. In practice, reentry around scar tissue is only observed sporadically in the human heart. Patchy fibrosis is characterized by areas where collagen fibers and myocardial bundles merge consisting of long strands. This type of fibrosis can cause large conduction delays because of zig-zag conduction between the various bundles and is most vulnerable to arrhythmias. Diffuse fibrosis consists of short stretches of fibrosis. It also impairs conduction, but to a lesser extent compared to patchy fibrosis in case the amount of fibrosis is the same.[7,48]

Mapping at a Microscopic Size Scale
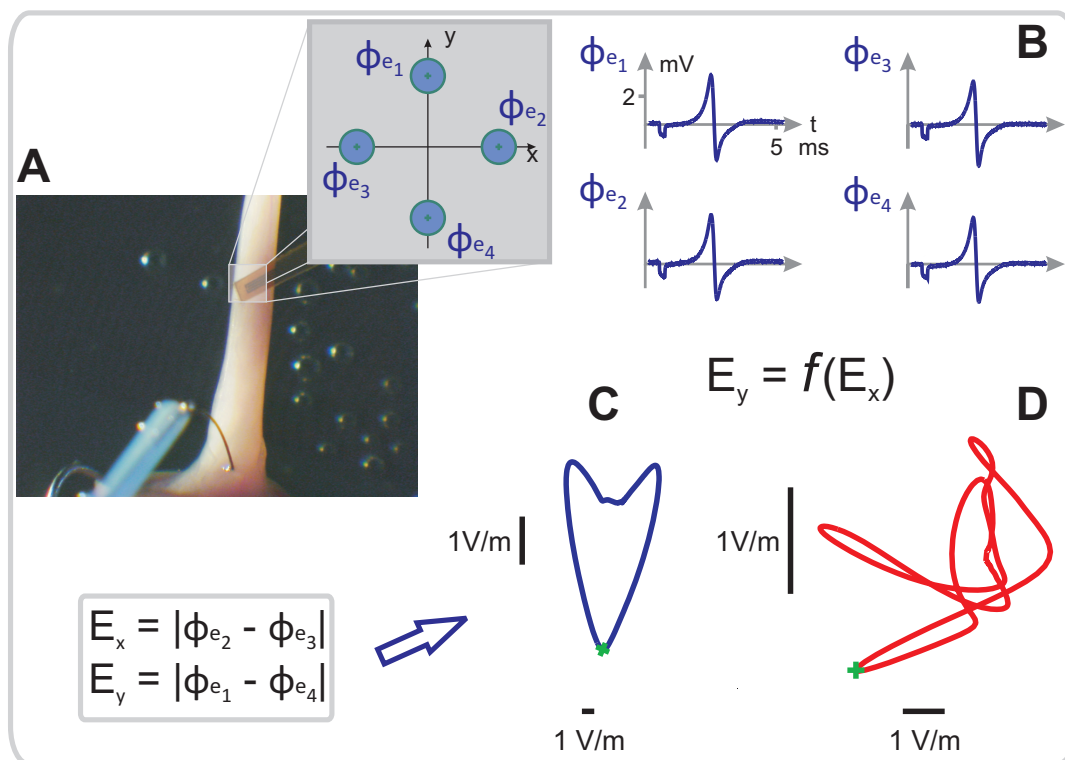
Figure 2.13: (A) A papillary muscle from a rabbit heart pinned on silicone rubber with tungsten needles and superfused with oxygenated Tyrode's solution. Showing a pacing electrode (lower part) and four-electrode sensor array carried from flexible polyamide (upper part). (B) Uniform atrial electrograms (UAE) obtained in each of the four electrodes. (C) 2D representation of the near field $\boldsymbol{E}$, based on the four signals in (B), forming a vector-loop pointing in the opposite direction to the local propagation (highlighted in green). The vector-loop is obtained by plotting $E_y = f(E_x)$. (D) Example of a vector-loop constructed based on complex fractionated atrial electrograms (CFAEs). Figure kindly provided by Dr. Ernst Hofer[‡].

Discontinuous conduction caused by connective tissue or by intercellular clefts may produce substantial irregularities in extracellular signals with multiple deflections (fractionated electrograms). The spatio-temporal separation of fractionated waves of depolarization can be in the submillimeter range. Although the presence of multiple small electrical events can be detected in the electrograms, directional properties of the wavefront can not. The cardiac activation pattern can be computed from a set of electrograms obtained with unipolar[*] or bipolar[†] recordings.[51] In the clinical setting, a bipolar recording is often preferred over a unipolar one because it represents rather local electrical

---

[‡]Institute of Biophysics, Medical University of Graz, Austria.

[*]Recording electrode is close to the active tissue while the reference electrode is located far from it.

[†]Obtained by subtracting two unipolar electrograms recorded at sites that are usually close together.

events.[7] However, the bipolar signal is triphasic instead of biphasic if a wavefront is passing, which makes its interpretation more complicated. In addition, the bipolar electrogram is direction dependent; its amplitude depends on the direction of the wavefront with respect to the line through the poles of the electrode. Moreover, the bipolar vanishes when the excitation wavefront is parallel to the axis formed by the two recording sites. A square arrangement of four tightly spaced electrodes four-element electrode array overcomes this difficulty and allows computation of a vector representation of the cardiac near field (CNF) $\boldsymbol{E} = [E_x \ E_y]^T$ from two bipolar recordings.[52]

$\boldsymbol{E}$ describes a vector-loop which varies in morphology from a straight line to an "open" loop similar to those seen in a vector cardiogram.[52] See Fig. 2.13 for examples of vector-loops obtained with a CNF measurement system. The peak vector of $\boldsymbol{E}$ points in the opposite direction to the local propagation and is oriented perpendicular to the isochrones of activation. Its morphology changes with curvature of the wavefront as well as with the probe orientation. The directional properties of CNF measurements can be exploited to trace the pathways of conduction, to precisely spot sites of ectopic activity and to obtain accurate estimations of the local conduction velocity.[52]

2.3.3 Limitations of Measurement Systems and Experimental Protocols

Classical electrophysiology techniques involve placing electrodes into various preparations of cardiac tissue. If an electrode is small enough (μm) in diameter, its tip could be inserted into a single cell allowing direct observation and recording of APs. However, such invasive setups reduce the life of the cell and cause a leak of substances across the membrane. As an alternative, optical mapping techniques are used to record APs from cardiac tissue without insertion of microelectrodes. To do so, the tissue preparation is stained with voltage-sensitive fluorescent dyes that bind to cell membranes. The signal that indicates electrical activity of the cells consists of a change in the fluorescence properties of the dye. The downsides of optical mapping are the possible toxicity of the dyes, the signal-to-noise ratio is low, and the unavoidable motion artifacts in optical signal due to cardiac contraction. Such constraints may favor extracellular recording techniques since cell impalement is avoided and displacement artifacts due to the mechanical movements are accounted for. Nonetheless, for technical and theoretical reasons, extracellular recording systems have always been a trade-off between number of electrodes, electrode size, electrode spacing and recording resolution in amplitude and time. For instance, as electrode size increases, the resolving power decreases. Larger electrodes are sensitive only to the net activity of cells within a certain portion of tissue, termed local field potentials. Finally, the underlying microstructure is not known during the experiment, which makes the interpretation of the signals a challenging endeavor.

In addition to the constraints inherent to the measurement systems, limitations in the protocols used during experiments could lead to misinterpretation of the results. Among them, superfusion as a method to provide cardiac tissue with proper oxygen supply and waste removal is of particular interest in this thesis.

Superfusion with Oxygenated Solutions

Multicellular cardiac preparations, such as isolated small animal atria (Fig. 2.14), pulmonary vein sleeves, ventricular slices as well as trabeculae and papillary (Fig. 2.13 A) muscles are widely used in experiments to study the physiology of cardiac function in healthy state and disease.[53–56] Unlike in isolated myocytes, gap junctions and extracellular matrix are preserved, allowing to characterize electrophysiological function under conditions similar to those in intact hearts (see Fig. 2.14 B).
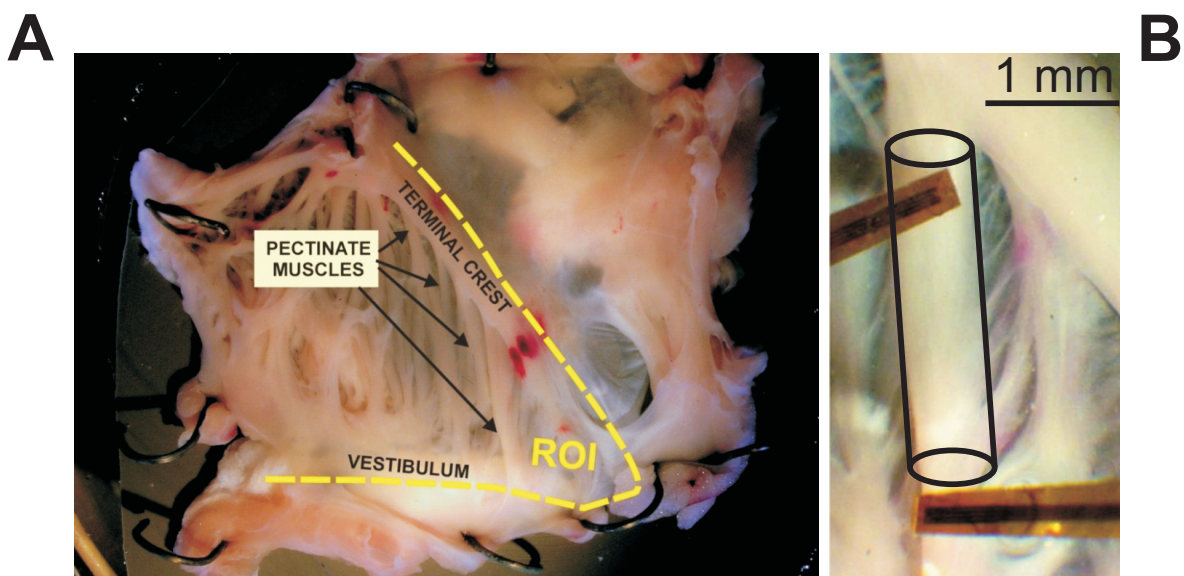
Figure 2.14: (A) Posterior part of the lower right atrium of a rabbit heart (region of interest - ROI) pinned on silicone rubber with tungsten needles and superfused with oxygenated Tyrode's solution. (B) Ramification of the crista terminalis into a pectinate muscle. Two four-electrode sensor arrays carried from flexible polyamide to measure extracellular potentials are shown. Figure kindly provided by Dr. Ernst Hofer[‡].

In larger tissue preparations or whole heart experiments, perfusion[*] is the method of choice to ensure adequate oxygen supply as well as wash out of waste products to the cells.[57] In small tissue preparations, on the other hand, perfusion might not be possible. Thus, due to its simplicity, superfusion with oxygenated solutions is typically employed for thin-walled tissue samples.[53–56,58,59] Although superfusion is adequate to maintain

---

[‡]Institute of Biophysics, Medical University of Graz, Austria.

[*]A experimental *in vitro* technique, where nutrients and oxygen delivery is done in a reverse fashion (via arteries).

preparations viable for prolonged experimental procedures, this is not the case with larger samples where the thickness of the muscle wall exceeds the maximum diffusion depth.[60] In these cases metabolic deficits build up with distance from superfused surfaces. High-energy phosphate stores in anoxic regions become depleted, hyperkalemia and acidosis develop due to insufficient wash out causing cells to become non-excitable and non-conductive.

Although these progressive changes which drive the formation of an ischemic[61,62] and, ultimately, a myolytic core, clearly compromise integrated physiological functions such as active force generation,[60] further elucidation is required to clarify as to which extent these pathological conditions in deeper layers of the tissue affect excitation spread and extracellular depolarization signals recorded close to the intact and viable surface. On one hand, the contribution of cells in ischemic regions as current sources during depolarization will be attenuated or even disappear.[63] On the other hand, these cells will influence electrophysiological behavior of viable cells in adjacent surface layers via electrotonic interactions.[33] A detailed quantitative understanding of these processes and their effects upon excitation spread, as observed at the tissue surface, is key to allow a correct interpretation of experimental data recorded from such preparations.

2.4   The Role of Computer Models

The anatomical diversity of conduction structures and their topology at a microscopic size scale is overwhelming. Inquiries as to which extent anatomical factors influence over the electrical activation sequence at different size scales with experimental techniques only are a challenging endeavor, since in an experimental context only a subset of the parameters of interest is tangible. In recent years, very detailed computer simulation studies that account for the cardiac anatomy at all size scales of interest, have become feasible and, thus are increasingly considered as an indispensable complement to experimental studies.[64–66] In such computer models the structural complexity can be varied step by step. For instance, as a starting point simplified isotropic models of the macro anatomy of the ROI can be employed. Subsequently, such models can be extended to include the endocardial macroanatomy with appropriate anisotropic properties corresponding to the respective fiber directions. Finally, microscopic details can be added either by introducing artificial barriers of conduction at a size scale that has been found to be characteristic for connective tissue layers in histology, or alternatively, histographs can be segmented and directly converted to finite element (FE) meshes.[11,23,67] In an histologically detailed model, all parameters of interest are tangible at spatial and temporal resolutions well beyond the experimentally feasible limits. Provided that a careful validation of the *in silico* model with experimental data has been performed, such models are the method of

choice to gain mechanistic insights into the phenomena observed in experiments.

Several computer models describing excitation spread in the atria have been reported in literature. In some earlier studies, simple cellular automata models had been employed.[68] Later on, macroscopically accurate 2D monolayer descriptions were reported using ionic models.[69] More recently, macroscopically realistic three-dimensional models of the entire atria incorporating major atrial bundles and making use of realistic descriptions of the dynamic membrane behavior became available.[70–72] At the microscopic size scale, very detailed models employed to study the behavior of the electrical propagation at a sub-cellular level and its relation with cardiac arrhythmias.[4,16,25,73] Recent studies using detailed geometries of the rabbit and pig RA with high spatial resolution, quantified the contributions of the tissue heterogeneity and anisotropy to reentry initiation mechanisms.[4,73] The authors showed that the complex organization of the RA tissue causes breakdown of regular AP conduction patterns at high pacing rates. Moreover, at a finer spatial scale, numerical simulations demonstrated that changes in AF activation frequency and dynamics are controlled by the interaction of electrical waves with clusters of fibrotic patches of various sizes.[25] However, the relation between the underlying microstructure and the morphology of electrograms was not addressed. In another elegant theoretical work, the authors showed that the density and length of microscale obstacles decrease conduction velocity and cause significant changes to electrogram waveforms.[24] Nevertheless, their rather simple monolayer model with transverse uncoupling can not be used to discriminate complex collagen organization like seen in histology.[7,19,21] The characterization of microstructural organization of fibrosis through the inspection of electrograms is still a challenging endeavor for physicians as well as electrophysiologists. Therefore, a method to distinguish differences microstructural organization of fibrotic tissue would be useful in many areas of cardiovascular research.

Chapter 3

Cardiac Modeling and Simulation

The modeling of the electrical activity of the heart is of great medical and scientific interest, because it provides a way to get a better understanding of the related biophysical phenomena, allows the development of new techniques for diagnoses and serves as a platform for drug tests. There are two components that contribute to the modeling of cardiac electrical propagation.[74] The first is a model of cellular membrane dynamics, describing the flow of ions across the cell membrane. The second is an electrical model of the tissue that describes how currents from one region of a cell membrane interact with other regions and with neighboring cells. In the following chapter, the basic principles of both components are introduced.

3.1   Electrical Model of the Cell Membrane

The permeability of the cell membrane for a given ion is controlled by the electrical conditions of the environment in which the cell is immersed. Depending on the transmembrane potential, for instance, ion channels can alter their conformation in order to regulate the passage of ions. The opening and closing of ion channels in response to changes in transmembrane potential is the basis for electrical excitability.

The cell membrane separates the inner and outer conductive media through a thin insulating layer ($\sim 10\,\text{Å}$). Thus, the membrane can be seen as a capacitor, i.e., two conductive plates separated by an insulating material. In this case the intracellular and extracellular fluids would be the conductive plates, while the phospholipid bilayer would be the insulating material.[32] The capacitance of any insulator is defined as the ratio of the charge q across the capacitor to the voltage potential necessary to hold that charge, and is denoted by

$$C_m = \frac{q}{V_m} \tag{3.1}$$

where V_m is the transmembrane potential which is, by convention, the potential difference between intracellular (ϕ_i) and extracellular potentials (ϕ_e), respectively.

The total electrical resistance of the membrane R_m is the sum (in parallel) of the resistances of each ion channel. This resistance is associated with the number of open channels, the ionic concentrations in the intra- and extracellular spaces, and the mobility of these ions.[32] Thus, the cell membrane can be modeled by a nonlinear resistor coupled in parallel with a capacitor. This circuit is shown in Fig. 3.1.

Extracellular space

Intracellular space
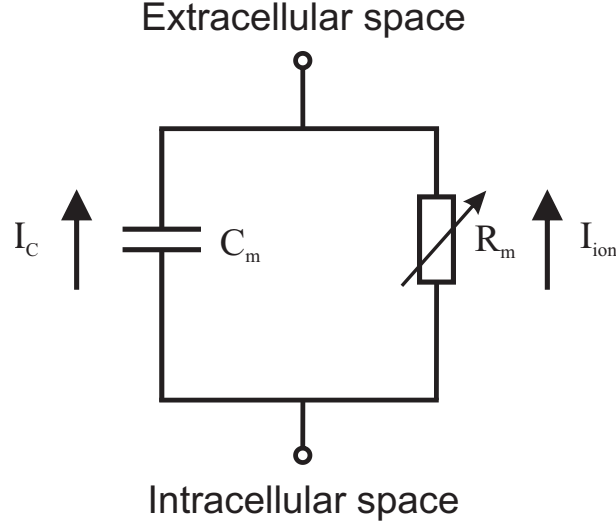
Figure 3.1: Electrical circuit model of the cell membrane. C_m is the membrane capacitance; R_m is the total electrical resistance of the membrane; I_c and I_{ion} are the capacitive and the ionic currents, respectively. The current flow from the intracellular space to the extracellular space is specified as positive.

Since the current is defined by dq/dt and provided that C_m is constant, it follows from Eq. 3.1 that the capacitive current I_c is given by

$$I_c = \frac{dq}{dt} = C_m \frac{dV_m}{dt} \tag{3.2}$$

Because there can be no net buildup of charge on either side of the membrane, the sum of the ionic (I_{ion}) and capacitive currents must be zero, and so

$$C_m \frac{dV_m}{dt} + I_{ion} = 0 \tag{3.3}$$

where $V_m = \phi_i - \phi_e$.

3.1.1 The Nernst Potential

The Nernst potential (or reversal potential) of an ion is the transmembrane potential at which there is no net (overall) flow of that particular ion from one side of the membrane to the other.[32] Fig. 3.2 depicts a schematically view of cell membrane as two-compartment system separated by a semipermeable membrane. The concentration of S^+ in compartment i (inside) is assumed to exceed that in compartment o (outside). In addition to that, it is also assumed that the membrane is impermeable to Q^-.
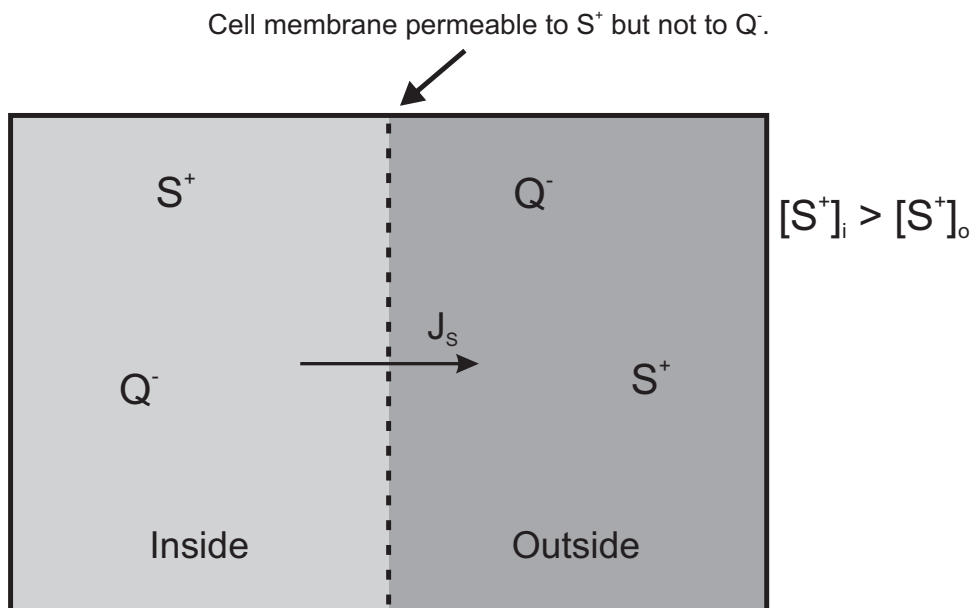
Figure 3.2: Schematic diagram of a membrane separating two solutions with different ionic (S^+ and Q^-) concentrations. J_S is the flux of ions S^+ due to the concentration gradient between the intra- and extracellular compartments. Figure adapted from Plonsey & Barr.[8]

Differences in concentrations cause the ions S^+ to move in the opposite direction of the concentration gradient. In contrast, because Q^- can not diffuse through the membrane, the diffusion of S^+ causes a buildup of charge across the membrane. This charge imbalance, in turn, sets up an electric field that will drive the S^+ in the opposite direction of the diffusion.[8] An equilibrium will be reached when the electric field exactly balances the diffusion of S^+. The value of the transmembrane potential which leads to a zero flow is given by the Nernst equation:

$$E_S = \frac{RT}{z\,F} \ln \left(\frac{[S^+]_o}{[S^+]_i} \right) \tag{3.4}$$

where R is the gas constant ($8314.0\,\mathrm{mJ/mol\,K}$), T is absolute temperature, z is the valence of the ion, F is Faraday's constant ($9\,648$ x $10^4\,\mathrm{C/mol}$), $[S^+]_o$ and $[S^+]_i$ denote the external and internal concentrations of the ion, respectively.

Thus, when $V_m = E_S$ there is no net current of S^+ between the phases, as the diffusion of S^+ is exactly balanced by the electric potential difference. The Nernst equation is called a universal law, because it is independent of how ions move through the membrane and depends only on the difference between the concentrations.[32] However, it assumes an ideal case, where the membrane separating the two compartments allows only the passage of the ion S^+ and no other ion (e.g. Q^-). A rigorous derivation of the Nernst potential can be found in Plonsey and Barr.[8]

3.1.2 The Ionic Current

Determine the form to I_{ion} in Eq. 3.3 is still a topic of active research, because different cells have different types of ion channels, which respond differently to changes in transmembrane potential, ionic concentrations and on a set of other variables.

The macroscopic behavior of ionic channels can be modeled with states and functions describing the transition between the states.[45] The simplest model for macroscopic channel kinetics assumes that each channel's behavior is independent, though governed by similar statistics. Further, each channel can be in an open O or closed state C, and the rate of transition from one state to another is a function of V_m. Let n be the proportion of channels in state O at any instant t. The variation of n with time is determined by:

$$\frac{dn}{dt} = \alpha(V_m)\,(1-n) - \beta(V_m)n \tag{3.5}$$

where $\alpha(V_m)$ is the rate of transition from closed to open and $\beta(V_m)$ the reverse transition rate. Fig. 3.3 shows a schematic diagram of the two-state model.
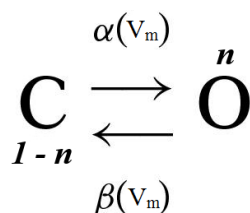
Figure 3.3: Schematic diagram of two-state model for an ion channel.

Eq. 3.5 can be conveniently rewritten in the form:

$$\frac{dn}{dt} = \frac{n_\infty - n}{\tau_n} \tag{3.6}$$

where

$$n_\infty = \frac{\alpha(V_m)}{\alpha(V_m) + \beta(V_m)} \tag{3.7}$$

is the steady-state value of n, and

$$\tau_n = \frac{1}{\alpha(V_m) + \beta(V_m)} \tag{3.8}$$

is the time constant approach to the steady state. Expressions for n_∞ and τ_n can be obtained from experimental data, and thus $\alpha(V_m)$ and $\beta(V_m)$ can be unambiguously determined.[32]

An important generalization of the two-state model in Fig. 3.3 occurs when the channel is assumed to consist of multiple identical subunits, each of which can be in either the closed or open state. In this case, the open probability of a population of channels with k equal subunits is proportional to n^k, where n satisfies Eq. 3.6.[32] Yet, it is often

the case where ion channels (e.g. sodium channels) are formed as a complex of several distinct subunits with different transition rates $\alpha(V_m)$ and $\beta(V_m)$. As for instance, a channel comprising k subunits of type n and l subunits of type h with transition rates $\alpha_n(V_m)$, $\beta_n(V_m)$ and $\alpha_h(V_m)$, $\beta_h(V_m)$, respectively. In this scenario, the probability that the channel is open is given by $n^k \times h^{l}$,[32] with n and h satisfying Eq. 3.6.

Furthermore, the maximum channel conductance $\bar{g}$ occurs when they are all open:[8]

$$\bar{g} = N g_\gamma \tag{3.9}$$

where N is the number of channels per unit area of membrane and g_γ is the single channel conductance.

Thus, the total current through a population of open channels (per unit area of membrane) resulting from the difference between the transmembrane voltage V_m and the Nernst voltage E_{eq} is given by

$$I_{ion} = \bar{g}\, O\, (V_m - E_{eq}) \tag{3.10}$$

where O is the proportion of open channels and $(V_m - E_{eq})$ is the ion's driving force.

Most of cell models available in the literature utilize multiple subunit formulation, also known as the Hodgkin-Huxley[9] formalism, for ionic channels. A common limitation of this approach is that activation and inactivation of the channel are considered to occur independently of each other. However, experiments have shown that the inactivation of an ion channel is a process closely coupled to activation.[75,76] In addition to that, channel gating modifications due to either genetic diseases or pharmacological therapies can not be modeled using this simple approximation.[77] Several new models for excitable cells have employed Markov chains as an alternative to the multiple subunit models to describe the behavior of ion channels.[77–79] In a simple Markov model of the sodium channel,[76] for instance, it is assumed that the channel can exist in three states: closed (C), open (O), or inactivated (I), and that once the channel is inactivated, it cannot return to either the closed or the open state. Such models make use of information provided by molecular biology studies being a more accurate description of channel gating properties in health and disease.[77]

3.1.3 The Hodgkin-Huxley Model

The mechanism of action potential generation was first elucidated by Hodgkin and Huxley[9] in the 50's, in their experiments with nerve cells. Since most of the current cardiac electrophysiological models are based on their pioneering work, the model will be briefly presented here. In the Hodgkin-Huxley model, I_{ion} is given by the sum of three currents (see Fig. 3.4):

$$I_{ion} = I_{Na} + I_K + I_L \tag{3.11}$$

where I_{Na} and I_K are, respectively, the sodium and potassium currents and I_L a leak current, that consists mainly of Cl^- ions.
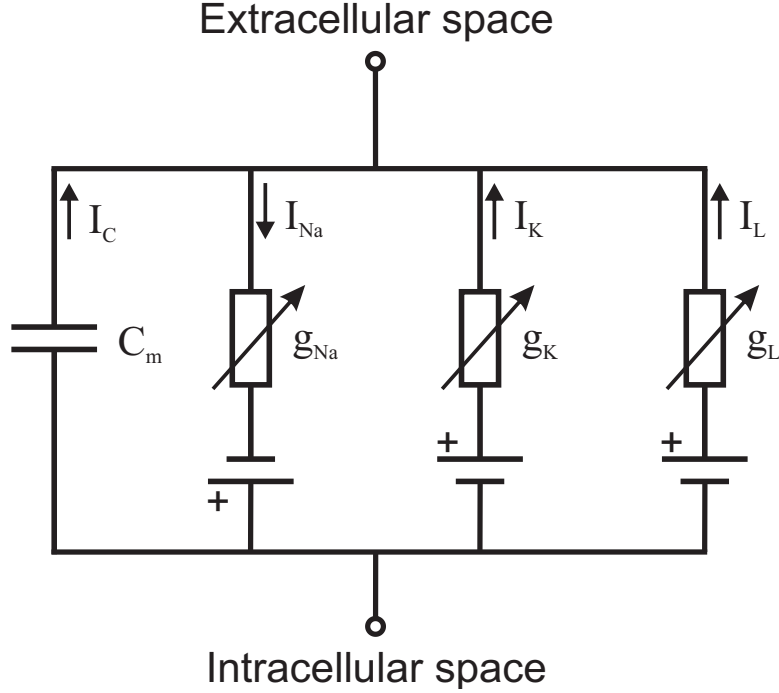
Figure 3.4: Electrical equivalent circuit proposed by Hodgkin and Huxley[9] to characterize the electrophysiology of a squid giant axon.

From Eqs. 3.3 (p. 26) and 3.11, follows that

$$C_m \frac{dV_m}{dt} + I_{Na} + I_K + I_L = 0 \tag{3.12}$$

In their model, the currents through the ion channels are linear in V_m as in Eq. 3.10:

$$\frac{dV_m}{dt} = -\frac{1}{C_m} \left(\bar{g_{Na}}\, m^3\, h\, (V_m - E_{Na}) + \bar{g_K}\, n^4\, (V_m - E_K) + \bar{g_L}\, (V_m - E_L) - I_{stim} \right) \tag{3.13}$$

where $\bar{g_{Na}}$, E_{Na} and $\bar{g_K}$, E_K are the maximum channel conductances (per unit area of membrane) and Nernst potentials of the Na^+ and K^+ channels (respectively); $\bar{g_L}$ and E_L refer to the leak current I_L; and I_{stim} is an external applied transmembrane current. The status of the channels is determined by the gating variables m, h and n, which open and close in a voltage-dependent manner (see Eq. 3.5). Further details about the mathematical expressions of the Hodgkin-Huxley model can be obtained in their original publication[9] or in any standard physiological modeling book.[8,32,45]

3.1.4   Cardiac Cells

The *voltage clamp* technique[*] contributed with quantitative data which supported the development of many models for different species and regions of the heart. All these models are based on detailed descriptions of the ionic currents observed in experiments with isolated myocytes.[80–85] The first model that describes the AP in cardiac cells has been proposed by DiFrancesco and Noble[82] for Purkinje fibers. In 1977, Beeler and Reuter[80] presented a model for the electrical activity in ventricular myocytes. The model includes equations for ionic concentrations as well as the calcium current due to the important role of this ion in cardiac muscle contraction. The Luo and Rudy[84] model is a more detailed description of electrophysiology of ventricular myocytes, it includes equations for the internal concentrations of sodium and potassium ions, and also for the calcium concentration in the sarcoplasmic reticulum (SR). Among all mathematical models of APs in heart cells, the Lindblad model[83] (atrium) and the Mahajan-Shiferaw model[79] (ventricle) are of particular interest in this thesis. This choice is due to the fact that both models were developed based on experiments with rabbit myocytes, the species considered throughout this work.

The Lindblad Model

A mathematical model describing the total ionic current for a rabbit atrial myocyte has been developed by Lindblad *et al.*[83] Available biophysical data have been incorporated into the model to quantify the specific structural morphology, intracellular ion buffering, and time- and voltage-dependent currents and transport mechanisms of the rabbit atrial cell. A schematic representation of the currents, fluxes, and physical compartments of the model is shown in Fig. 3.5. In generating APs, the model rabbit membrane potential (V_m) is determined by the following ordinary differential equation (ODE):

$$\frac{dV_m}{dt} = -\frac{1}{C_m}(I_{Na} + I_{Ca,L} + I_{Ca,T} + I_t + I_{K,r} + I_{K,s} + I_{K1} + \qquad (3.14)$$
$$+ \; I_{NaCa} + I_{NaK} + I_{Ca,p} + I_{Na,b} + I_{Ca,b} + I_{Cl,b} - I_{stim})$$

where I_{Na} is the fast Na^+ current; $I_{Ca,L}$ and $I_{Ca,T}$ are the the L-type and T-type Ca^{2+} currents, respectively; I_t is the transient outward K^+ current; $I_{K,r}$ and $I_{K,s}$ are the rapid and slow delayed rectifiers K^+ currents, respectively; I_{K1} is the time-independent inwardly rectifying K^+ current[†]; I_{NaCa} is the Na^+/Ca^{2+} exchanger; I_{NaK} is the Na^+/K^+

---

[*]Voltage clamp is a laboratory technique in electrophysiology to measure the ion currents across the membrane of excitable cells while holding the membrane voltage at a set level.

[†]A current that is "inwardly-rectifying" is one that passes current (positive charge) more easily in the inward direction (into the cell). At membrane potentials negative to potassium's reversal potential, inwardly rectifying K^+ channels support the flow of positively charged K^+ ions into the cell, pushing the membrane potential back to the resting potential. When first discovered, inward rectification was named "anomalous rectification" to distinguish it from outward potassium currents.[86]

pump; $I_{Ca,p}$ is the sarcolemmal Ca^{2+} pump; I_{Nab}, I_{Cab} and $I_{Cl,b}$ are the background Na^+, Ca^{2+} and Cl^- currents, respectively; and I_{stim} is the external applied current.
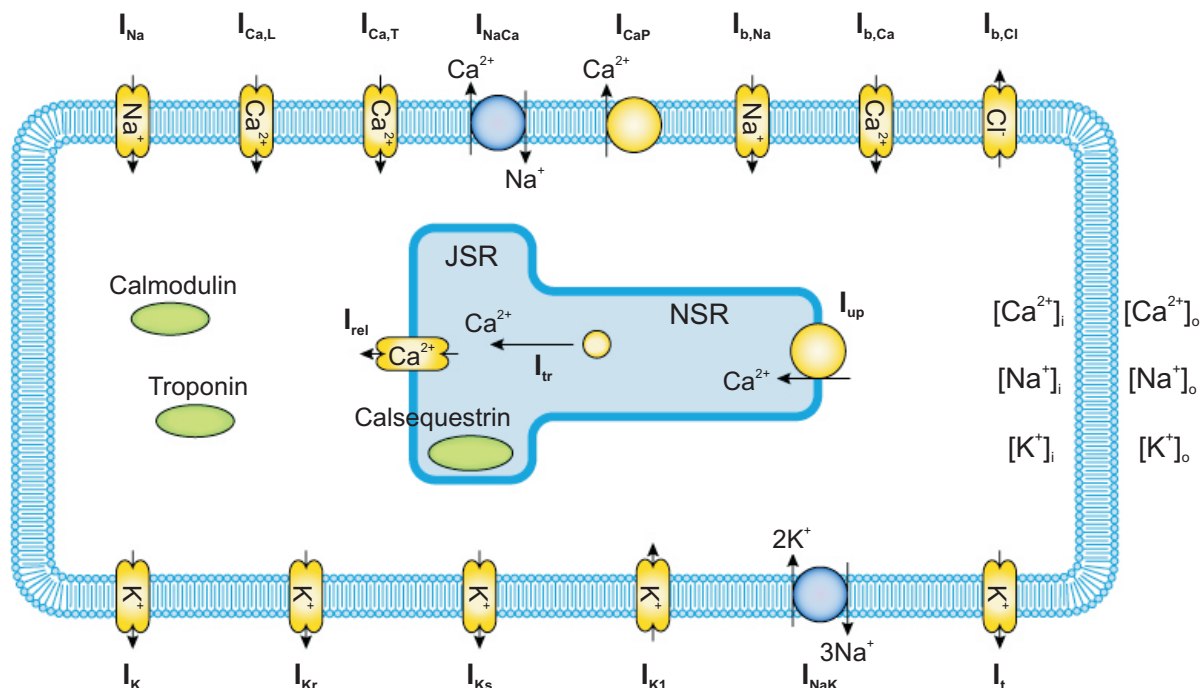
Figure 3.5: Schematic diagram of the (rabbit) atrial model ionic currents and Ca^{2+} fluxes. Figure downloaded and adapted from the cellML repository[‡].

Recently a new family of mathematical model was published by Aslanidi *et al.*,[4] incorporating newer experimental data on regional differences in several ionic currents determining the AP properties of rabbit RA cells. The models are a modification of the Lindblad model to account for differences in AP shape between myocytes from the CT and PM.

The Mahajan-Shiferaw (MSH) Model

The electrophysiological model proposed by Mahajan *et al.*[79] together with the Aslanidi models[4] represent the state-of-the-art throughout this thesis. The Mahajan-Shiferaw (MSH) model[79] has several advantages over the widely used Luo-Rudy model.[84] The MSH model is up to date the only detailed electrophysiological model, that accurately reproduces the dynamics of the cardiac AP and intracellular calcium cycling at rapid heart rates relevant to ventricular tachycardia and fibrillation. The ionic currents and all components involved in the modeling of the rabbit ventricular AP are illustrated in Fig. 3.6.

[‡]http://www.cellml.org/.
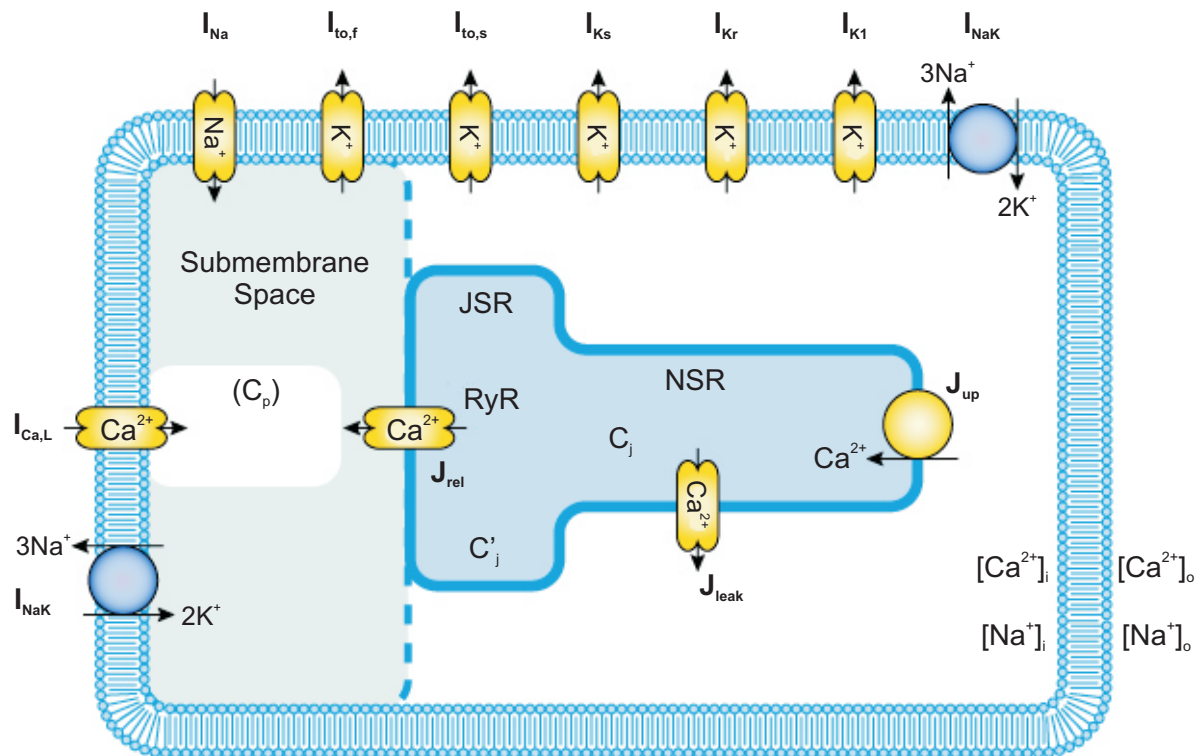
Figure 3.6: Schematic diagram of the (rabbit) ventricular model ionic currents and Ca^{2+} fluxes. Figure downloaded and adapted from the cellML repository[§].

3.2   Modeling the Electrical Excitation Spread

In order to describe the spread of an electrical excitation wavefront in cardiac tissue, the models describing the AP in a single myocytes have to be coupled to a tissue model. Ideally, the coupling method should be able to consider the anisotropic properties of cardiac tissue arising from the non-uniform distribution of gap junctions. In general, the electrical conduction in the heart can be described using microscopic or macroscopic approaches. In case of the microscopic methods, each myocyte is divided into segments in order to approximate their irregular surface. The segments are usually connected with low resistances to produce a cytoplasmic resistivity. Adjacent cells are not connected except at gap junctions, which are assigned with a higher resistance.[16] The advantage of such an approach is the possibility to consider heterogeneities in myocyte shape, gap junctions, ion channels and capillary distribution. The downside is the extremely high computational cost when it comes to simulations in larger tissue preparations or even the whole heart (with $\approx 10^{10}$ myocytes). In this context, the macroscopic approaches are preferred since they describe processes of the interacting cells based on a spatially homogenized representation of the tissue.[87] A trade-off between both approaches can be

---

[§]http://www.cellml.org/.

achieved by solving the partial differential equations (PDEs) arising from the homoge-nization procedure using very fine finite element (FE) meshes. This pseudo-microscopic method has been employed to study electrical activation in histologically detailed mod-els.[11,67,88] The pseudo approach was the method of choice during the course of this thesis and will be simply referred as microscopic modeling in the next chapters.

3.2.1 The Bidomain Model
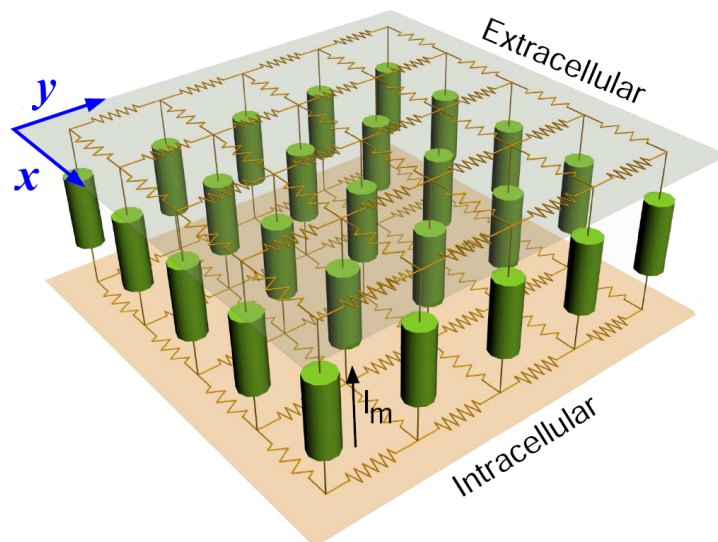
Figure 3.7: Bidomain representation of cardiac tissue in 2D. Intra- and extracellular (interstitial) domains are represented by the gray and orange planes, respectively. Within each domain, conductivities are anisotropic as indicated by the different resistances in each direction. Figure adapted from Vigmond *et al.*[10]

The set of bidomain equations[87] is currently one of the most complete mathematical models for describing the spread of cardiac electrical activity. The basis for the bidomain model is the division of the cardiac tissue into two domains: the intracellular and the ex-tracellular domains. Each domain is continuous and encompasses the whole myocardium, i.e., the domains have identical geometries and every point of the cardiac tissue is found in both domains.[89] In each domain, the current flow is purely resistive and thus, may be described by Ohm's law. In the intracellular domain, the current flows from one cell to another via the gap junctions. In the extracellular domain, on the other hand, the currents flow in the continuous space between the cells. Fig. 3.7 illustrates a bidomain representation of a 2D cardiac tissue. Accordingly, at each point in space there are two electrical potentials ϕ_i and ϕ_e, as well as two currents I_i and I_e, with subscripts i and e denoting intracellular and extracellular space, respectively.

The relationship between current and potential is ohmic:[32]

$$I_i = -\boldsymbol{\sigma_i} \nabla \phi_i \tag{3.15}$$

$$I_e = -\boldsymbol{\sigma_e} \nabla \phi_e \tag{3.16}$$

where $\boldsymbol{\sigma_i}$ and $\boldsymbol{\sigma_e}$ are the intracellular and extracellular conductivity tensors, respectively, given in mS/cm. Both minus signs arise because positive longitudinal currents are assumed to flow in the positive x and y directions.

At any point in space the total current is $I_m = I_i + I_e$ and unless there are no build up of charges, the total current is conserved:

$$\nabla \cdot (\boldsymbol{\sigma_i} \nabla \phi_i + \boldsymbol{\sigma_e} \nabla \phi_e) = 0 \tag{3.17}$$

The transmembrane current I_m is the current that leaves the intracellular space to enter the extracellular space:

$$I_m = \nabla \cdot (\boldsymbol{\sigma_i} \nabla \phi_i) = -\nabla \cdot (\boldsymbol{\sigma_e} \nabla \phi_e) \tag{3.18}$$

At every point in space there is a transmembrane potential $V_m = \phi_i - \phi_e$ (in mV). Moreover, for a biological membrane, the total I_m is the sum of ionic and capacitive currents (Eq. 3.3, p. 26). Hence, the set of bidomain equations linking both intracellular and extracellular potential fields via transmembrane currents, which act as sources is given by:

$$\nabla \cdot (\boldsymbol{\sigma_i} \nabla \phi_i) = +\beta I_m, \tag{3.19}$$

$$\nabla \cdot (\boldsymbol{\sigma_e} \nabla \phi_e) = -\beta I_m, \tag{3.20}$$

$$C_m \frac{\partial V_m}{\partial t} + I_{ion}(V_m, \boldsymbol{\eta}) - I_{stim} = I_m, \tag{3.21}$$

$$\frac{\partial \boldsymbol{\eta}}{\partial t} = \boldsymbol{g}(V_m, \boldsymbol{\eta}), \tag{3.22}$$

$$V_m = \phi_i - \phi_e \tag{3.23}$$

where β (cm^{-1}) is the membrane surface-to-cell volume ratio, needed to convert transmembrane current per unit area into transmembrane current per unit volume; I_{stim} $(\mu A/cm^2)$ is the stimulus current density; C_m is the membrane capacitance per unit area $(\mu F/cm^2)$; and I_{ion} $(\mu A/cm^2)$ is the density of the total ionic current flowing through the membrane channels, pumps and exchangers, which in turn depends on V_m (mV) and on a set of state variables, $\boldsymbol{\eta}$. $\boldsymbol{\eta}$ accounts for the dynamics of cellular processes such as gating or changes in concentrations within intracellular compartments. The vector-valued function $\boldsymbol{g}$ comprises the set of functions which describes the rate of change of the state variables $\boldsymbol{\eta}$. At the tissue boundaries, electrical insulation is assumed, which is accounted for by imposing no-flux boundary conditions on I_i and I_e, i.e., $\boldsymbol{n} \cdot \boldsymbol{\sigma_i} \nabla \phi_i = \boldsymbol{n} \cdot \boldsymbol{\sigma_e} \nabla \phi_e = 0$, where $\boldsymbol{n}$ is the normal component of the outward current.

The bidomain equations can be conveniently recasted to retain ϕ_e and V_m, the two experimentally measurable quantities of interest, as the independent variables. A particularly popular linear transformation is achieved, firstly, replacing ϕ_i by $V_m + \phi_e$ according to Eq. 3.23 in Eq. 3.19:

$$\nabla \cdot (\boldsymbol{\sigma_i} \nabla (V_m + \phi_e)) = \beta I_m, \tag{3.24}$$

then, replacing I_m by its formulation in Eq. 3.21:

$$\nabla \cdot (\boldsymbol{\sigma_i} \nabla (V_m + \phi_e)) = \beta \left(C_m \frac{\partial V_m}{\partial t} + I_{ion}(V_m, \boldsymbol{\eta}) - I_{stim} \right) \tag{3.25}$$

The second part of the transformation is obtained by adding Eq. 3.20 and Eq. 3.24:

$$\nabla \cdot (\boldsymbol{\sigma_i} \nabla (V_m + \phi_e)) + \nabla \cdot (\boldsymbol{\sigma_e} \nabla \phi_e) = 0 \tag{3.26}$$

which can be rearranged as follows:

$$\nabla \cdot (\boldsymbol{\sigma_i} \nabla V_m) + \nabla \cdot ((\boldsymbol{\sigma_i} + \boldsymbol{\sigma_e}) \nabla \phi_e) = 0 \tag{3.27}$$

In many experimental setups including *in vivo* studies, cardiac tissue is surrounded by a conductive medium, such as blood or a superfusing Tyrode's solution, that can be modeled by an additional Poisson equation:

$$\nabla \cdot (\sigma_b \nabla \phi_e) = 0 \tag{3.28}$$

where σ_b (mS/cm) is the isotropic conductivity of the conductive medium.

Hence, the widely used transformation proposed by Pollard *et al.*[90] is obtained from Eqs. 3.25, 3.27 and 3.28:

$$\nabla \cdot (\boldsymbol{\sigma_i} \nabla V_m) + \nabla \cdot (\boldsymbol{\sigma_i} \nabla \phi_e) = \beta \left(C_m \frac{\partial V_m}{\partial t} + I_{ion}(V_m, \boldsymbol{\eta}) - I_{stim} \right), \tag{3.29}$$

$$\begin{bmatrix} -\nabla \cdot ((\boldsymbol{\sigma_i} + \boldsymbol{\sigma_e}) \nabla \phi_e) \\ \nabla \cdot (\sigma_b \nabla \phi_e) \end{bmatrix} = \begin{bmatrix} \nabla \cdot (\boldsymbol{\sigma_i} \nabla V_m) \\ 0 \end{bmatrix}, \tag{3.30}$$

$$\frac{\partial \boldsymbol{\eta}}{\partial t} = \boldsymbol{g}(V_m, \boldsymbol{\eta}) \tag{3.31}$$

where V_m and ϕ_e, the quantities of primary concern, are retained as the independent variables.

Note that Eq. 3.30 treats the bath as an extension of the interstitial space. In this case, no-flux boundary conditions are assumed at the boundaries of the conductive medium $\boldsymbol{n} \cdot \boldsymbol{\sigma_i} \nabla \phi_i = 0$, whereas continuity of the normal component of the extracellular current and continuity of ϕ_e are enforced at the tissue-bath interface, i.e., $\boldsymbol{n} \cdot \boldsymbol{\sigma_e} \nabla \phi_e = \boldsymbol{n} \cdot \boldsymbol{\sigma_b} \nabla \phi_e$. Typically, Dirichlet boundary conditions are applied in the extracellular domain to prescribe potentials as imposed by the electrodes of a data acquisition system, i.e. nodes in the mesh are chosen where ϕ_e is fixed at zero value.

3.2.2   The Monodomain Model

Despite being currently the most complete description of cardiac electrical activity, the numerical solution of the bidomain equations is very computationally demanding.[10, 26, 27] A simpler approximation can be obtained from the model formulation by considering the intracellular and extracellular conductivities to have equal anisotropy ratios, i.e., $\boldsymbol{\sigma_i} = \lambda \boldsymbol{\sigma_e}$, where λ is a scalar.[91] Substitution of this relation in Eq. 3.27 and solving for $\nabla \cdot (\boldsymbol{\sigma_i} \nabla \phi_e)$ gives:

$$\nabla \cdot (\boldsymbol{\sigma_i} \nabla \phi_e) = -\frac{1}{(1+\lambda)} \nabla \cdot (\boldsymbol{\sigma_i} \nabla V_m) \tag{3.32}$$

Substituting Eq. 3.32 into Eq. 3.25 follows that:

$$\nabla \cdot (\boldsymbol{\sigma_i} \nabla V_m) - \frac{1}{(1+\lambda)} \nabla \cdot (\boldsymbol{\sigma_i} \nabla V_m) = \beta \left(C_m \frac{\partial V_m}{\partial t} + I_{ion}(V_m, \boldsymbol{\eta}) - I_{stim} \right) \tag{3.33}$$

Rearranging the terms in Eq. 3.33 reduces the system to the monodomain equations:[92]

$$\nabla \cdot (\boldsymbol{\sigma_m} \nabla V_m) = \beta \left(C_m \frac{\partial V_m}{\partial t} + I_{ion}(V_m, \boldsymbol{\eta}) - I_{stim} \right), \tag{3.34}$$

$$\frac{\partial \boldsymbol{\eta}}{\partial t} = \boldsymbol{g}(V_m, \boldsymbol{\eta}) \tag{3.35}$$

where $\boldsymbol{\sigma_m}$ is called the harmonic mean conductivity tensor or the effective bulk conductivity given by:[93]

$$\sigma_m^\zeta = \frac{\sigma_i^\zeta \sigma_e^\zeta}{\sigma_i^\zeta + \sigma_e^\zeta} \tag{3.36}$$

where $\zeta = l \,|\, t$ are the eigendirections of the conductivity tensor along ($\zeta = l$) and transverse ($\zeta = t$) to the cardiac fibers.

ϕ_e Recovery Method

Although the monodomain equations describe only current flow in the intracellular space of the cardiac tissue, the extracellular potentials ϕ_e can be recovered based on the transmembrane currents. Specifically, the electric potential field of a current point source lying in a uniform volume conductor of infinite extent and conductivity σ_b (mS/cm) is given by:[8]

$$\phi_e(r) = \frac{1}{4\pi\sigma_b} \frac{I_0}{r} \tag{3.37}$$

where I_0 is the strength of a current point source, and r is the distance between source and field point.

However, the transmembrane current is not confined to a point, but instead varies in space. Hence, finding ϕ_e requires an integration over the tissue volume (Ω):

$$\phi_e = \frac{1}{4\pi\sigma_b} \int \frac{\beta I_m}{\|\boldsymbol{r}\|} d\Omega \tag{3.38}$$

where $\boldsymbol{r}$ is the distance vector between source and field points. Using Eq. 3.34 the source term βI_m is given by $\nabla \cdot (\boldsymbol{\sigma_m} \nabla V_m)$.[93]

3.2.3 Modeling Fiber Orientation

The electrophysiological behavior of the myocytes is extremely important when simulating the spread of the electrical wavefront in the heart. However, the propagation of the AP is also strongly affected by how the myocytes are connected to form the muscle tissue. Moreover, the preferential arrangement of cardiac cells within the heart (fiber orientation) is known to play crucial roles in electrical and mechanical activity.[44,94] Therefore, to accurately represent anisotropic conduction, it is necessary to include the orientation of the muscle fibers to the model formulation.

Fiber information can be incorporated into the model using either rule-based approaches or assessed by histological sectioning or diffusion tensor magnetic resonance imaging (DT-MRI).[95,96] Based on the fact that fibers negotiate around intramural structures in a continuous manner, Bishop *et al.* [96] proposed a novel method which successfully represents the fiber architecture in cardiac tissue. The authors adapted the Laplace-Dirichlet method, which involves computing the solution of an electric potential, ϕ within the tissue between two electrodes using Laplace's equation ($\nabla^2\phi = 0$) where isotropic conductivity is assumed. A voltage is assigned between the electrodes and no flux conditions are imposed on all other surfaces. Field lines will terminate only on the electrodes and be tangential to all other surfaces. The resulting potential gradient will be smooth and globally point from one electrode to the other, but importantly, navigate around local discontinuities, i.e., holes in the tissue.[96]

Methods for measuring fiber orientation in histological images based on intensity gradients have been successfully employed to assess myofiber disarray associated with cardiomyopathy.[94] Such methods are ideal for capturing all the details found in the microstructure of the cardiac tissue, being thus, often used to study the electrical conduction in the atria.[11,67,73] Briefly, the algorithm determines local orientation in images by forming a pixel-by-pixel gradient vector with magnitude and direction with respect to the horizontal axis of the image. The direction of orientation is perpendicular to the direction of the intensity gradient.[94,97]

3.3 Simulations of the Cardiac Electrical Activity

The bidomain model is one of the most complete mathematical descriptions of the electrical activity at the tissue scale, but due to its complexity, it is impossible to obtain an analytical solution of the equations. Because of that, the equations must be discretized in time and space in order to obtain an approximated solution. To do so, the bidomain equations are usually discretized based on Eqs. 3.29-3.30 via an operator splitting technique.[89] This technique decouples the computing scheme into three components, an elliptic PDE, a parabolic PDE and a set of nonlinear ODEs. Solutions are then found by

leapfrogging between the decoupled components, where either V_m in equation Eq. 3.29 or ϕ_e in Eq. 3.30 are considered as constant.[27]

Despite being widely used to simulate the cardiac electrical activity, both mono- and bidomain models are very computational costly to solve. Such complexity arises from to the high spatio-temporal characteristic of the electrical impulse propagation. Transients in the heart are fast, requiring high temporal resolution, and wavefronts are steep, necessitating fine spatial resolution. Combined, these two factors result in large FE grids associated with systems of equations that have to be solved thousands of times in order to simulate a single heart beat.[65] The lack of efficiency has been among the most important limiting factors over the last decade that forced drastic model simplifications to reduce the computational burden. Recent improvements, both in available computing power[12,98] and numerical techniques,[26,27,89] promise to lift some of these restrictions to allow unprecedentedly realistic simulations of electrical and mechanical functions without current trade-offs in terms of representation of structural or functional detail.

A detailed discussion about numerical methods to efficiently solve the system of equations arising from spatial discretization of the PDEs is out of the scope of this thesis. The interested reader looking for more specialized literatures in the field is kindly referred to Vigmond *et al.*[10] and Plank *et al.*[26,65]

Chapter 4

Material and Methods

This chapter introduces the material and methods that were used for the various electro-physiological studies conducted during the course of this thesis:

1. The development of a radially symmetric model representing a muscle bundle from the ROI to quantify possible limitations of superfusion with oxygenated solutions.

2. Modeling activation sequences in the right atrial isthmus of the rabbit in macro- and microscopic scales.

3. The correlation between microstructural organization of fibrosis and atrial electro-grams.

4. The evaluation of the performance of GPU solvers to accelerate the simulations of the atrial electrical activity.

The corresponding results can be found in Chap. 5.

4.1   Cardiac Cell Models

4.1.1   Atrial Myocyte Model

Both the Lindblad and Aslanidi models[4,83] were employed to describe cellular dynamics of rabbit atrial myocytes (Eqs. 3.34-3.35 in p. 37). Among all reformulations suggested by Aslanidi *et al.*,[4] the inactivation time constant τ_{h2} of the fast sodium current I_{Na} is of particular interest in this work. In their study, τ_{h2} was decreased by 2.5 ms. On one hand, this modification improves the match between the simulation and recent experimental data. On the other hand, it results in a reduction of the AP overshoot (see Fig. 2.6 A), which in turn leads to block in electrical conduction at the tissue level. Thus, a decrease of 1.5 ms, instead of 2.5 ms, in τ_{h2} was used in this work as a trade-off between successful propagation and proper atrial AP waveform.

4.1.2 Ischemic Myocyte Model

The MSH model[79] was used to describe cellular dynamics of normal rabbit ventricular myocytes (terms I_{ion}, $\boldsymbol{\eta}$ and $\boldsymbol{g}(V_m, \boldsymbol{\eta})$ in Eqs. 3.21-3.22, p. 35). The choice of a ventricular AP model, rather than an atrial one, is justified by the fact that most of the available data (experiments and simulations), in respect to ischemia, were performed with tissue from the ventricles. Following previous approaches, model modifications were introduced to represent the three main components of ischemia at the cellular level: hyperkalemia, acidosis and hypoxia.[99–101] Two distinct phases during the first hour after coronary occlusion can be distinguished,[102] a first phase, referred to as phase 1a, which lasts for about 15 min and a second, later phase, referred to as phase 1b, lasting from 15 to 45 min after coronary occlusion. To account for the progression of ischemia, model parameters were adjusted to represent the combined effects of hyperkalemia, acidosis and hypoxia at 0 min (control); 5 and 10 min (phase 1a); 15 and 30 min (phase 1b) after coronary occlusion (see Tab. 4.1).

Hyperkalemia was introduced by increasing the extracellular potassium concentration $[K^+]_e$.[100, 103] Since the MSH model does not explicitly account for pH value, effects of acidosis were modeled indirectly through a decrease in the L-type calcium and sodium channel conductances, g_{Ca} and g_{Na}, respectively, and by shifting the voltage-dependent kinetics of the sodium current $V_{s,Na}$.[100, 101, 104] Hypoxia was mimicked by augmenting the MSH model with an ATP sensitive potassium current, $I_{K,ATP}$,[105] which activates when adenosine triphosphate concentration in the cytosol ($[ATP]_i$) is reduced and the adenosine diphosphate concentration ($[ADP]_i$) is increased. During ischemia phase 1b, changes in $[K^+]_e$ are moderate while acidosis and hypoxia worsen.[99] Cytosolic Na^+ accumulates secondary to the inhibition of sodium-calcium exchanger (I_{NaCa}) and the sodium-potassium pump (I_{NaK}). In addition, ATP depletion and pH reduction reduce both release current strength of ryanodine receptor channels (g_{RyR}) as well as calcium uptake into the sarcoplasmic reticulum, (ν_{up}),[106–109] which leads to cellular calcium overload. Metabolic inhibition is also known to augment the background calcium current, $I_{Ca,B}$, and the calcium-sensitive nonselective cation current, $I_{ns,Ca}$.[99] However, since $I_{ns,Ca}$ and $I_{Ca,B}$ were not included in the MSH model formulation and considering that these currents are fairly small compared to the other currents, they were not taken into account. Parameter modifications to reflect phase 1b conditions were obtained based on the range of values during acute ischemia.[99, 100, 105] A summary of all parameters of cardiomyocytes under normal as well as ischemic conditions can be found in Tab. 4.1.

Table 4.1: Model parameters for myocytes under normal and different stages of ischemia.

Parameter		*Stage of ischemia (min)*				
		0	**5**	**10**	**15**	**30**
		control	*phase 1a*		*phase 1b*	
Hyperkalemia						
$[K^+]_e$	(mmol/l)	5.4	8.9	12.5	14	15.5
Acidosis						
g_{Ca}	(%)	100	87.5	75	50	50
g_{Na}	(%)	100	87.5	75	50	50
$V_{s,Na}$	(mV)	0	1.7	3.4	3.4	3.4
I_{NaCa}	(%)	100	100	100	60	20
Acidosis & Hypoxia						
$[Na^+]_i$	(mmol/l)	14	14	14	17	20
I_{NaK}	(%)	100	100	100	65	30
g_{RyR}	(%)	100	100	100	50	5
ν_{up}	(%)	100	100	100	95	90
Hypoxia						
$[ATP]_i$	(mmol/l)	6.8	5.7	4.6	3.5	2.0
$[ADP]_i$	(μmol/l)	15	57	99	136	164

4.2 Modeling Superfused-induced Ischemia in Multicellular Preparations

4.2.1 Pseudo-1D Model of an Ischemic Multicellular Strand

A computer model of a 5 mm long strand of cardiac tissue with a diameter of 25μm was developed to assess the impact of ischemia-related changes upon impulse propagation at the tissue scale. The model geometry which is close to 1D, was discretized at a spatial resolution of $25\,\mu$m using 3D hexahedral finite elements. Although 3D elements are employed, due to diameter which is small compared to the length of the preparation, the strand can be considered to behave like a 1D structure. During each simulation run, a particular condition, i.e., control, hyperkalemia, acidosis, hypoxia or ischemia at various stages, was assigned to the entire strand, where for each condition the MSH model was modified according to Tab. 4.1. In addition to cellular scale adaptations, progression of ischemia also induces a host of changes which effect electrophysiological properties at

the tissue scale. Myocyte and vascular morphologies are altered, which, in turn, affect the conductivity $\boldsymbol{\sigma_e}$ of the extracellular matrix.[110,111] Further, during ischemia phase 1b considerable dephosplorylation of Cx43 takes places due to prolonged acidification, leading to the progressive closure of gap junctions.[107] These changes are reflected in a reduced intracellular bidomain conductivity $\boldsymbol{\sigma_i}$.[104,112] Both $\boldsymbol{\sigma_i}$ and $\boldsymbol{\sigma_e}$ (Eqs. 3.19-3.20 in p. 35) were further reduced to model the extreme case of irreversible cell damage, referred to as myolysis. Based on experimental measurements[110,113] the relative changes in $\boldsymbol{\sigma_i}$ and $\boldsymbol{\sigma_e}$ for different stages of ischemia and myolysis are summarized in Tab. 4.2.

Table 4.2: Changes in extracellular ($\boldsymbol{\sigma_e}$) and intracellular ($\boldsymbol{\sigma_i}$) conductivities.

Parameter	Stage of ischemia (min)					
	0	5	10	15	30	> 30
	control	phase 1a		phase 1b		myolysis
$\boldsymbol{\sigma_e}$ (%)	100	75	65	60	55	50
$\boldsymbol{\sigma_i}$ (%)	100	100	100	80	50	10

4.2.2 Radially Symmetric Model of a Superfused Muscle Strip

A finite element model of a thin-walled tissue preparation was developed to study effects of ischemia-induced heterogeneities in the depth of the tissue upon activation sequence, AP morphology and extracellularly recorded depolarization signals. In this work, a geometry representative of cardiac muscle strips such as pectinate (as shown in Fig. 2.14 B, p. 22), trabecular and papillary (e.g. Fig. 2.13 A in p. 20) muscles was chosen since they are often employed to investigate the physiological functions of the heart.[54,59,114] In particular, rabbit papillary muscles have lengths that are between 3.5 mm and 5 mm long with diameter of ∼1 mm.[115–117] Based on that, a cylindrical approximation of the muscle's geometry of 5 mm length and 0.5 mm radius was generated (Fig. 4.1 A). The model was composed of 35,498 nodes and 193,567 tetrahedral elements of 62.42 μm average edge length and a maximum aspect ratio* of 4.14.[64] The preferred axis of conduction was assumed to be aligned with the y-axis, i.e., the main axis of the cylinder. The thin-walled muscle was immersed in a bath of dimensions $11 \times 15 \times 7$ mm^3 to mirror relevant aspects of experimental set-ups employing superfusion.[22,118] It was positioned 1 mm above the bottom of the bath and centered in the x-y plane. 83,766 nodes and 464,891 tetrahedral elements of 185.02 μm average edge length and a maximum aspect ratio of 5.18 were used to discretize the bath.

---

*The aspect ratio of an element is given by l_{max}/l_{min}, where l_{max} and l_{min} refer to the longest and shortest edge lengths, respectively. It is used to quantify the degree that mesh elements are stretched.[64]
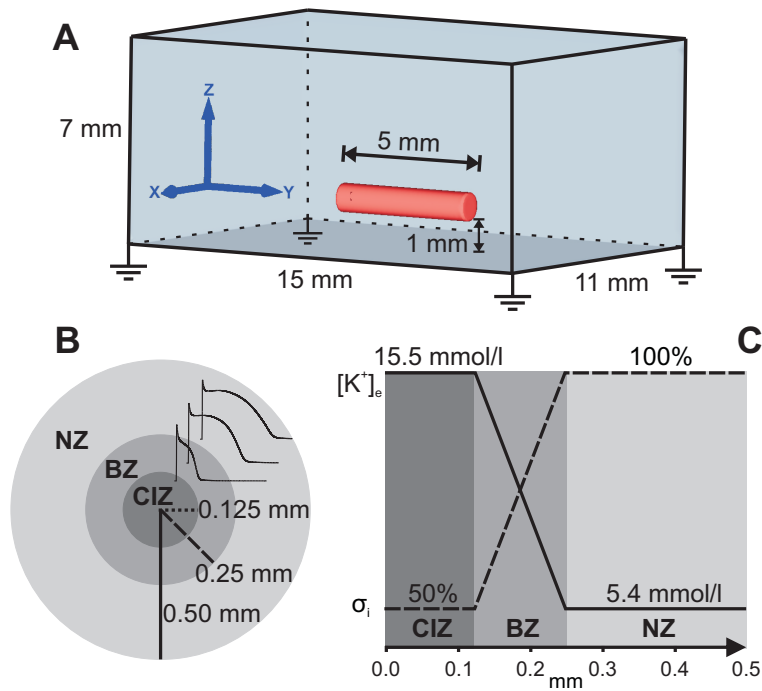
Figure 4.1: (A) Finite element model of a thin-walled cardiac sample, resembling the pectinate muscle in Fig. 2.14 B, immersed in a bath with four symmetrically arranged grounding electrodes. (B) Cross section of the muscle preparation in (A) showing APs from central ischemic zone (CIZ), border zone (BZ) and normal zone (NZ). (C) Gradients of extracellular potassium concentration $[K^+]_e$ and intracellular conductivity $\boldsymbol{\sigma_i}$ along the radial axis. Values for $[K^+]_e$ and $\boldsymbol{\sigma_i}$ in the CIZ and NZ are assigned according to ischemia phase 1b (30 min) and control, respectively (Tabs. 4.1-4.2).

The assessment of transmural inhomogeneities of $[K^+]_e$, pH and myocardial energy metabolism in the heart during ischemia have been the focus of many experimental studies.[119–121] Accordingly, spatial heterogeneity secondary to the progression of ischemia was accounted for by assigning different sets of parameters to the central ischemic zone (CIZ), the border zone (BZ)[122] surrounding the CIZ and the normal zone (NZ). The size of the NZ, within which superfusion is sufficient to avoid any impairment of physiological function, was chosen assuming a maximum diffusion depth of 250 μm.[123] The remaining core of the muscle was subdivided into a BZ of 125 μm radius enclosing the CIZ (Fig. 4.1B). In the NZ, parameters were set according to control conditions to represent viable surface layers. In the CIZ, on the other hand, the same adjustments to cellular properties as well as $\boldsymbol{\sigma_e}$ and $\boldsymbol{\sigma_i}$ were made as before in the set-up of the 1D strand to account for different stages of ischemia. In the BZ, as depicted in Fig. 4.1C, parameters were linearly interpolated between NZ and CIZ.[101, 104, 124]

Six tissue simulations were conducted to study the effects of progressive ischemia in the CIZ using the parameters detailed in Tabs. 4.1 and 4.2: control at 0 min with the entire cross section of the muscle intact; ischemic phase 1a (at 5 min and 10 min); and phase

1b (at 15 min and 30 min). At last, one simulation was conducted to assess a worst case scenario, i.e. the onset of irreversible cell damage in the whole core of the preparation: myolysis. In this extreme scenario, electrophysiological parameters in both CIZ and BZ were assigned according to phase 1b 30 min stage, but $\boldsymbol{\sigma_i}$ and $\boldsymbol{\sigma_e}$ were reduced to 10% and to 50%, respectively, of the values used in control.

4.3 Image-based Tissue Models

4.3.1 Tissue Preparations

Rabbits were anesthetized with 5-10 mg/kg propofol and 20 μg/kg fentanyl and sacrificed according to the National Ethic Guidelines. Hearts were quickly excised and immersed in modified and oxygenated Tyrode's solution at 1-3° C. The solution contained (in mmol/l): NaCl 132.1, KCl 2.7, CaCl$_2$ 2.5, MgCl2$_2$1.15, NaHCO$_3$ 24, NaH$_2$PO$_4$ 0.42, and D-glucose 5.6. The right atrium including the intact SAN was dissected, trimmed to the ROI and pinned down with needles on a transparent rubber carrier. Afterwards the tissue was placed in a bath and superfused with oxygenated Tyrode's solution at 36.4° C. The preparations remained autorhythmic with sinus rhythm during the whole experiment.

4.3.2 Electrophysiological Experiments

Experiments carried out with rabbit right atria were used as either input for the image-based models or as basis for comparison with simulation results. Unipolar extracellular potentials ϕ_e were measured with custom designed flexible multielectrode sensors[22] capable of floating with the small displacement of the tissue during contraction. Each sensor comprises four quadratically arranged Ag/AgCl-electrodes with 18 μm diameter and with 50 μm interelectrode spacing. Extracellular potentials were derived with respect to a circular Ag/AgCl reference electrode at the bottom of the tissue bath. The sensors with pre-amplifiers were mounted on micromanipulators and positioned at given recording sites on the tissue surface. Common procedure was to use two sensors: one kept stationary at the proximal or distal end of a PM and a second one consecutively positioned along the muscle for time serial mapping of ϕ_e. Tissue topology and recording sites were documented with a digital camera (Olympus C-5060 WZ, Olympus Corp., Japan). A tungsten recording electrode was placed close to the sinus node to detect the sinus rhythm and to obtain a trigger source for beat-to-beat online monitoring of ϕ_e. Signals were amplified by custom-designed differential amplifiers (gain 100) and lowpass filtered (-3 dB point at 20 kHz). A PXI based data acquisition system (NI PXI-6123, National Instruments, Austin, Texas) was used to digitize signals at a rate of 100 kHz per channel and 16 bit resolution.

4.3.3 Macro Model of the ROI

An image (1 280 x 960 pixels) accounting for the gross morphological features of the right atrial isthmus of an adult rabbit was taken to build a macroscopic model of the ROI. As shown in Fig. 4.2 A, the gross anatomy is characterized at a macroscopic size scale by fiber bundles such as the CT and PMs which are attached to the endocardium of the RA.
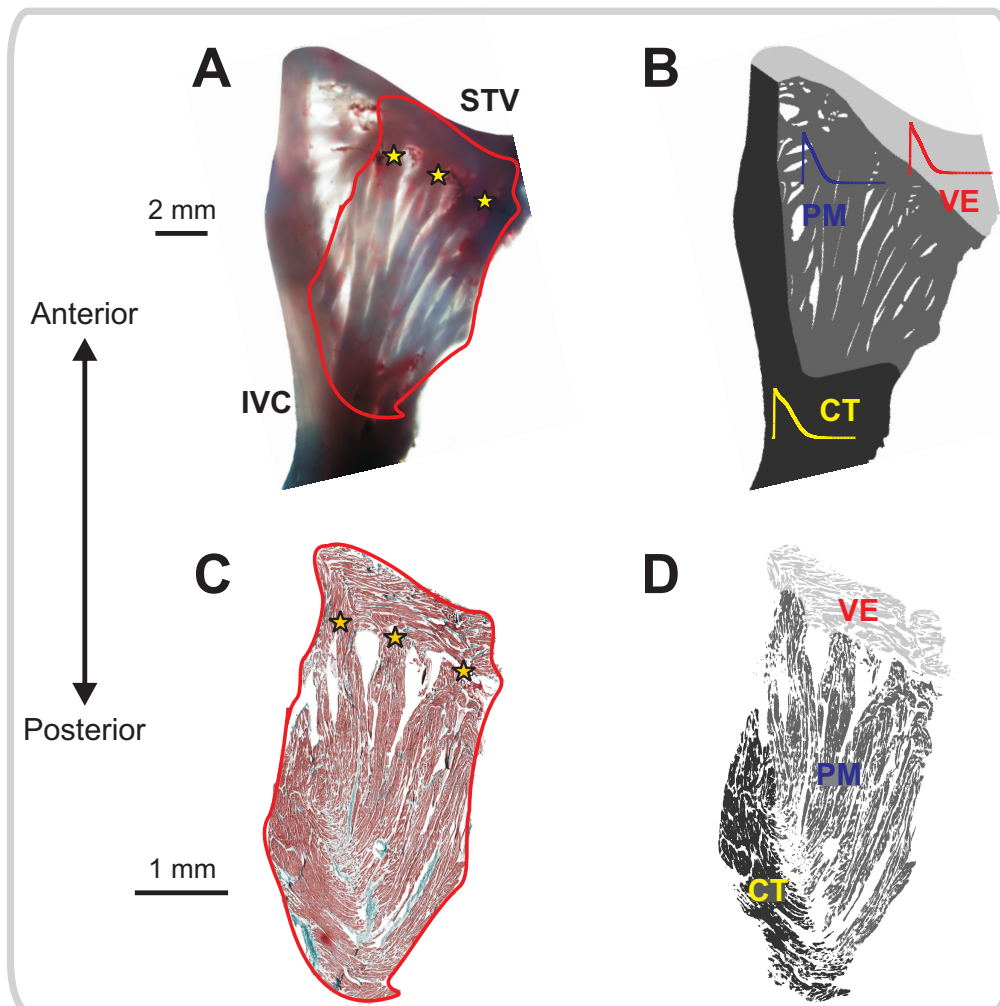
Figure 4.2: (A) Macro-image of the rabbit right atrial isthmus in respect to the inferior vena cava (IVC) and the septum tricuspidal valve (STV). (B) Segmentation of the image in (A) showing the three main components of the ROI and their respective AP shapes: crista terminalis (CT), pectinate muscles (PMs) and the vestibule (VE). (C) High resolution histological image of the selected area in (A). The staining (Masson's trichrome) resulted in a coloring of myocytes (red), connective tissue (blue) and interstitial cleft spaces (white). (D) Segmentation of the histograph shown in (C). Macro- and histological images kindly provided by Dr. Damián Sánchez-Quintana[†]. Segmented images were obtained with the help of Dr. Helmut Ahammer[‡].

[†]Departamento de Anatomía, Biología Celular y Zoología, Universidad de Extremadura, Spain.

[‡]Institute of Biophysics, Medical University of Graz, Austria.

The myocardium was segmented in the hue, saturation and lightness (HSL) color space by setting proper thresholds and translated into an hexahedral FE mesh. In total, 116 048 nodes with a space discretization of 45 μm were required to capture the macrostructure in a $\sim$ 12.1 x 17.0 mm^2 area of tissue. Each element of the mesh was tagged with the help of Dr. Damián Sánchez-Quintana* in order to identify whether it belongs to the crista terminalis, to a pectinate muscle or to the vestibule (see Fig. 4.2 B). The membrane kinetics in atrial myocytes (rabbit) developed by Aslanidi *et al.*[4] were assigned to the 2D tissue model to account for the functional heterogeneities known to exist in the isthmus.

Macroscopic fiber orientations were incorporated to the model by solving a Laplace equation[96] (Sect. 3.2.3, p. 38). Appropriate sources and sinks were chosen such that the resultant electric field follows the macro-geometry. The unit electric field vectors were then used to assign fiber direction to each finite element in the model.

4.3.4 Micro Model of the ROI

Histological Tissue Slices

Tissue samples containing the full thicknesses of the isthmus were excised from the atrium. The samples were immediately fixed in 7% neutral buffered formaldehyde and subsequently dehydrated, embedded in paraffin, and serially sectioned parallel to the septal leaflet of the tricuspid valve at a thickness of 7 μm with a microtome (Microm HM310, Thermo Fisher Scientific, Walldorf, Germany). Finally, the sections were stained with Masson's trichrome protocol resulting in a coloring of muscle cells in red, collagen fibers in blue, and intercellular clefts appearing in white.

Image Processing

Tissue slices that were sufficiently representative of the ROI were then scanned at high resolution (San Scope, Aperio, Vista CA, USA) in SVS file format. The digital images were cropped and reduced in resolution in order to keep the size of the finite element meshes tractable. In this work, two atrial tissue slices obtained from different hearts were chosen to build microscopic models of the ROI: Fig. 2.4 B (see p. 9) with 458 x 670 pixels, where the Vestibule is not present, and Fig. 4.2 C with 696 x 1288 pixels, respectively.

The digitized images were segmented using color clustering and thresholding techniques to distinguish myocardium (red) from connective tissue (blue) and intercellular clefts (white). Finally, the microscopic fiber orientations were obtained using an image intensity gradient method.[94]

---

*Departamento de Anatomía, Biología Celular y Zoología, Universidad de Extremadura, Spain.

Mesh Generation

The FE meshes were generated directly from the segmented histological images shown in Fig. 2.4 B (see p. 9, also shown in Fig. 4.4) and Fig. 4.2 C (in p. 46). In the process, each pixel segmented as a myocyte was meshed as an hexahedral element whereas pixels segmented as uncoupling structures (clefts or connective tissue) were not represented in the mesh.[11,67] These 2D models reveal the complexity of activation patterns caused by the microstructure, but do not reflect the shunting effects of subsequent layers of tissue in 3D. In order to alleviate such a drawback, a second (shunting) layer of cardiac tissue was added based on the same histograph, but neglecting some microscopic details (see Fig. 4.3). Fiber orientations were considered to be the same as in the upper histological layer but the coupling, i.e., the conductivity tensor $\boldsymbol{\sigma_m}$ in Eq. 3.34, p. 37, was successively reduced until a value 100x smaller. The inclusion of the shunting layer with a smaller electrical conductivity allows electrical propagation into regions that were disconnected by the 2D model while avoiding undesired shortcuts.
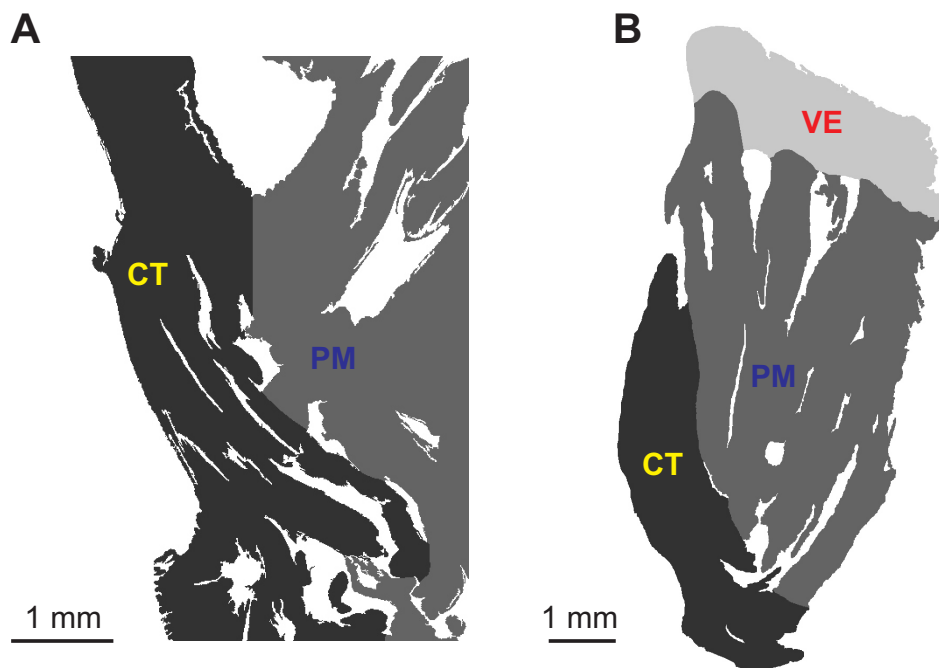
Figure 4.3: Shunting layers used to mimic the effects of tissue in 3D. (A) Shunting layer established based on the histograph in Fig. 2.4 B (p. 9), but neglecting some microscopic details. (B) Shunting layer related to the histological image in Fig. 4.2 C (p. 46).

As in the macroscopic model, each element of the mesh was tagged and assigned to a specific atrial cell model to account for the differences in APs within the ROI[4] (see Fig. 4.2 D). In summary, 923 967 nodes with a space discretization of 9 μm and 613 720 hexahedral elements were required to build a microscopic model based on the histograph shown in Fig. 2.4 B, p. 9; and 2 695 299 nodes (8 μm) and 1 792 896 elements were required to set the microscopic model based on the histograph shown in Fig. 4.2 C, p. 46.

4.4 Simulation Protocols

4.4.1 Single-cell Simulations

Both Aslanidi and MSH models were solved using the Rush-Larsen method, with a time step of $10\,\mu s$.[125] Initial conditions for both atrial (CT, PM and VE) and ventricular myocytes were computed by pacing a single cell at a basic cycle length (BCL) of $500\,ms$ ($2\,Hz$). Pacing was terminated when arriving at a stable limit cycle where differences in AP features between subsequent beats were small ($< 1\%$, see Sect. 4.5 for further details about AP features). The state variables at the end of the protocol for each case were stored to be used as an input for the tissue simulations. Regarding the radially symmetric model of a superfused muscle strip, initial conditions for the ischemic myocyte model in the regions NZ, BZ and CIZ were also obtained for the instants $0\,min$, $5\,min$, $10\,min$, $15\,min$ and $30\,min$ using cellular parameters as given in Tab. 4.1 (see p. 42).

4.4.2 Radially Symmetric Model of a Superfused Muscle Strip

The bidomain model was used to simulate the electrical activity in multicellular strands (1D as well as in the radially symmetric model). Bidomain parameters were taken from the literature:[66] membrane capacitance $C_m = 1\,\mu F/cm^2$, surface-to-volume ratio $\beta = 0.14\,\mu m^{-1}$ and the conductivities $\sigma_{il} = 0.174\,S/m$, $\sigma_{it} = 0.019\,S/m$, $\sigma_{el} = 0.625\,S/m$ and $\sigma_{et} = 0.236\,S/m$ where the indices i and e indicate intracellular and extracellular, and l and t the longitudinal and transverse direction, respectively. The surrounding bath was considered isotropic with conductivity $\sigma_b = 1\,S/m$.

In the 1D case, a transmembrane current stimulus was applied at one end of the cable. In the radially symmetric case, on the other hand, the left top cusp of the muscle was stimulated as shown in Fig. 4.6 A, p. 52. Four symmetrically arranged grounding electrodes were placed at the lower corners of the bath (see Fig. 4.1 A, p. 44). To ensure steady-state at the tissue scale, the phase 1b set-up (which is the model with the most pronounced AP heterogeneity) was paced seven times at a BCL of $500\,ms$ after initialization with the single-cell steady-state values. Limit cycle trajectories were verified by recording APs in all three regions NZ, BZ and CIZ within the central cross sectional plane of the muscle. Differences in AP morphologies (using metrics as described in Sect. 4.5, p. 52) between the last two paced beats at all three sites were negligible. After administering 2 stimuli, differences between two subsequent APs were $< 3\%$. Therefore, for all other cases under study, only two pacing stimuli were delivered to arrive at a limit cycle.

4.4.3 2D Histologically Detailed Models

Due to the fine spatial and temporal discretizations required to solve the image-based models, the monodomain equations were used to simulate the spread of the electrical activation in the atrial isthmus. Tissue conductivity values from the literature[66] have been uniformly rescaled to match the reported conduction velocities in pectinate muscles from adult rabbits.[126] If not stated different, a transmembrane current was applied at the CT close to the SAN.

Multisite Pacing
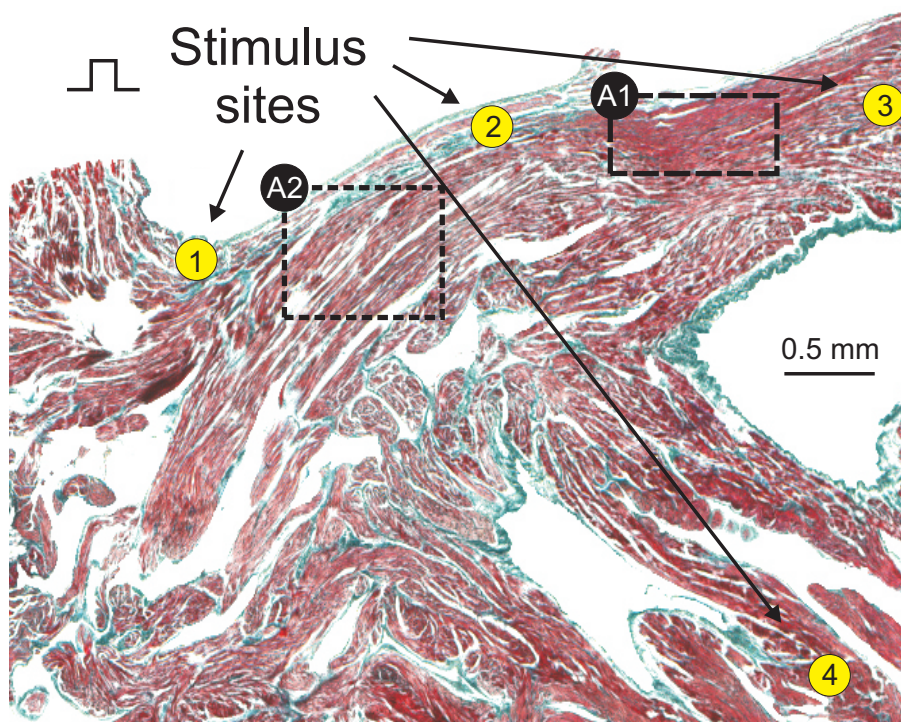
Figure 4.4: Histograph of the selected area in Fig. 2.4 A. Subregions A1 and A2 relate to two types of configuration of microstructure: A1 - well coupled densely packed tissue and, A2 - uncoupled tissue with uncoupling structures oriented parallel to the cardiac fibers. One simulation was performed for each of the stimulus sites indicated. Figure adapted from Campos *et al.*[11]

In order to investigate the occurrence of fractionated electrograms and their dependence on the direction of the depolarization wavefront, four simulations were performed using the microscopic model of the ROI based on the histograph shown in Fig. 4.4. A stimulus current was applied at four different sites (see Fig. 4.4): STIM1, close to the SAN causing an antegrade propagation along the CT; STIM2, causing transverse propagation within fiber bundles within the CT; STIM3, located distal to the SAN in order to produce retrograde conduction in the CT; and STIM4, placed at a PM producing a ret-

rograde conduction in it. All simulations were carried out for 30 ms computing only the depolarization phase after the stimulus. Two subregions A1 and A2 representing different spatial organization of microstructure are demarcated. Extracellular recorded signals within these two subregions are of particular interest in this thesis and thus, analyzed in Chap. 5.

Circumferential Stimulation

In order to investigate the occurrence of fractionated electrograms and their dependence on the direction of the depolarization wavefront, stimulus currents were applied to the tissue at different sites. As depicted in Fig. 4.5, a stimulus current was injected at points forming a virtual ring surrounding the tissue section under investigation. In total, twelve simulations (one per stimulus site) were performed for each of the six tissue samples under investigation.
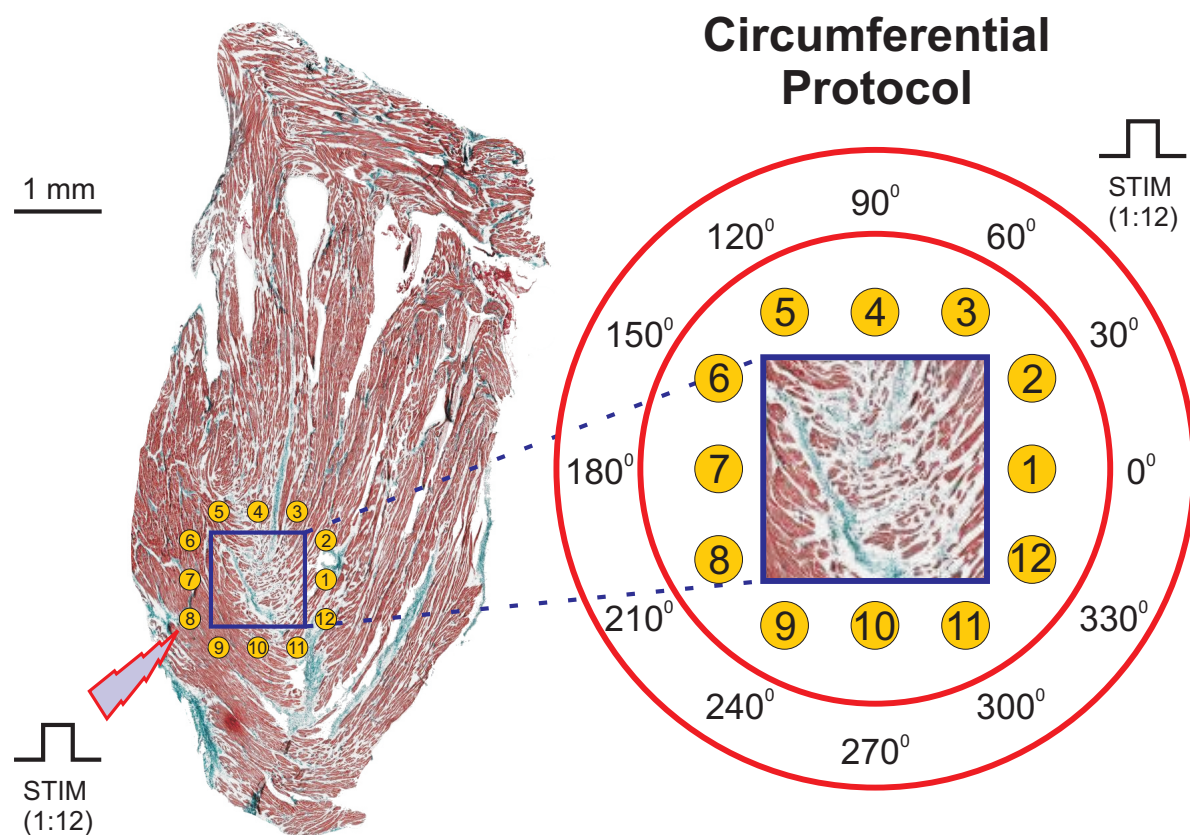
Figure 4.5: Illustration of the circumferential protocol: 12 stimulus sites forming a virtual ring around the tissue sample under investigation. Each stimulus (STIM) relate to one sole simulation. Histological image kindly provided by Dr. Damián Sánchez-Quintana[†].

[†]Departamento de Anatomía, Biología Celular y Zoología, Universidad de Extremadura, Spain.

4.5 Data Analysis

4.5.1 Action Potentials

APs were taken from the central cross-sectional area of the radially symmetric model (see Fig. 4.6) to avoid boundary artifacts. APs from the CIZ were also considered for analysis. The following AP features were evaluated: resting potential ($V_{m_{rest}}$), action potential amplitude (APA), maximum upstroke velocity ($\hat{\dot{V}}_m$) and AP duration at 90% of repolarization (APD_{90}). APD_{90} was calculated as the difference between the activation time and the repolarization time. The activation time was determined as the instant of $\hat{\dot{V}}_m$ of the AP. The repolarization time was calculated as the time which the AP waveform crossed a level corresponding to 90% of repolarization to the resting potential.
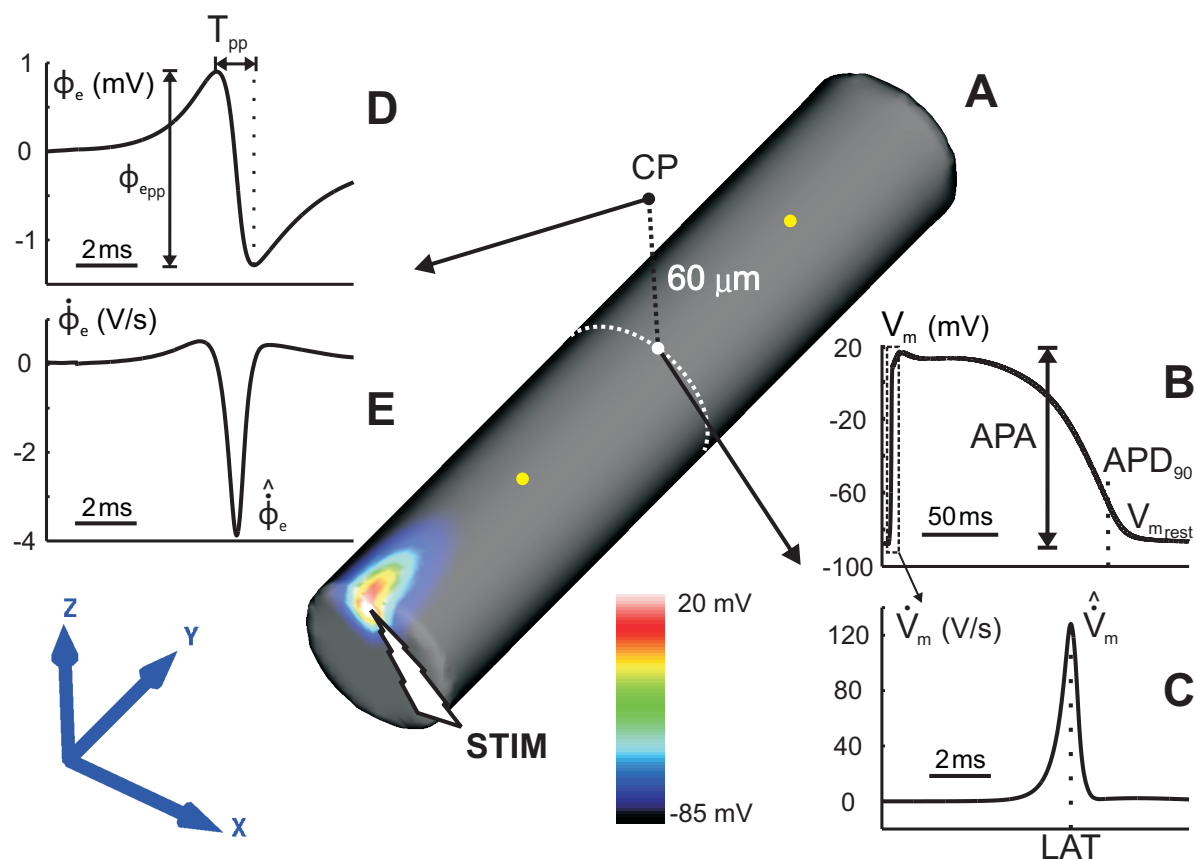
Figure 4.6: (A) Spatial distribution of V_m in the control model 1 ms after stimulation (STIM) at the left top cusp. Yellow dots indicate the location of the recording sites used to determine conduction velocity (CV). (B) Action potential at the surface of the NZ. (C) Time derivative of V_m during an AP. (D) ϕ_e signals at the observation point (CP) at 60 μm above the muscle's surface. (E) Time derivative of ϕ_e.

4.5.2 Extracellular Potentials

Radially Symmetric Model of a Superfused Muscle Strip

Extracellular signals ϕ_e at the observation point (CP) were taken for analysis (Fig. 4.6). The distance of $60\,\mu$m to the surface was chosen to match new contact recording systems for extracellular potentials.[22] Other conduction parameters based on extracellular potentials, such as the amplitude $\phi_{e_{pp}}$ of the biphasic signal ϕ_e calculated as the difference between its positive and negative peaks, the time difference between these two peaks T_{PP} and the negative peak of the time derivative $\dot{\hat{\phi}}_e$ were evaluated. Fig. 4.6 summarizes all features which were used to characterize both V_m and ϕ_e dynamics.

Image-based Models

Grids of points spaced by one cell length ($\sim 100\,\mu$m) following the macroscopic structures of the underlying tissue, like shown in Fig. 4.7 A, were defined for all image-based models. Each of these points represents the center of a square CNF sensor with $50\,\mu$m lateral length (see Fig. 4.7 B). Since the monodomain equations describe only current flow in the intracellular medium of the cardiac tissue, electrograms (ϕ_e) were recovered in the middle and at the vertices of each electrode according to Eq. 3.38. As in the radially symmetric model of a cable-like muscle, all signals were computed $60\,\mu$m above the tissue surface.[22]

Fractionation Index (FI): in addition to the conduction parameters based on ϕ_e described above (Sect. 4.5.2 in p. 53), the fractionation indices, i.e., the number of negative peaks of $\dot{\phi}_e$ were calculated by an extrema-finding algorithm. Deflections smaller than 10% of the signal peak-to-peak amplitude of $\dot{\phi}_e$ were ignored. FI is used here as a measure of complexity, since it indicates the number of superimposed events within ϕ_e.

4.5.3 Cardiac Near Field (CNF)

For the estimation of the components of the electrical field strength $\boldsymbol{E} = [E_x\ E_y]^T$ in x and y direction two signals of diagonally placed electrodes are used, respectively (see Fig. 4.7 B). The potential difference divided by the diagonal distance DD between two electrodes results in:

$$\boldsymbol{E} = \boldsymbol{A}(\alpha) \cdot \begin{bmatrix} E_x \\ E_y \end{bmatrix} = \boldsymbol{A}(\alpha) \cdot \begin{bmatrix} \frac{\phi_{e_3}-\phi_{e_2}}{DD} \\ \frac{\phi_{e_4}-\phi_{e_1}}{DD} \end{bmatrix} \tag{4.1}$$

where $\boldsymbol{A}(\alpha)$ is the rotation matrix given by:

$$\boldsymbol{A}(\alpha) = \begin{bmatrix} cos(\alpha) & -sin(\alpha) \\ sin(\alpha) & cos(\alpha) \end{bmatrix} \tag{4.2}$$
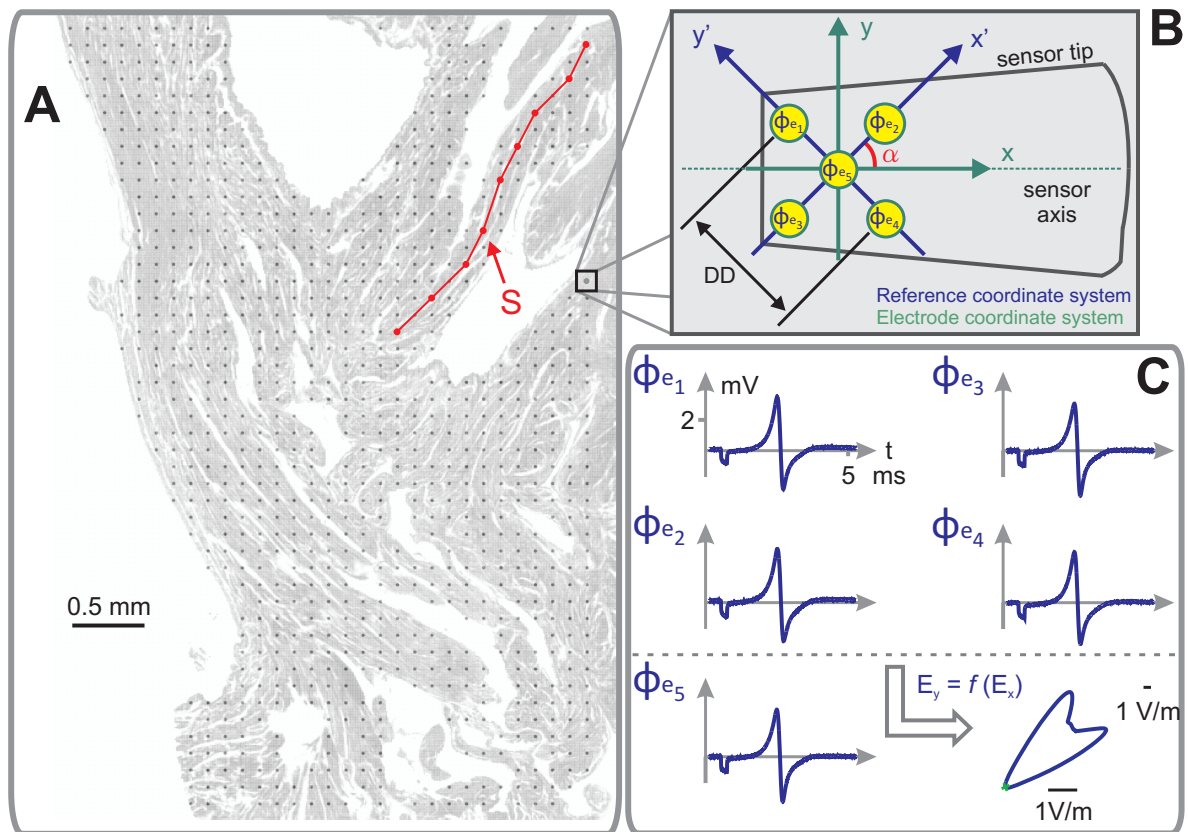
Figure 4.7: (A) Grid established to recover extracellular potentials ϕ_e in the microscopic model based on the high resolution histological image shown in Fig. 4.4. Each point represents the center of a CNF sensor. An example of a pathway **S** used to compute conduction velocity along a PM. (B) Square five-electrode array representing a CNF sensor. (C) Electrograms recovered according to the CNF sensor array in (B) and the vector-loop constructed based on signals $\phi_{e_1} \dots \phi_{e_4}$. Figure kindly provided by Dr. Ernst Hofer[‡].

The reference coordinate system xy' is rotated clockwise by the correction angle α with respect to the sensor axis xy. Thus, $\boldsymbol{A}(\alpha)$ has to be considered to transform a propagation angle φ determined within the coordinate system xy' into coordinate system xy.[52] The correction angle in Fig. 4.7 B, for instance, is $\alpha = \pi/4$.

The peak magnitude $\hat{E}$ as well as the direction $\hat{\varphi}$ (obtained based on the vector-loops constructed by plotting $E_y = f(E_x)$, as depicted in Fig. 4.7) were considered to characterize the CNF $\boldsymbol{E}$.

4.5.4 Conduction Velocity (CV)

Conduction velocity (CV) in cable-like model shown in Fig. 4.6 A, p. 52, was simply obtained by dividing the distance between two locations by the difference in arrival times.

[‡]Institute of Biophysics, Medical University of Graz, Austria.

In the macro and micro models of the ROI, on the other hand, CV along pectinate muscles was examined by taking the local activation time (LAT), as the time of $\hat{\phi}_e$, and a path length **S** (see Fig. 4.7 A) along the muscle creating time-distance diagrams. Mean CV was then estimated by linear regression.[126]

Local Conduction Velocity (LCV)

To estimate the local velocity vector $\boldsymbol{v} = [dx/dt,\, dy/dt]^T$ of a point on a wavefront, a procedure similar to the mapping analysis of Bayly *et al.*[127] for multisite recordings was used. First, electrograms were recovered in a grid of points representing the center of square sensors following the macroscopic structures of the underlying tissue (see Fig. 4.7 A). Second, LATs were estimated from $\hat{\phi}_e$. The set of LATs describes the activation at a recording site (x, y). A surface $T(x, y)$ can thus be fitted to this set of discrete values using an interpolation technique. Sections through this surface at constant time are isochronal contours. The isochrone for a specific activation time, e.g. t_i, is defined by the solution of the equation $T(x, y) = t_i$. If $P(x, y)$ is a point lying on the isochrone, then the total differential dT_1 must be zero proceeding from $P(x, y)$ along the isochrone. If dx_1 and dy_1 are taken in such a way that the vector $[dx_1,\, dy_1]^T$ is tangent to the isochrone, thus

$$dT_1 = \frac{\partial T}{\partial x}\, dx_1 + \frac{\partial T}{\partial y}\, dy_1 = 0 \tag{4.3}$$

Hence, the slope of the isochrone in the x-y plane is given by

$$\frac{dy_1}{dx_1} = -\frac{\partial T/\partial x}{\partial T/\partial y} \tag{4.4}$$

The excitation spread occurs along the gradient $\nabla T(x, y)$ and is perpendicular to the direction calculated in Eq. 4.4. Therefore, the slope in this direction is

$$\frac{dy_2}{dx_2} = -\frac{1}{dy_1/dx_1} = \frac{\partial T/\partial y}{\partial T/\partial x} \tag{4.5}$$

Along this direction the total differential is again analog to the relationship in Eq. 4.3, but non-zero:

$$dT_2 = \frac{\partial T}{\partial x}\, dx_2 + \frac{\partial T}{\partial y}\, dy_2 \tag{4.6}$$

The local velocity vector $\boldsymbol{v}$ can be estimated dividing the way which the excitation has traveled $[dx_2,\, dy_2]^T$ by the isochrone interval dT_2. From Eq. 4.6 it can be seen that

$$\frac{dT_2}{dx_2} = \frac{\partial T}{\partial x} + \frac{\partial T}{\partial y}\frac{dy_2}{dx_2} \tag{4.7}$$

Substituting Eq. 4.5 in Eq. 4.7:

$$\frac{dT_2}{dx_2} = \frac{\partial T}{\partial x} + \frac{\partial T}{\partial y}\left(\frac{\partial T/\partial y}{\partial T/\partial x}\right) \tag{4.8}$$

Rearranging the terms in Eq. 4.8 and solving for the component of the velocity dx_2/dT_2:

$$\frac{dx_2}{dT_2} = \frac{\partial T/\partial x}{((\partial T/\partial x)^2 + (\partial T/\partial y)^2)} \tag{4.9}$$

The component dy_2/dT_2 can be similarly determined. Therefore, the expression for the local velocity vector $\boldsymbol{v}$ is:

$$\boldsymbol{v} = \begin{bmatrix} dx_2/dT_2 \\ dy_2/dT_2 \end{bmatrix} = \frac{1}{T_x^2 + T_y^2} \begin{bmatrix} T_x \\ T_y \end{bmatrix} \tag{4.10}$$

where $T_x = \partial T/\partial x$ and $T_y = \partial T/\partial y$.

In the work of Bayly *et al.*[127] $T(x,y)$ is a polynomial surface. Thus, the gradient $\nabla T(x,y)$ was obtained analytically. In this thesis, on the other hand, no surface was fitted to the set of discrete values $LAT(x,y)$. The gradient $\nabla LAT(x,y)$ was rather approximated at the center of the sensor (see Fig. 4.7 B, p. 54) using a finite difference approach:[52]

$$\nabla LAT(x,y) = \begin{bmatrix} LAT_x \\ LAT_y \end{bmatrix} = \frac{1}{DD} \begin{bmatrix} LAT_4 - LAT_1 \\ LAT_3 - LAT_2 \end{bmatrix} \tag{4.11}$$

where $LAT_1 \ldots LAT_4$ are local activation times obatined from $\phi_{e_1} \ldots \phi_{e_4}$ in Fig. 4.7 B, p. 54.

Local conduction velocity (LCV) was obtained similarly to Eq. 4.10 as follows:

$$\boldsymbol{v} = \begin{bmatrix} v_x \\ v_y \end{bmatrix} = \frac{1}{LAT_x^2 + LAT_y^2} \begin{bmatrix} LAT_x \\ LAT_y \end{bmatrix} \tag{4.12}$$

and its magnitude $\hat{\theta}$ expressed as:

$$\hat{v} = \sqrt{v_x^2 + v_y^2} \tag{4.13}$$

It is important to point out that Eq. 4.10 remains valid only because the four-measurement sensor forms a rectangular coordinate system.

4.5.5 Classification of Microfibrosis

In the heart, fibrosis is referred to be interstitial, compact, patchy, or diffuse.[7] However, there is no strict rule or quantitative measure to draw a line separating these classes. In this work, fibrotic tissue was identified in the histological images by the amount of uncoupling structures (collagen as well as interstitial clefts) and their spatial orientation with respect to the cardiac fibers.

After visual inspection of the tissue slice in Fig. 4.8, subregions of $1\,\mathrm{mm}^2$ representing three types (classes) of spatial organization of the microstructure were chosen for the classification procedures:

- Well coupled densely packed tissue (WCDP)

- Uncoupled tissue with uncoupling structures oriented parallel to the cardiac fibers (UCPO)

- Uncoupled tissue with multidirectional arrangement of uncoupling structures (UCMO)

In total, six tissue subregions representing two samples of each class were identified.
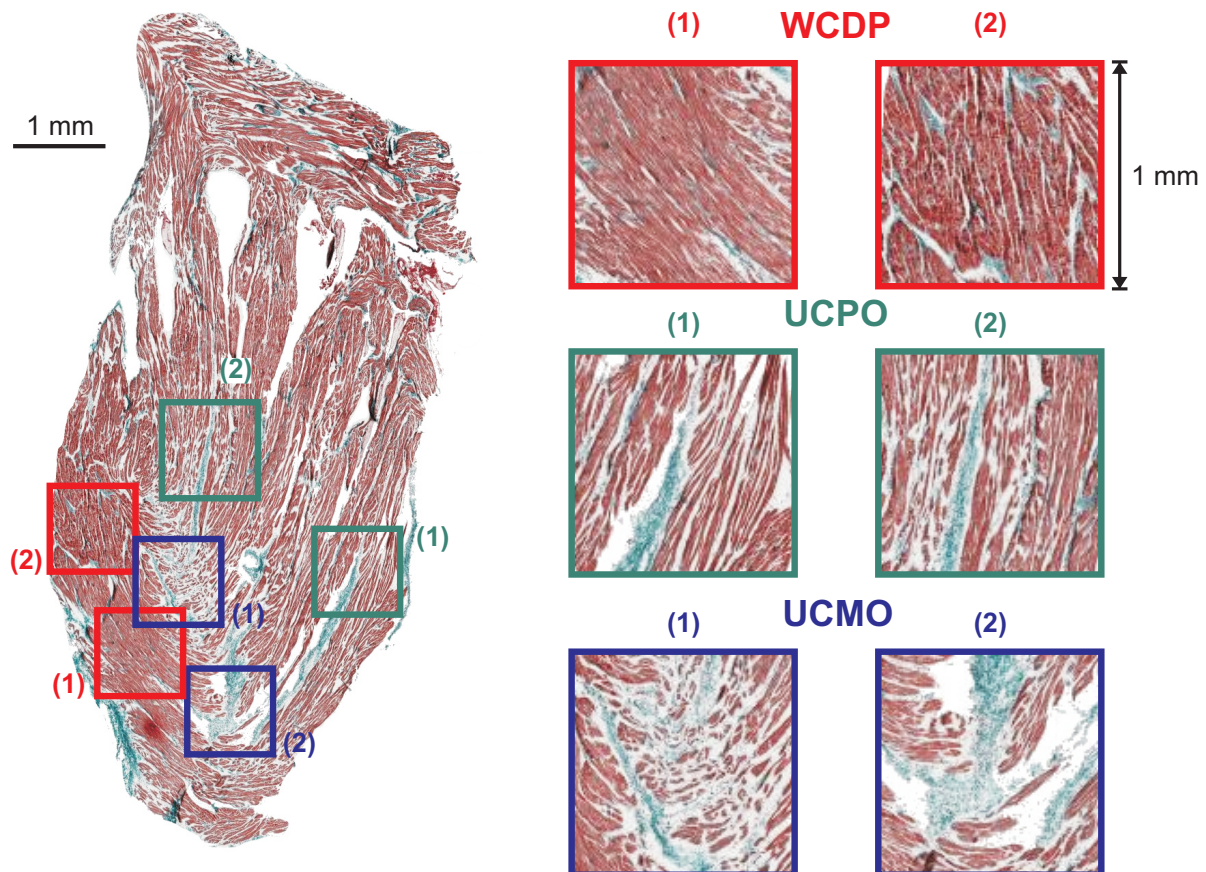
Figure 4.8: Examples three types of spatial organization of cardiac microstructure. From top to bottom: well coupled densely packed tissue (WCDP), uncoupled tissue with uncoupling structures oriented parallel to the cardiac fibers (UCPO), and uncoupled tissue with multidirectional arrangement of uncoupling structures (UCMO). Each subregion accounts for a $1\,\mathrm{mm}^2$ area of myocardium. Histological image kindly provided by Dr. Damián Sánchez-Quintana[§].

Image Processing

Statistics regarding the percentage of myocytes, collagen (fibrosis) and interstitial clefts were computed in order to obtain a more quantitative measure of the degree of fibrosis.

[§]Departamento de Anatomía, Biología Celular y Zoología, Universidad de Extremadura, Spain.

In addition to that, the average of angles of the cardiac myofibers (θ_1) as well as collagen fibers (θ_2) within each subregion was calculated. The deviation between these two angles, as depicted in Fig. 4.9 was considered as a quantitative information about the spatial organization of microfibrosis in relation to the cardiac fibers.
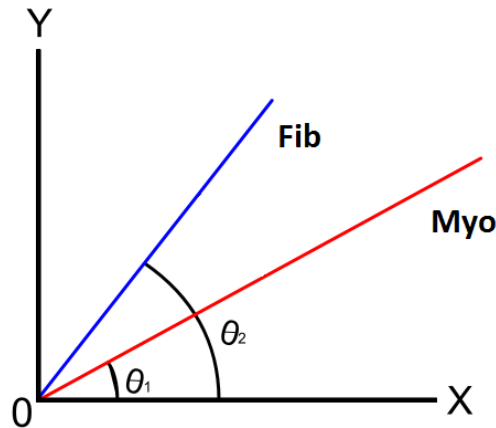
Figure 4.9: Example of angles formed by the cardiac (red) and by collagen (blue) fibers in tissue. Deviation between them was taken as $||\theta_1 - \theta_2||$.

Classification Based on Extracellular Potentials

In this thesis, classification of small tissue samples in terms of their microstructure is sought through inspection of extracellular potentials. The procedure of this classification is as follows: first, computer simulations were conducted using the microscopic model developed based on Fig. 4.8. The circumferential protocol described in Sect. 4.4.3, p. 51 was applied to each of the six subregions under investigation (Fig. 4.8); subsequently, characteristics of extracellular potentials (see Sect. 4.5.2 in p. 53) recovered in all tissue samples were calculated. Moreover, from the acquired set of electrograms ($n = 121$ computed in a $1\,\text{mm}^2$ grid of points spaced by $d = 100\,\mu\text{m}$), FI and $\phi_{e_{pp}}$ were obtained for each of the $s = 12$ stimulus sites (every stimulus represents a single simulation). Thus, the objects, i.e., each of the six $1\,\text{mm}^2$ samples of tissue in Fig. 4.8, can be characterized by FI and $\phi_{e_{pp}}$ of $1\,452$ (121 x 12) electrograms. Means of FI (μ_{FI}) and amplitudes (μ_{amp}) of each set of electrograms ($n = 121$) are taken as lumped information. Based on that, the following three features describing the objects were selected for the classification process:

1. m_{FI}: mean of μ_{FI} over all s stimulus sites.

2. ΔFI: range of μ_{FI} ($\Delta FI = \max\limits_{n_s} \mu_{FI} - \min\limits_{n_s} \mu_{FI}$, where $n_s = 1 \ldots s$).

3. ξ_{amp}: normalized range of μ_{amp}. $\xi_{amp} = \Delta amp / m_{amp}$, where $\Delta amp = \max\limits_{n_s} \mu_{amp} - \min\limits_{n_s} \mu_{amp}$ ($n_s = 1 \ldots s$) and m_{amp} is the mean of μ_{amp} over all s stimulus sites.

The linear discriminant analysis (LDA) was chosen to classify the objects into WCDP, UCPO or UCMO based on the set of features (m_{FI}, ΔFI, ξ_{amp}) described above. LDA assumes that the classes are linearly separable, i.e., the classes can be separated by a linear combination of features describing the objects.[128] Since only three features are considered, the separators among classes are planes.

The classification was cross-validated using leave-one-out method (LOOM)[128] in order to prevent overfitting. LOOM involves using a single object from the set as the validation data, and the remaining objects as the training data. This is repeated such that each object in the set is used once as the validation data. The evaluation criteria were the classification accuracy,[129] i.e., the fraction of correctly classified samples for each class (acc_1 for WCDP, acc_2 for UCPO, and acc_3 for UCMO) as well as the overall accuracy acc_{tot}. acc_i ($i = 1, 2, 3$) is given by:

$$acc_i = \frac{m_i}{n_i} \tag{4.14}$$

where m_i is the number of sample cases of class i correctly classified, and n_i is the total number of samples of class i.

Whereas acc_{tot} is:

$$acc_{tot} = \frac{m_{tot}}{n} \tag{4.15}$$

where m_{tot} is the total number of cases correctly classified, and n the total number of samples.

The sensibility of the classification in respect to the number of stimulus sites s was analyzed. s was set to 6 and 3 maintaining the circumferential protocol. Furthermore, coarser grids with spaced by $d = 200$, 300, 400 and $600\,\mu$m were also evaluated. In the case $s = 6$, the features were computed for stimulus positions $0°$, $60°$, $120°$, $180°$, $240°$ and $300°$. Then, the imaginary ring containing the stimulus electrodes was rotated by $30°$ and the features were again computed. Thus, e.g. for $s = 3$, three feature sets were obtained. In the same manner, for $d = 200\,\mu$m the grid of recording points was shifted in x and y direction by $[x\ y]^T = [100\ 0]\,\mu$m, $[x\ y]^T = [0\ 100]\,\mu$m, and $[x\ y]^T = [100\ 100]\,\mu$m. Thus, e.g. for $d = 200\,\mu$m, four feature sets were obtained.

4.6 Computational Aspects

Both mono- and bidomain equations were solved using the Cardiac Arrhythmia Research package (CARP).[130] Details of the underlying numerical methods have been described in detail elsewhere.[26,66] Simulations were carried out in eight Quad-Core AMD Opteron™ 8386 SE 2.8 GHz processors with 126 GB of RAM running a 64-bit Linux system. Data was stored using a 100 kHz sampling frequency. This work also made use of the facilities of HECToR, the UK's national high-performance computing service,

which is provided by UoE HPCx Ltd at the University of Edinburgh, Cray Inc and NAG Ltd, and funded by the Office of Science and Technology through EPSRC's High End Computing Programme.

4.6.1 Graphic-hardware Solvers for Cardiac Cell Models

To perform simulations of all macro- and microscopic models of the ROI, a large number of ODE systems describing the electrical behavior of cell membranes (Eqs. 3.21-3.22 in p. 35) must be solved contributing substantially to the total computational work.[131, 132] The graphic processing units (GPUs) have become highly parallel processors, which make them a promising alternative to solve the system of ODEs. The reason behind is that GPUs are specialized for compute-intensive, highly parallel computation and therefore designed such that more transistors are devoted to data processing rather than data caching and flow control.[133] More specifically, the GPU is especially well-suited to address problems that can be expressed as data-parallel computations, such as the integration of a large number of systems of ODEs like those associated with cardiac tissue models. In this class of problems, the same program (ODE solver) is executed on many data elements in parallel, with high arithmetic intensity*. Because the same program is executed for each data element, there is a lower requirement for sophisticated flow control; and because it is executed on many data elements and has high arithmetic intensity, the memory access latency can be hidden with calculations instead of big data caches.[133]

To demonstrate the potential of the use GPUs to simulate cardiac cell models, the performance of solvers coded in standard C (CPU) and CUDA (GPU) programming languages was evaluated. The same number of cell models needed to simulated both macro (116 048 nodes) and micro (2 695 299 nodes) models of the ROI were solved using the Rush-Larsen[125] method. The cell model was simulated for 250 ms with a time discretization of 0.25 ms (maximum time step allowed due to stability constraints). The comparison between CPU and GPU solvers is based purely on measuring the total execution time required for a typical integration of the equations.

4.6.2 Implementation Details

In order to obtain high performance using GPU programming some requisites should be kept in mind. The first is the challenge inherent to the development of applications for parallel systems, which should balance the workload and scale it over a number of processors. In addition, differently than in the CPU, the global memory space is not cached in the GPU. Finally, it is also very important to follow the right access pattern to get maximum memory bandwidth.[133]

---

*The ratio of arithmetic operations to memory operations.

A numerical solver of the systems of ODEs described by Eqs. 3.21-3.22, p. 35, in which I_{ion} is given by Eq. 3.15 (the Lindblad model, p. 31) was implemented in both CPU and GPU hardwares. The program for the CPU version was written in C and compiled with GNU C compiler version 4.4.3. In order to exploit the power of the available multi-core processors, the CPU code was parallelized using OpenMP.[134] The code for the GPU was extended from the CPU code to the NVIDIA CUDA parallel environment. Thus, specific CUDA kernels* were developed to solve the system of ODEs. More specifically, two CUDA kernels were implemented: the first one refers to the setting of initial conditions to the systems of ODEs, whereas the second kernel integrates the ODEs at each time step. Fig. 4.10 illustrates the solution algorithm in the GPU, describing memory allocations, computations and data transfers between CPU (host) and GPU (device).

The state variables of M cells were stored in an array SV of size $M * N_{eq}$, where N_{eq} is the number of differential equations of the ionic model (in this work $N_{eq} = 27$ following the Lindblad model). The SV array was organized in such way that the first M entries correspond to the first state variable, followed by M entries of the next state variable, and so on. Moreover, the first M entries of the SV array correspond to the transmembrane potential V_m. In the kernel to set the initial conditions each CUDA thread sets the values of all its state variables. The kernel that solves the system of ODEs operates similarly, i.e., each thread computes and updates its state variables writing to the right position in memory that correspond to their variables.

All CUDA kernels in this work were launched with the number of threads set accordingly to the size of the problem, i.e., accordingly to the number of nodes in the FE mesh. The GPU code was compiled with NVIDIA CUDA 3.2 and single precision was used for all floating point operations. In order to check for possible deviations in the numerical solutions due to the use of single precision in the arithmetic operations, the results (V_m) obtained using single precision were compared against those computed using double precision through the relative root-mean-square norm:

$$RRMS = 100 \, \frac{\sqrt{\sum_t \sum_{i,j} (\upsilon_{i,j}^t - \nu_{i,j}^t)^2}}{\sqrt{\sum_t \sum_{i,j} (\upsilon_{i,j}^t)^2}} \tag{4.16}$$

where υ is the solution computed using double precision, ν is the solution computed using single precision, and t and i, j are indexes in time and space, respectively.

Simulations running on the CPU were performed using OpenMP with 32 cores (eight Quad-Core AMD Opteron$^{\text{TM}}$ 8386 SE 2.8 GHz processors) and compared against simulations running on a single GPU (a NVIDIA GeForce GTX 260, 1 GB graphic-hardware).

---

*Routines designed to run in the GPU in parallel by thousands of threads.

Read mesh and initialize problem parameters on host;

Allocate device memory for the state-variables (ODEs);

Set initial conditions to the ODEs systems;

while *not final time* **do**

    Integrate the ODEs;

    if *writeToDisk* **then**

        Copy Vm from device to host;

        Write Vm into disk on host;

    end

end

Free host and device memory;

CPU	CPU GPU	GPU	GPU CPU
CPU performs the computation.	Copy data from CPU to GPU.	GPU performs the computation.	Copy data from GPU to CPU.

Figure 4.10: Algorithm to solve systems of ODEs on the GPU. Figure adapted from Rocha *et al.*[12]

Chapter 5

Results

This chapter presents the results of the various modeling and simulation studies (strongly related to experimental work) done during the course of this thesis. Material and methods used to achieve the results presented below are described in Chap. 4. This chapter is divided in four sections. First, results obtained with a radially symmetric model representing a muscle bundle from the ROI are presented. The model is a preliminary study aiming to quantify possible limitations of experimental set-ups, where superfusion is the choice to provide the tissue with oxygen supply and waste removal. Second, 2D models of the ROI with different levels of details are presented. Simulation results are compared to data from experiments. Third, the tissue models are used to determine how the microstructural organization of fibrosis in the ROI correlates with electrograms as well as with CNF signals. Multisite pacing was performed and directional effects of wavefronts on electrogram morphology analyzed in different atrial regions representing different types of microstructure. Finally, the performance of a GPU solver to accelerate the simulations of the electrical activity using the models proposed here is evaluated.

5.1 Influence of Ischemic Core Muscle Fibers in a Superfused Cardiac Tissue Preparation

5.1.1 Effects of Ischemia on Impulse Propagation in a Strand

The impact upon impulse propagation of the three main components of ischemia at the cellular scale, i.e. hyperkalemia, acidosis and hypoxia, as well as reduced coupling secondary to dephosphorylation of gap junctions at the tissue scale was studied using a numerical model of a cardiac strand. To assess the relative influence of the individual contributing factors to overall ischemia computer simulations were performed, where the impact of each factor was studied first in separation before combining all of them to form an ischemic strand of tissue.

Fig. 5.1 A reveals how each component affects AP features and CV. Elevated $[K^+]_e$ has the most prominent influence upon $V_{m_{rest}}$, $\hat{V}_m$, APA and CV. CV increased initially with $[K^+]_e$ (from 5.4 mmol/l at 0 min to 8.9 mmol/l at 5 min, see Tab. 4.1 in p. 42), but this trend reversed as hyperkalemia deteriorated until conduction block occurred at $[K^+]_e > 8.9$ mmol/l, i.e., after 10 min. APA and $\hat{V}_m$ monotonically decreased whereas APD$_{90}$ was prolonged up to 12.6% before conduction block. In contrast, acidosis led to a monotonic decrease in $\hat{V}_m$, APA, APD$_{90}$ and CV over the first 15 min, while remaining constant afterwards. Hypoxia was the major determinant of APD shortening (from 148 ms under control conditions to 10 ms at t = 30 min), while its impact upon all other metrics was rather moderate. Finally, as expected on theoretical grounds, reduced coupling had no influence upon AP features, but slowed down CV.
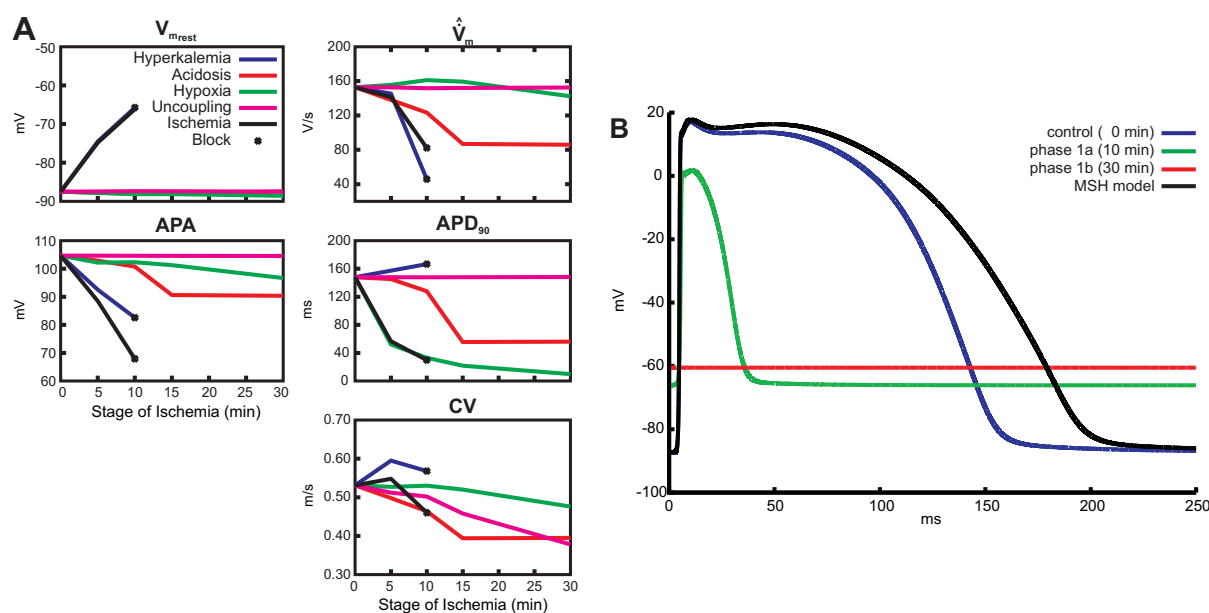
Figure 5.1: Effects of hyperkalemia, acidosis, hypoxia, cell uncoupling and ischemia (combination of all four components) during impulse propagation on (A) AP properties and CV as well as on (B) AP waveform. Resting potential ($V_{m_{rest}}$), maximum upstroke velocity ($\hat{V}_m$), amplitude of transmembrane AP (APA), APD at 90% of repolarization (APD$_{90}$) and conduction velocity (CV).

Fig. 5.1 B shows simulated APs obtained after combining all contributing factors to model overall ischemia. The AP shape as generated by the original MSH model is shown to serve as a reference. Note that even during normoxic intracellular ATP and ADP levels (6.8 mmol/L and 15 μmol/L, respectively), the augmentation of the MSH model with an $I_{K,ATP}$ channel added a non-zero outward K^+ current which shortened APD$_{90}$ to 80% of its nominal value. Changes in AP morphology as induced by the progression of ischemia are summarized in Fig. 5.1 A. $V_{m_{rest}}$ was elevated while $\hat{V}_m$, APA and APD$_{90}$ were monotonically reduced until block. The elevation of $V_{m_{rest}}$ was determined solely

by hyperkalemia (the blue trace related to hyperkalemia overlaps with the black trace related to ischemia). APA was reduced to a larger extent due to the combined effects of hyperkalemia, acidosis and hypoxia. Shortening of APD_{90} was mainly governed by the hypoxia-driven increase in $I_{K,ATP}$. Hyperkalemia led to conduction block after 10 min, no APs could be elicited at 15 min (not shown) and 30 min (phase 1b).

5.1.2 Effects of Ischemia-induced Heterogeneity on Propagation and AP Characteristics in a 3D Preparation
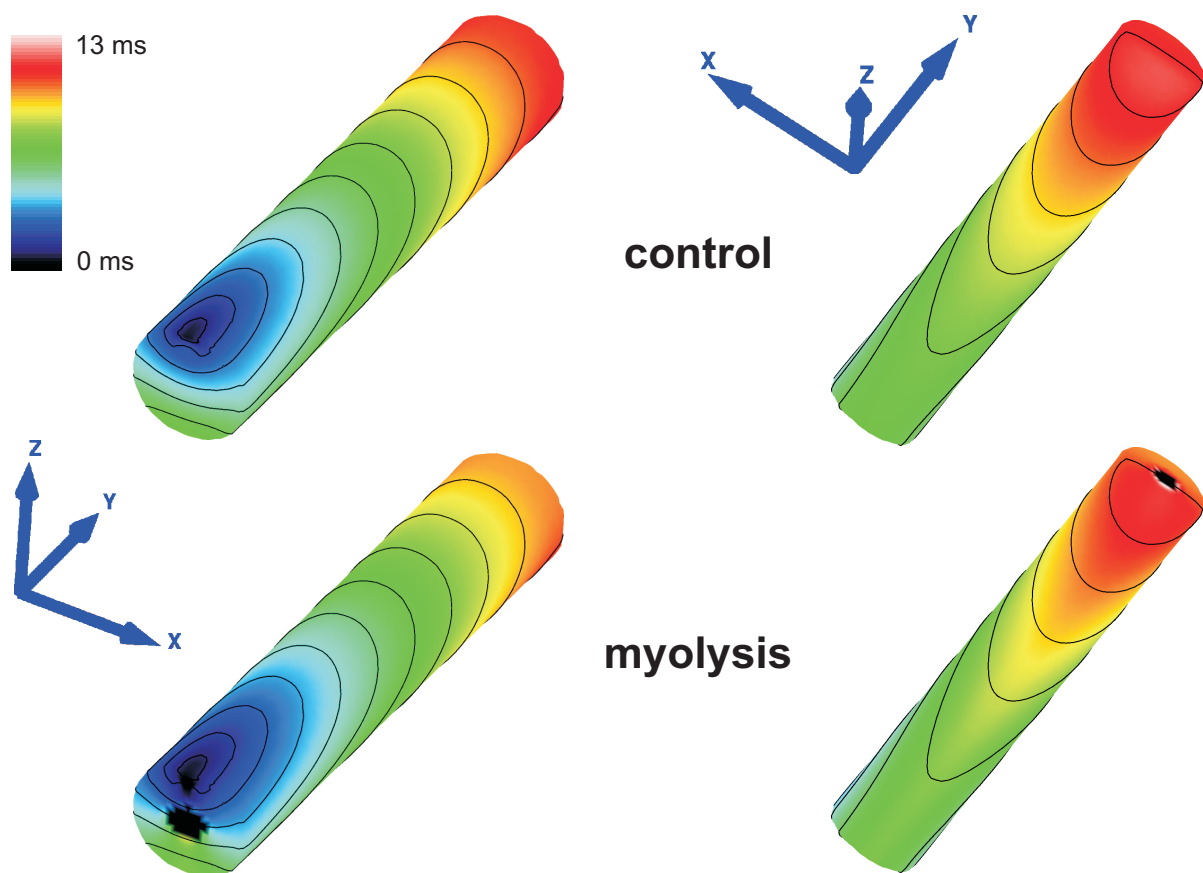
Figure 5.2: Activation sequences in the control and myolysis models (viewing upper and back sides of muscle). Activation started at the left top cusp (blue) and finished after 11.5 ms (control) and 12.9 ms (myolysis) at the right basal cusp (red).

A 3D model of a thin-walled cardiac muscle was used to study the effect of ischemia-induced radial heterogeneity upon activation sequence and AP characteristics. Fig. 5.2 presents the propagation pattern in control as well as in myolysis (worst case scenario) and Fig. 5.3 shows APs in both the CIZ and the NZ of the muscle. Unlike with the homogeneous 1D strand where functional gradients were absent, electrotonic interactions due to intrinsic differences in AP morphology between the CIZ and viable NZ act to modulate the intrinsic cellular dynamics. Comparing Figs. 5.3 A and 5.1 B demonstrates

that main qualitative differences were observed in case of phase 1B and myolysis. Unlike in the case of the 1D strand, V_m in the CIZ always departed from the resting potential, even in the case of myolysis, driven by electrotonic interactions between NZ and CIZ. Conduction within the CIZ was possible during phase 1B and failed only in the case of myolysis (> 30 min) where $\boldsymbol{\sigma_i}$ (Eq. 3.19, p. 35) in the whole core (CIZ and BZ) was set to 10% of the control model. CV in the NZ increased by 5.2% during phase 1a, but remained constant during more advanced stages of ischemia. Fig. 5.2 reveals that despite the fact that propagation fails in the CIZ during myolysis, the overall activation sequence at the surface is comparable to the control.
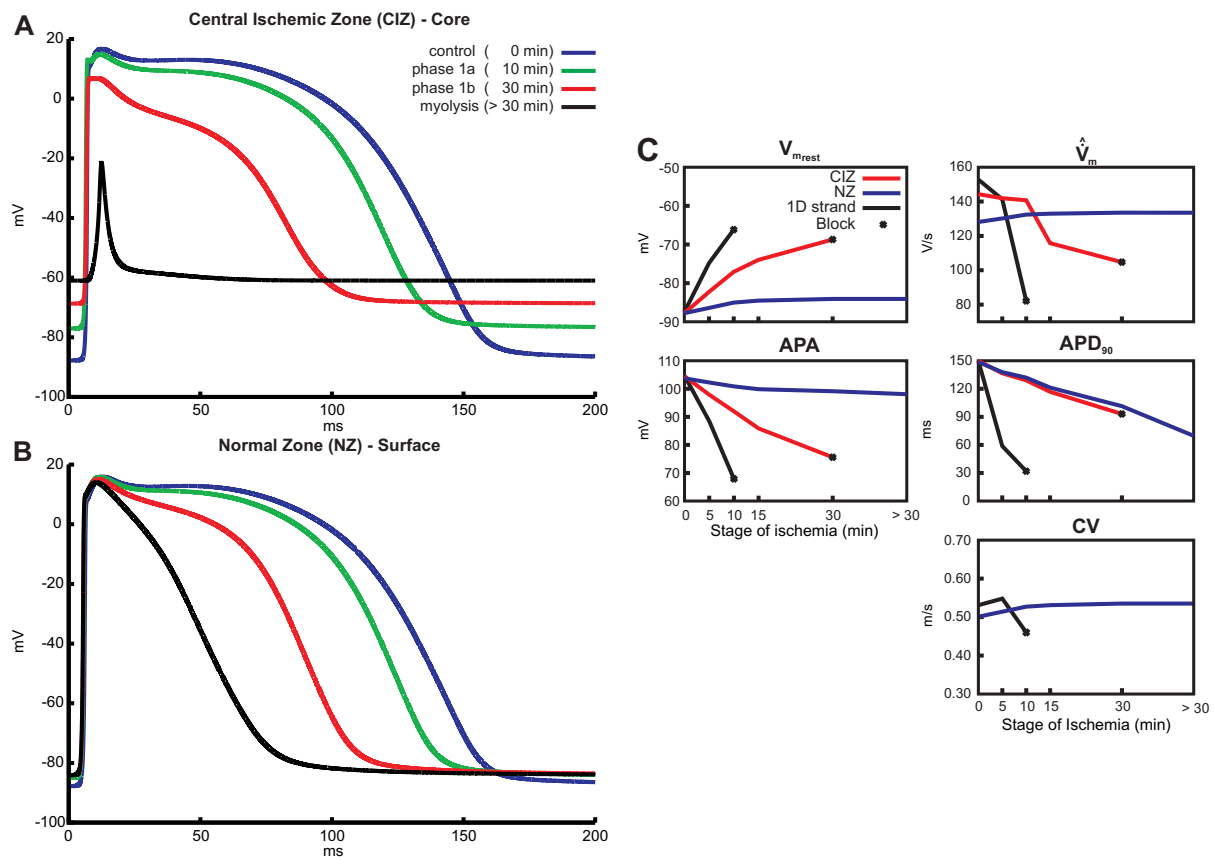
Figure 5.3: Results obtained with all 3D models. Representative APs (A) in the core (CIZ) and (B) in the surface layer (NZ) for varying states of progression of ischemia in the CIZ: control, ischemia phase 1a, phase 1b and myolysis. (C) Variation of AP properties in CIZ and NZ as a function of ischemia progression (see Tabs. 4.1-4.2, pp. 42-43). Results related to the 1D strand are shown for the purpose of comparison.

At the same time, the presence of a CIZ adjacent to the viable NZ had a very minor impact upon all AP characteristics, except APD_{90}. Changes in $V_{m_{rest}}$, APA and $\hat{V}_m$ were detectable, but remained small (<5.5%). The most prominent effect was a significant shortening of APD_{90} due to diffusive repolarization currents. APD_{90} shortened from 148.6 ms (control) to 131.9 ms, 88.8% (phase 1a), 101.4 ms, 68.2% (phase 1b) and

69.8 ms/47.0% (myolysis), respectively. That is, in the most extreme case of a myolytic core APD$_{90}$ in the viable NZ decreased to 47% of those values observed in a muscle where the entire cross section remains viable. All changes in AP characteristics over time in NZ and CIZ under electrotonic coupling are summarized in Fig. 5.3 C.

5.1.3 Effect of Ischemia on Extracellular Depolarization Signals Recorded at the Surface

Extracellular signals ϕ_e recorded at the observation site CP are shown in Fig. 5.4 A for different stages during the progression of ischemia. Note that the shape of the depolarization signals are very similar. As ischemia progresses, minor delays relative to the control case occur due to the minor conduction slowing in the NZ secondary to the drag effect of the CIZ. Further, minor differences are observed between 8 to 12 ms due to border effects which arise when the wavefront collides with the end of the specimen. Fig. 5.4 B reveals that all conduction parameters based on ϕ_e are marginally affected by the ischemic core. Comparing control with phase 1b and myolysis it is observed that $\phi_{e_{pp}}$ decreases by 3.6% and 9.4%, whereas the peak-to-peak interval T_{PP} is shortens by 8.2% and 12.3%, respectively. The maximum negative rate of rise $\hat{\dot{\phi}}_e$ showed a non-monotonic behavior, being more negative by 3.3% during phase 1b, but returning to the control value during myolysis, where the CIZ was almost fully decoupled.
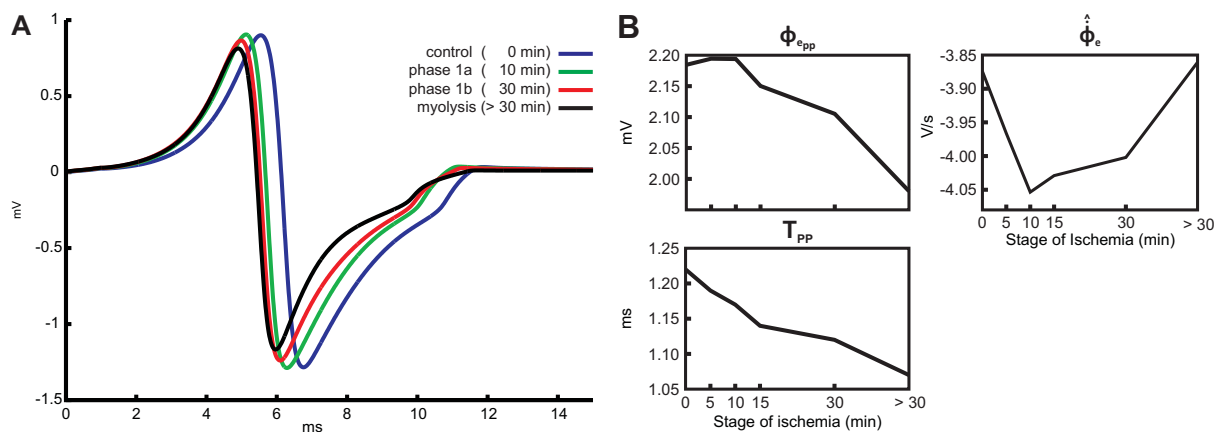
Figure 5.4: Signals recorded close to the surface of the preparation at observation the point CP (see Fig. 4.6 in p. 52). (A) Extracellular potentials recorded at different stages of ischemia: control, ischemia phase 1a, phase 1b and myolysis. (B) Variation of ϕ_e-derived metrics during ischemia progression. Amplitude of the signal ($\phi_{e_{pp}}$), negative peak of the time derivative $\hat{\dot{\phi}}_e$ and time difference between the negative and positive peaks T_{pp}.

5.1.4 Discussion

Since the 80s superfusion techniques have been used extensively as a method to supply oxygen and nutrients to thin-walled cardiac tissue samples such as pectinate and papillary muscles.[54,59,61,114] In recent years superfusion has gained relevance again in experimental studies that involve large tissue samples.[55,56,58] Such thin-walled samples, although virtually 1D (trabeculae, pectinate or papillary muscles) or 2D (atria), are effectively 3D structures which is why gradients in metabolic state build up over the cross section of a muscle, unless more elaborate perfusion techniques are applied.[113,115,116] Over time the core of the muscle becomes ischemic whereas superficial layers remain perfectly viable. It remains unclear as to which degree electrophysiological recordings from such preparations are affected. Computer simulations suggests themselves quite naturally as a modality for investigating these effects, since electrophysiological parameters in the depth of such samples cannot be observed at all, or with very limited spatio-temporal resolution, with experimental techniques alone. Previously, the impact of ischemia progression on impulse propagation in such thin-walled superfused preparations has been studied using 1D computer models,[135] however, effects of radial heterogeneity, as they arise in 3D, have not been considered yet. In this study a 3D computational model was developed to characterize effects of superfusion-induced radial heterogeneity upon AP morphology and impulse propagation, as well as to assess the relative contributions of superficial and core layers to extracellular depolarization signals measured in the volume conductor close to the tissue surface. Although the main focus of the study is on the impact upon depolarization signals and propagation, repolarization metrics such as changes in APD are reported as well, since these are of relevance when interpreting the results in the context of larger tissues samples when used for studying arrhythmogenesis or defibrillation.

Effects of Ischemia in a 1D Strand

The recent MSH model of a rabbit ventricular myocyte was used and augmented following previously reported approaches[99–101,103] to account for the three main effects of ischemia at the cellular level: hyperkalemia, acidosis and hypoxia.[99–101,103,104] 1D simulations were performed to ascertain that predictions are in line with previous studies: i) Ischemia-induced changes are qualitatively and quantitatively reproduced for all stages of ischemia progression (Fig. 5.1). ii) The biphasic relationship between CV and $[K^+]_e$, referred to as "supernormal conduction", shown in Fig. 5.1 A,[135] was observed. iii) As previously reported,[135] conduction block occurred at $[K^+]_e > 8.9$ mmol/l (10 min). iv) Augmentation with an ATP-sensitive K^+ channel shortened APD_{90} by 20% under normoxic conditions, in agreement with previous studies where decreases of 17%[101] and 12%[105] were reported. v) Under normoxic conditions AP characteristics matched up very well with other simulation studies[100,101,103,135] and fell within the range of experimental

data obtained from perfused rabbit papillary muscles.[110,113,115–117] vi) Progressive uncoupling and morphological changes in the interstitial matrix, as reflected by changes in extra- and intracellular conductivities in the model, did not influence any AP properties. The decrease in $\boldsymbol{\sigma_e}$ during the first 10 min led to a small decrease in CV and later after >15 min to disturbances of impulse conduction, consistent with experimental reports.[110]

Effects of Ischemia in a 3D Preparation

In 3D, the intrinsic cellular dynamics is modulated by electrotonic crosstalk between cells of different electrophysiological states. This caused APD to be noticeably shorter in the viable superficial NZ due to the presence of additional diffusive repolarization currents, as imposed by cells in the CIZ where APD is much shorter or tissue even remains unexcited. Conversely, APDs in the CIZ are longer and APs are elicited even in those cases where propagation block occurred in 1D. These electrotonic influences are governed by the transverse space constant, λ_t, which is at the order of $\approx 100\,\mu$m. That is, electrotonic crosstalk occurs over the entire cross section of the preparation, assuming a radius of influence of $5 \times \lambda_t$. Therefore, intrinsic differences between CIZ and viable NZ were smoothed out, resulting in ischemic effects which are qualitatively similar to 1D, but significantly less pronounced.

Major global physiological differences arose mainly at more progressive stages of ischemia. Unlike in 1D where conduction block occurred at the onset of phase 1b (15 min), propagation in 3D did not even fail in the late phase 1b (30 min). Conduction block occurred only during myolysis (> 30 min) where $\boldsymbol{\sigma_i}$ in the core was reduced to 10% of the control values. Further, as ischemia progressed, the overall activation sequence started to alter. These changes were moderate until phase 1b, affecting mainly the shape of the depolarization wavefront in the CIZ. In the extreme scenario of myolysis propagation failed in the CIZ, causing the activation wavefront to propagate around the myolytic core which led to collisions at the bottom of the muscle (see Fig. 5.2). The activation sequence at the top of the muscle remained virtually unchanged though, only minor difference were observed. At the surface CV is slightly faster in myolysis, as shown in Fig. 5.2 and in Fig. 5.3 C in the CV panel, because the myolitic core is decoupled from the the healthy tissue ($\boldsymbol{\sigma_i}$ was reduced to 10%). Thus, unlike the control condition, the core does not represent a load for the activated cells at the surface. In terms of total activation time, in myolysis this took slightly longer than in the control case with 12.9 ms versus 11.5 ms, respectively. This is caused by cells within the BZ, which are still able to conduct a very impaired AP due to electrotonic interactions between NZ and CIZ. That is, the latest activating cells are located in the distal end of the preparation in the BZ (not shown).

Extracellular Depolarization Signals

Despite major electrophysiological changes throughout the muscle, recordings of extracellular depolarization signals close to the surface remained surprisingly unaffected. For instance, during phase 1b extracellular potentials ϕ_e at CP had their T_{PP} shortened by 8.2% and changes in $\phi_{e_{pp}}$ as well as in $\hat{\dot{\phi}}_e$ were even less significant ($< 4\%$), as shown in Fig. 5.4 B. In the extreme case of myolysis where conduction was blocked in the CIZ, the effect on extracellular depolarization signals was very minor, with a 9.4% decrease in $\phi_{e_{pp}}$ and a shortening of T_{PP} by 12.3% compared to control. Minor changes in arrival times arose due to changes in CV.

These fairly moderate changes can be attributed to the fact that sources in the superficial NZ are closer to the recording site and thus carry a more significant weight in determining the extracellular potential field. Contributions of sources to ϕ_e are weighted by a $1/r$ relationship where r is the distance between recording site and source point.[136] Hence, for the given setup sources in the NZ carry roughly ten times the weight of sources located in the more distant CIZ. The temporal derivative $\dot{\phi}_e$ was even less affected since weighting of sources is governed by the function $1/r^2$, giving sources in the NZ ~ 87 times the weight of sources in the CIZ. Further, the sources carrying most of the weight are located in the NZ which is least affected. In the NZ $V_{m_{rest}}$, $\hat{\dot{V}}_m$ and APA were barely affected (see Fig. 5.3), only APD_{90} was significantly altered there, with reductions of 32% and 53% during phase 1b and myolysis, respectively. However, changes in APD are not reflected at all in extracellularly recorded depolarization signals.

Limitations of the Model

A 3D computational model of a superfused thin-walled cardiac muscle was developed, using a cylindrical geometry with a diameter of 1.0 mm to match experimental set-ups.[115–117] This choice of diameter is a key factor which strongly influences the electrophysiology of the whole preparation, in particular, the ratio between viable and ischemic tissue volume. Nonetheless, in this study the diameter was not a model parameter and kept fixed throughout the study. A further important factor is the width of viable NZ and BZ which depends on numerous factors such as the rate of cellular consumption, the diameter of the muscle or the pressure in the external solution. Even when the superfusate is well oxygenated, the CIZ may be still deprived of an adequate oxygen supply if oxygen use is high, diffusion distances are excessively large, or both.[61] Experiments with rabbit myocardium, where perfusion and superfusion were combined, demonstrated that cells within 130 μm remain viable, whereas cells up to 650 μm are relatively little affected by ischemia phase 1a.[121] In the same study, transmural extracellular gradients of K^+, pH and myocardial energy metabolism were also shown to build up, depressing APs markedly in layers deeper than 600 μm in phase 1b. Such transmural inhomogeneities in the ischemic heart have

been further investigated in other experimental work as well.[119,120] Early modeling and experimental studies suggested that the critical diameter is around $0.6\text{-}0.8\,$mm at 37°, where, if exceeded, an anoxic core is formed.[60,61,137] In the model the widths of the NZ and BZ were kept fixed as $250\,\mu$m and $125\,\mu$m, respectively, which is, consistent with experimental reports,[121,123] in the range of 130 - 300 μm. Moreover, the width of NZ and BZ is also known to be different for the three main components of ischemia.[122] However, a simpler approach was opted where the same width of BZ for hyperkalemia, acidosis and hypoxia was used and all parameters in Tabs. 4.1 and 4.2, pp. 42-43 were linearly interpolated between NZ and CIZ.[104,124]

A further limitation is the short length and simplified geometry of the model. While this setup approximates traditional experimental setups fairly well where isolated papillary muscles or trabeculae are used, this is not the case with more recent studies[55,56,58] where electrical activity is globally mapped over larger preparations such as the atria. Nonetheless, the findings reported in this study for a small cable-like sample can be extrapolated to larger superfused preparations (e.g. the atria), considering that the thickness of the individual muscles do not exceed the dimensions considered here. The results suggest that activation sequences and extracellular potentials during the depolarization phase will remain largely unaffected in larger preparations, however, particular caution is advised when analyzing data which also involve the repolarization phase, as it is the case when studying the formation of arrhythmias.

Although these choices may affect the findings presented in this study quantitatively, qualitatively they are robust and do not depend on these choices. With regard to measurements of extracellular depolarization signals this view is supported by the observation that even in the worst case scenario of a myolytic core the influence upon ϕ_e was virtually negligible.

5.2 Image-based Tissue Models

5.2.1 Macroscopic Model of the Region of Interest (ROI)

Fig. 5.5 A presents the fiber orientations computed by solving a Laplace's equation. Field lines terminated between the electrodes placed on the Crista Terminalis (sources) as well as on the Vestibule (sinks). Note that the resulting potential gradient points from one electrode to the other, and most importantly, navigate around local discontinuities due to the macrostructure of the tissue. The fiber orientations were combined with the FE mesh in order to establish a macroscopic model of the ROI. In order to investigate activation sequences in this tissue model, a depolarization wavefront was initiated by applying a stimulus current at the CT as shown in Fig. 5.5 B. The isochrones were computed based on the transmembrane potentials V_m. All myocytes within the region of interest (ROI) are activated after about 20 ms.
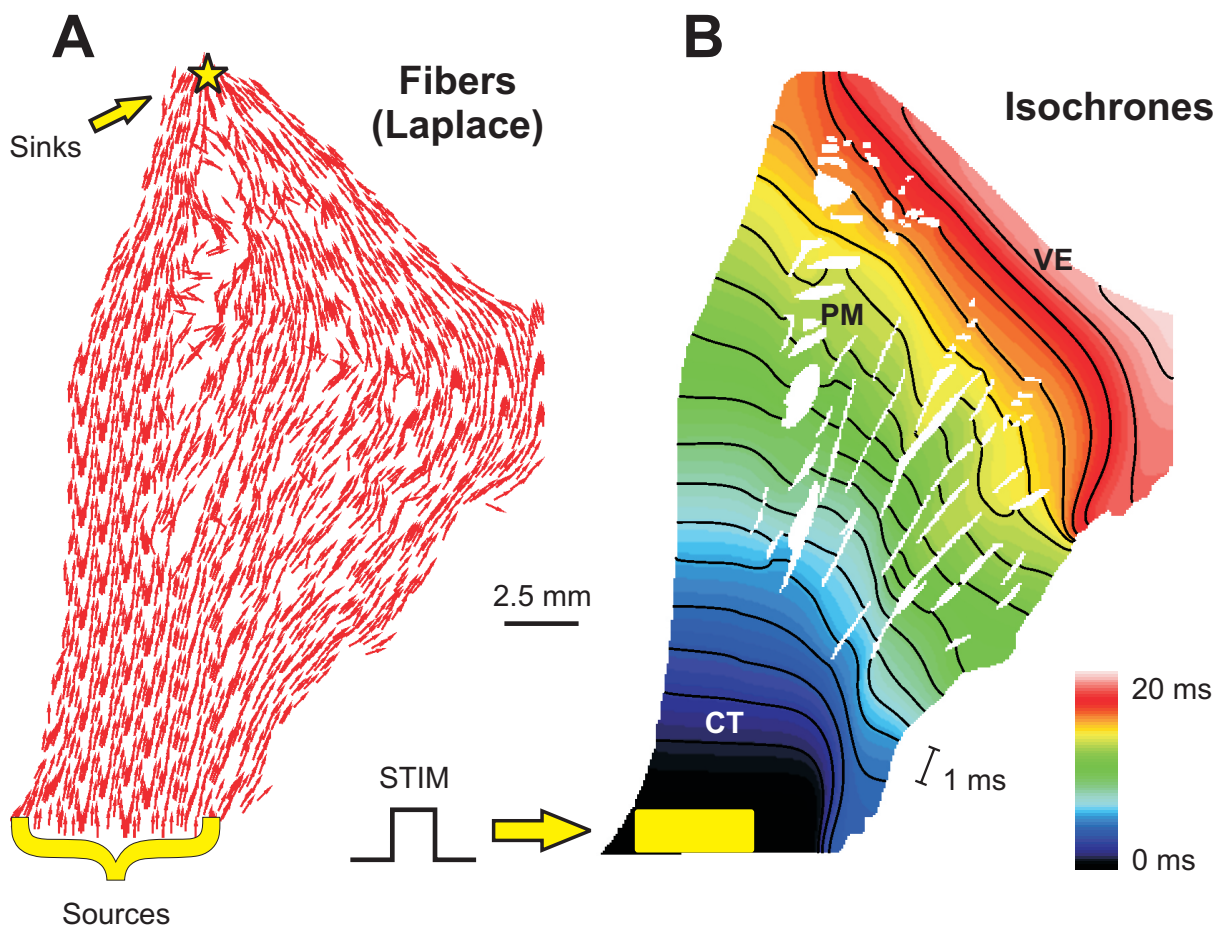
Figure 5.5: (A) Macroscopic fiber orientations obtained by solving a Laplace problem. Locations of sources and sinks are indicated. (B) Activation sequences. Activation started at the Crista Terminalis (CT) and finished at about 20 ms.

Conduction velocities (macro) as well as local conduction velocities (micro) along

Pectinate muscles were calculated and compared to values obtained in experiments. Pectinates were chosen rather than the Crista and the Vestibule because they have a simpler geometry and alignment of fibers (mainly longitudinal conduction). As can be seen in Fig. 5.6, CV from simulations (CV_{Sim}) is about $0.8\,m/s$ in PM1 and PM3, and about $0.7\,m/s$ in PM2. Simulated local conduction velocities (LCV_{Sim}), on the other hand, vary along Pectinates from $0.6\,m/s$ up to $1\,m/s$ (PM3). Mean CV (thick lines) and standard deviation (dashed lines) obtained in experiments (CV_{Exp}) are also shown for comparison.
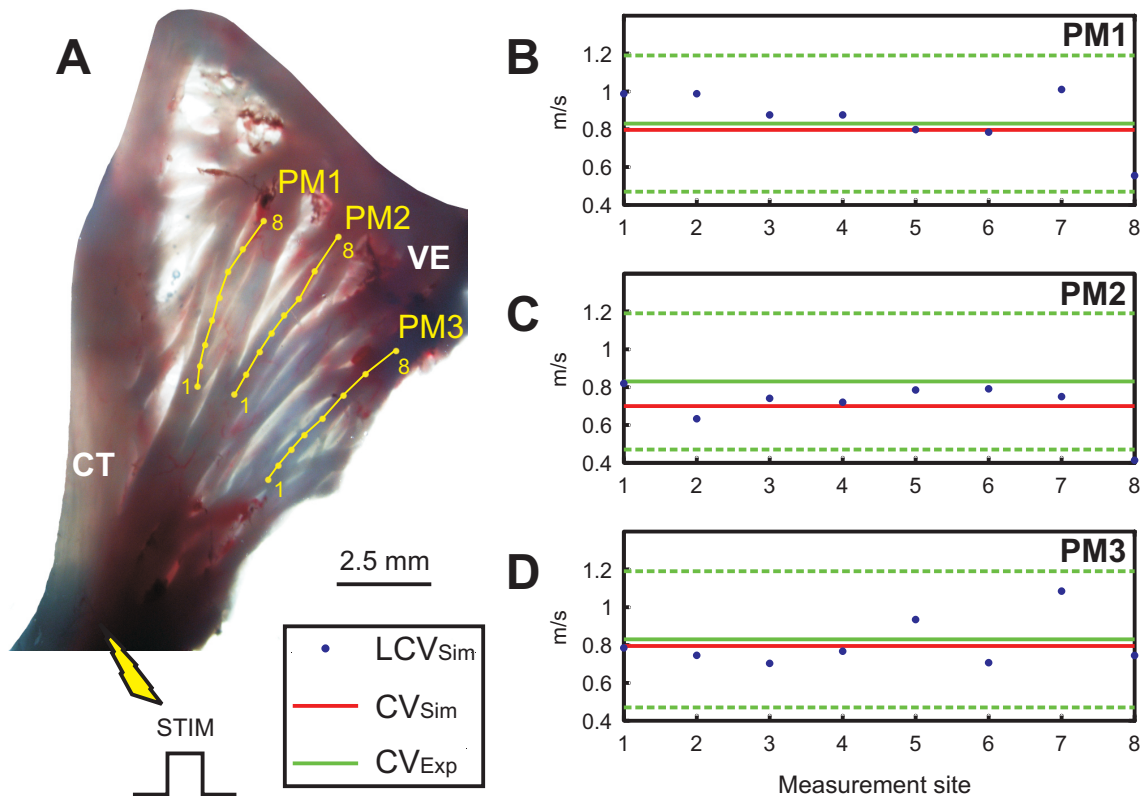
Figure 5.6: (A) Image used to build the macro model of the ROI depicting the pathways taken to compute conduction velocity along three PMs. (B)-(D) Macro conduction velocity (CV_{Sim}) and local conduction velocity (LCV_{Sim}) computed along the pathways in (A). In total, 8 measurement sites were considered to form the pathways and each position represents the center of a CNF sensor. CV_{Sim} was estimated by linear regression whereas LCV_{Sim} was obtained as described in Sect. 4.5.4, p. 55. Mean CV (CV_{Exp}) and standard deviation (dashed lines) obtained in experiments are also shown. Image and experimental data were kindly provided by Dr. Ernst Hofer[*].

In addition to CV and LCV, fractionation index (FI) was also computed in order to obtain more information about underlying electrical conduction. Uniform atrial electrograms (UAEs), i.e., FI = 1 correspond to about 96% of the extracellular signals ϕ_e. The

---

[*]Institute of Biophysics, Medical University of Graz, Austria.

remaining signals were complex fractionated atrial electrograms (CFAEs) with FI = 2. Fractionated electrograms in the CT were due to stimulus artifacts, whereas complex signals in the PMs and in the VE arose due to delays in the wavefront in adjacent structures. More specifically in regions where muscle bundles are merging or branching. An example of such type of fractionated electrogram is shown in Fig. 5.7. ϕ_e was computed at the observation point indicated by an yellow triangle in Fig. 5.7 C-D. In this case, a PM branches into a thicker (left hand side of the observation point) and thinner (observation point) bundles. Note that delayed events can be readily seen as two peaks in the temporal derivative $\dot{\phi}_e$ (Fig. 5.7 B). The arrival of the wavefront at the local activation times (LATs) corresponding to the two peaks are showed in Fig. 5.7 C and Fig. 5.7 D, respectively. The first peak is generated by depolarization front traveling on the thicker muscle bundle, whereas the second peak is due to the activation of myocytes at the point of observation. The amplitude of the first peak is larger because the adjacent muscle is thicker, i.e., there are more myocytes (sources) activated at that time instant (LAT1).
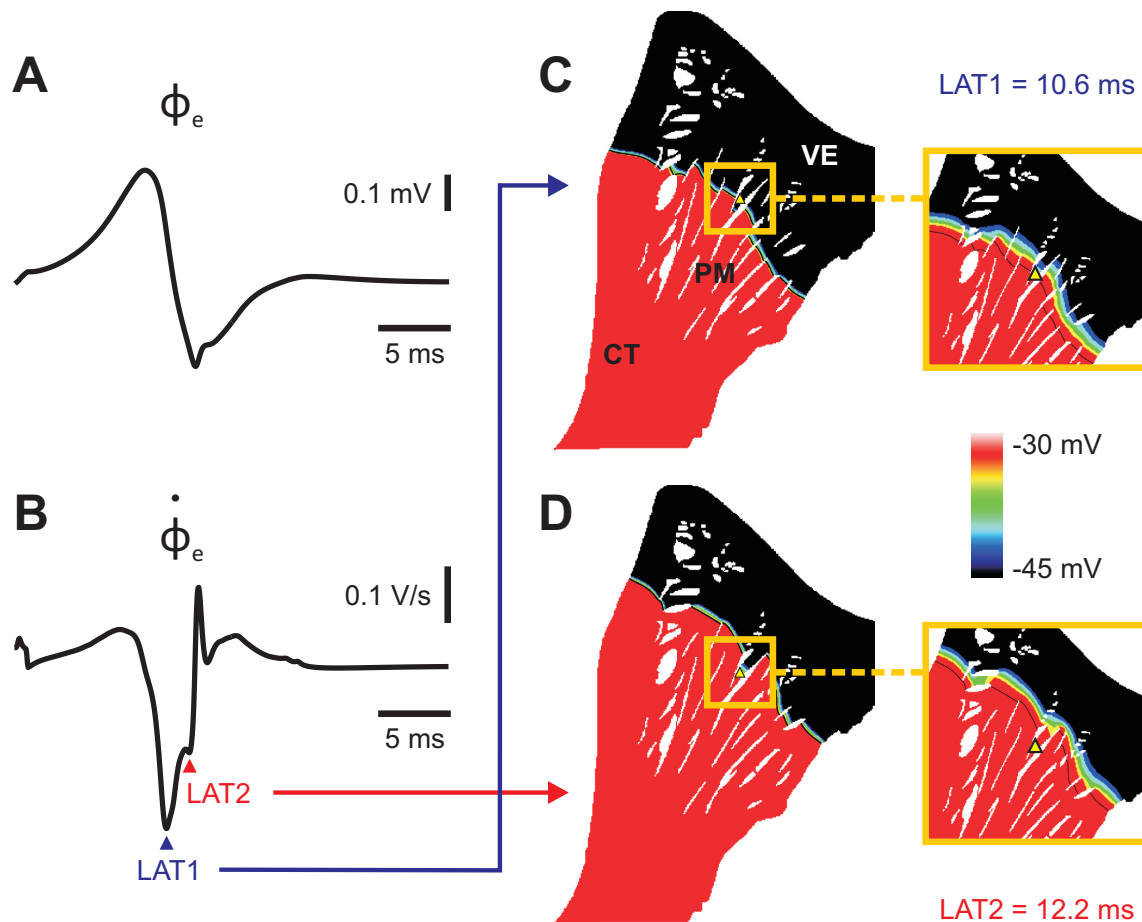
Figure 5.7: (A) Complex fractionated atrial electrogram (CFAE) ϕ_e and (B) its temporal derivative $\dot{\phi}_e$ generated by a wavefront passing at the observation point depicted by an yellow triangle in (C) and (D). (C) Depolarization wavefront. Color coding refers to depolarized (red) and quiescent (black) cells, 10.6 ms and (D) 12.2 ms after the stimulus.

5.2.2 Microscopic Models of the ROI

Figs. 5.8-5.9 show the two histographs (from two different hearts) as well as the resulted segmented images taken to construct microscopic models of the ROI. Although both tissue slices are from the rabbit isthmus, they account for two different parts of the Crista Terminalis. The histological image in Fig. 5.8 A is a representative cut of the upper part of the CT, closer to the Sinoatrial Node and containing more uncoupling structures. In the lower part of the CT, on the other hand, well coupled tissue is predominant (see Fig. 5.9 A). The presence of fibrosis and interstitial clefts in both histographs is reflected in the respective segmented images by forming "islands" of disconnected myocytes.
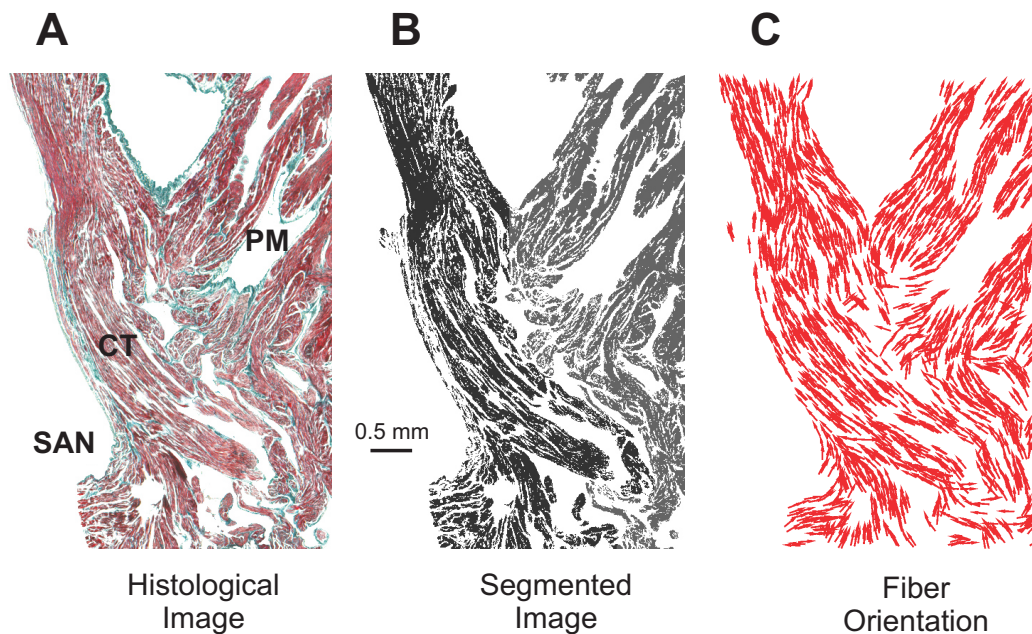
Figure 5.8: (A) Micrograph of the region of interest (ROI) showing the upper part of the Crista Terminalis (CT) and Pectinate Muscles (PMs). The locations of the Inferior Vena Cava (IVC) and the Septum Tricuspidal Valve (STV) are also depicted. (B) Segmented image used to construct a microscopic model. CT in black and PMs in gray. (C) Computed fiber orientation. Histograph kindly provided by Dr. Ernst Hofer[†] and segmented with the help of Dr. Helmut Ahammer[†].

Cardiac fiber orientation has been measured histologically at the endocardial surface of the ROI, and incorporated to the microscopic models developed in this thesis. The local fiber orientation was extracted by processing a grayscale version of the raw histological image. Resulted fiber alignment along the bundles of the Crista Terminalis, Pectinate muscles and Vestibule are shown in Fig. 5.8 C and Fig. 5.9 C. Note that in both histographs fibers are aligned following the macro anatomy of the ROI. Complex fiber orientations are found at the junction of the CT and a PM. A noticeable bending in the cardiac fibers from the lower part of the CT to the PMs can be seen in Fig. 5.9 C.

[†]Institute of Biophysics, Medical University of Graz, Austria.
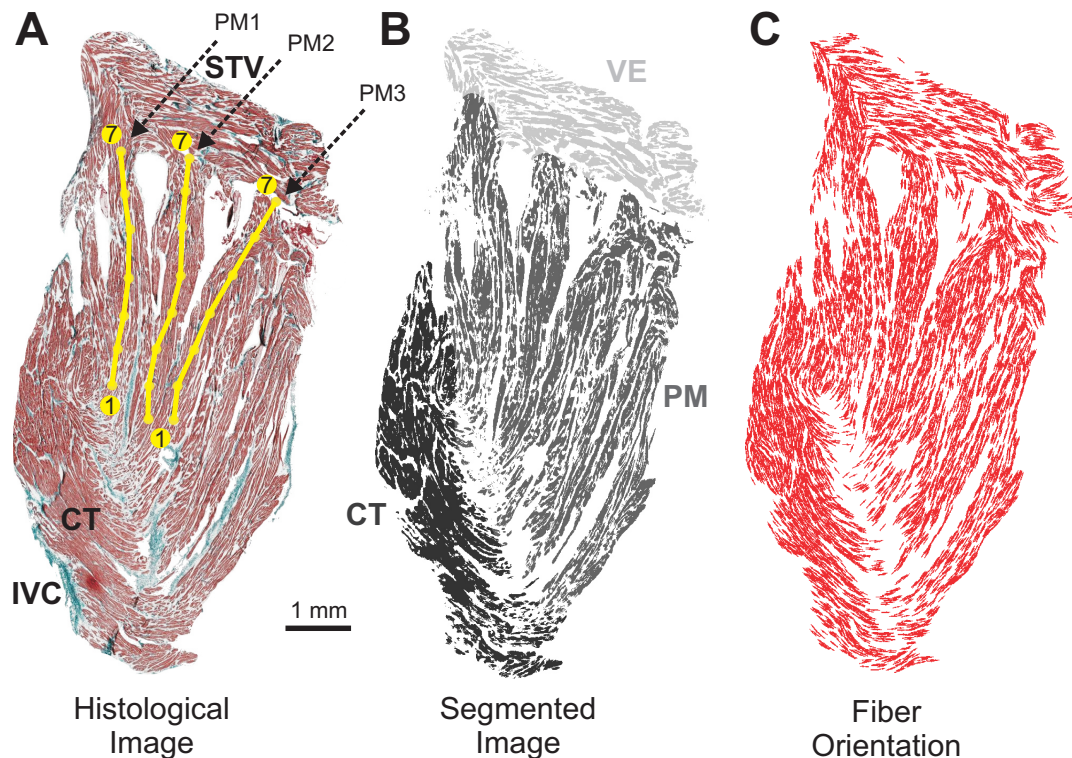
Figure 5.9: (A) Micrograph of the ROI showing the lower part of the Crista Terminalis (CT), Pectinate Muscles (PMs) and Vestibule (VE). Locations of the Inferior Vena Cava (IVC) and the Septum Tricuspidal Valve (STV) are also depicted. Pathways taken to compute conduction velocity along three PMs are illustrated by yellow lines. (B) Segmented image taken to construct a second microscopic model of the ROI. CT in black, PMs in dark gray and VE in light gray. (C) Computed fiber orientation. Histological image kindly provided by Dr. Damián Sánchez-Quintana[‡] and segmented with the help of Dr. Helmut Ahammer[§].

Electrical propagation in the model generated based on Fig. 5.9 B was initiated by a transmembrane current stimulus at the CT. The whole CT was stimulated rather than a specific point in order to ensure antegrade propagation (from the CT to the VE). Fig. 5.10 shows isochrones as well as the simulated depolarization wavefront. Color coding refers to depolarized (red) and quiescent (black) cells at 2 ms after the initial stimulus. A complex propagation pattern due to the presence of clefts and the heterogeneous fiber direction structure followed the stimulus. Such complexities resulted in remarkable differences between macro (CV) and local conduction velocities (LCV) as shown in Fig. 5.11. CV and LCV were computed along the three PMs following the pathways depicted in Fig. 5.9 A. CV was 0.67, 0.75 and 0.72 m/s in PM1, PM2 and PM3 respectively. LCV on the other hand, varied up to 6 m/s (Fig. 5.11, measurement site 2 in PM1).
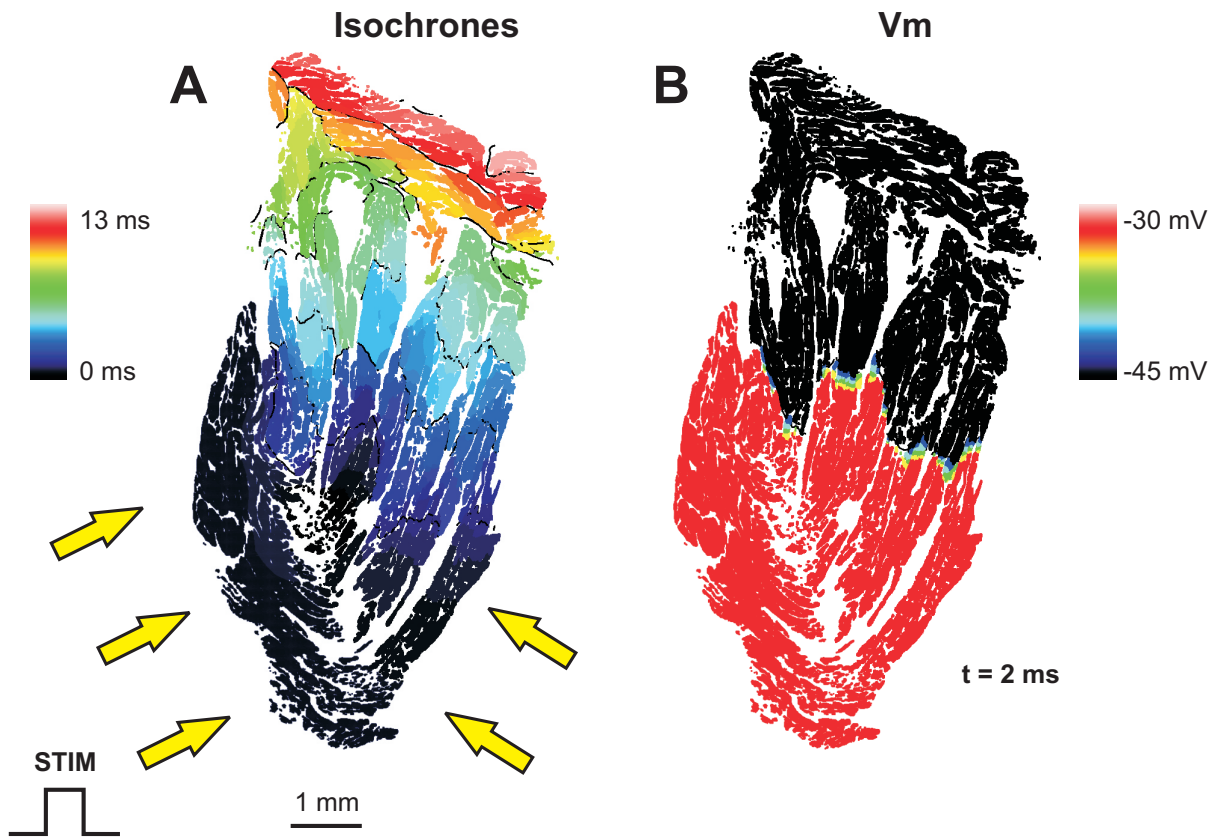
Figure 5.10: (A) Activation sequences (started at the CT). (B) Depolarization wavefront: depolarized (red) and quiescent (black) cells, 2 ms after the stimulus.
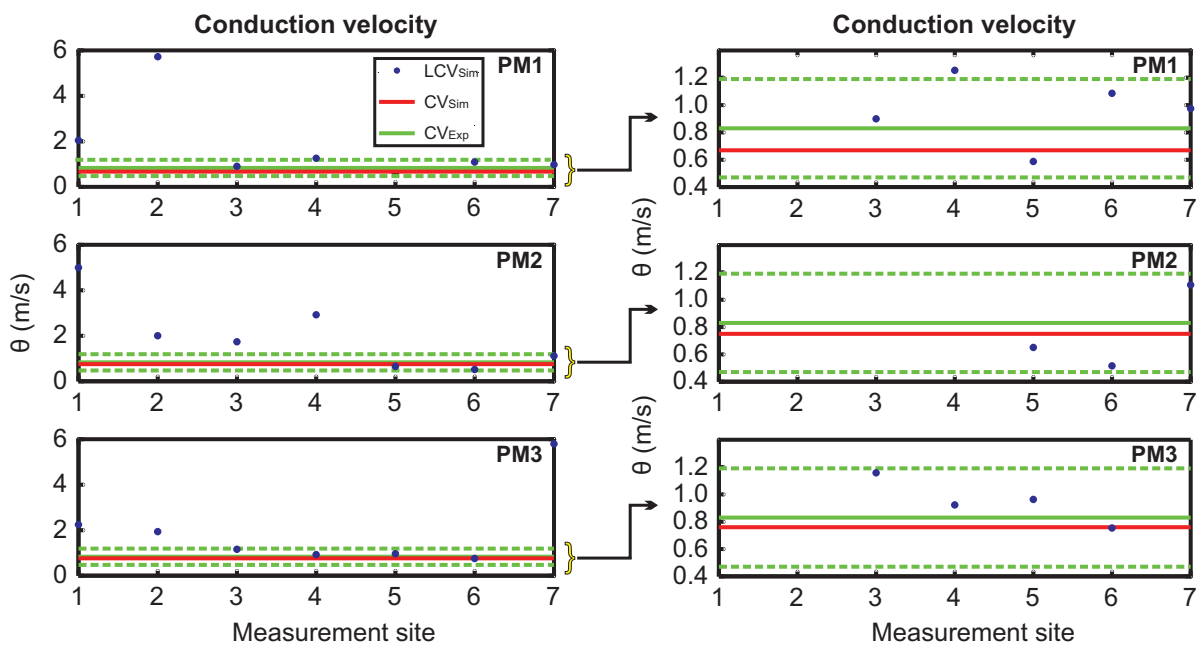
Figure 5.11: Macro conduction velocity (CV_{Sim}) and local conduction velocity (LCV_{Sim}) computed along the pathways in Fig. 5.9 A. In total, 7 measurement sites were considered and each position represents the center of a CNF sensor. Experimental data kindly provided by Dr. Ernst Hofer[¶].

Complexity of electrical propagation in the PMs was quantitatively assessed by computing FI of electrograms. Simulated as well as experimental results are presented in Fig. 5.12. Note that UAEs dominate followed by CFAEs with FI = 2.
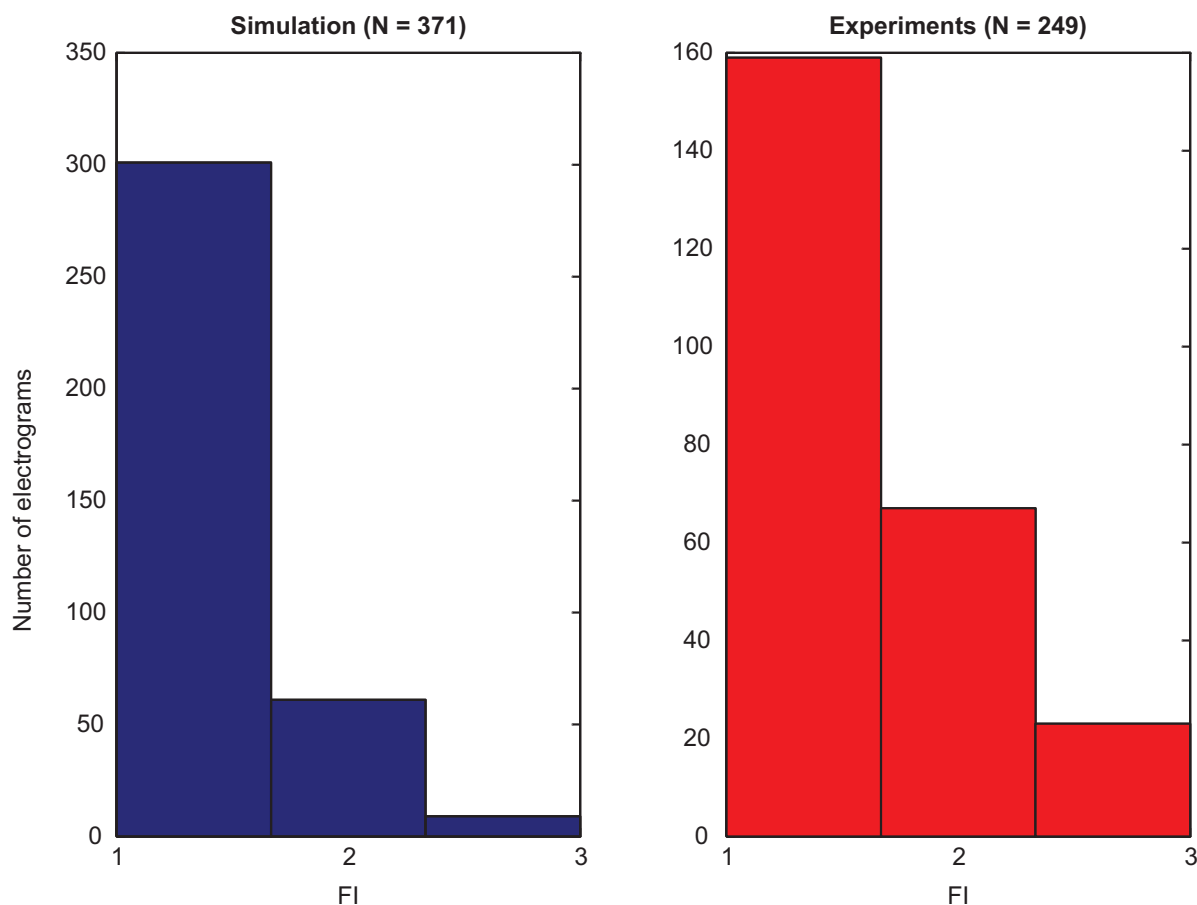
Figure 5.12: Distribution of Fractionation Indexes (FI) in Pectinate muscles obtained from simulated electrograms (N = 371 measurement sites) and experimental measured signals (N = 249). Experimental data kindly provided by Dr. Ernst Hofer[¶] and signal analysis performed with the help of Thomas Wiener[¶].

The 2D model of the ROI reveals the complexity of activation patterns caused by the microstructure, but electrical propagation would fail in the absence of a subsequent tissue layer resembling the 3D nature of the ROI. The inclusion of such shunting layer allows electrical propagation into regions that were disconnected by the 2D model. The genesis of fractionated electrograms and its relation with the underlying shunting layer was also investigated. To do so, additional simulations were performed where a transmembrane current was applied in a smaller area at the CT in order to reduce stimulus artifacts. The shunting layer should connect neighboring bundles, but at the same time undesired shortcuts should be avoided. Thus, the conductivity in the shunting layer was initially set to be the same as in the histological layer. Then, σ_m (Eq. 3.34, p. 37) was successively

[¶]Institute of Biophysics, Medical University of Graz, Austria.

reduced until a value 100x smaller. The results are summarized in Fig. 5.13. It can be seen that different from experiments, simulated UAEs appear more frequently. Simulations reveal that the lower the conductivity in the shunting layer, the larger the number of fractionated electrograms. Note that the number of detectable signals N in the Crista decreases from 153 to 149 when setting the shunting conductivity to $\sigma_m/100$. This is because no electrograms could be detected at some points due to a conduction block in the CT. Thus, all simulations with the micro models hereafter are performed considering the shunting conductivity to be $\sigma_m/20$. Note also that regardless the degree of coupling in the shunting layer, the distribution of FI obtained in all simulations differ completely from the experimental data included in Fig. 5.13.
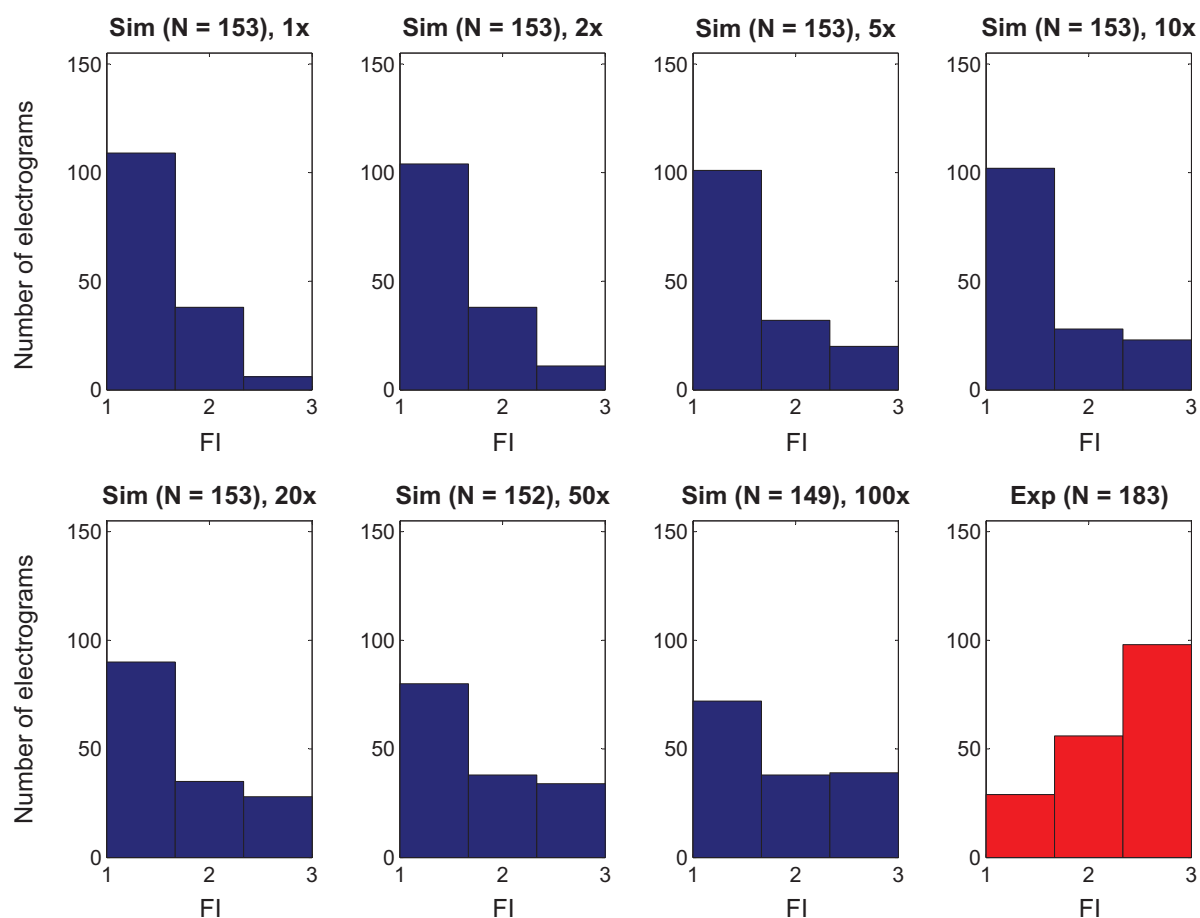
Figure 5.13: Distribution of Fractionation Indexes (FI) in Crista Terminalis (CT) obtained from simulations (N = 153 measurement sites) as well as from experiments (N = 183). Conductivities in the shunting layer were lowered from the control value σ_m to $\sigma_m/100$. Experimental data kindly provided by Dr. Ernst Hofer[¶] and signal analysis performed with the help of Thomas Wiener[¶].

5.2.3 Discussion

Macroscopic Model

The right atrial isthmus is seen as critical substrate for the genesis of intermittent block of conduction at junctions between the CT and PMs,[20] which may play a role in the initiation and maintenance of isthmus-dependent arrhythmias.[47] Computer models have been recently employed to study the atrial electrical activation at the macroscopic scale.[4,72,73] These models have provided important insights into conduction inhomogeneities and the creation of re-entry circuits. However, validation of the results through direct comparison to experimental data was not available. Instead, the minimal validation was done by adjusting the monodomain conductivity tensor in order to obtain "realistic" conduction velocities along the main axes of the cardiac fibers. However, extensive preliminary data obtained by spatio-temporally high resolution recordings in the ROI suggest that conduction patterns observed at the microscopic size scale are strikingly different from those expected from a macroscopic scale. In this work, a 2D model was developed incorporating a detailed representation of isthmus macrostructure and electrophysiologic heterogeneities. The results obtained from the simulation were compared to experimental data (kindly provided by Dr. Ernst Hofer[*]) not only in terms of velocity along the muscle bundles, but also in terms of micro conduction velocities. Furthermore, the morphology of electrograms computed at the endocardial surface was also considered since these signals have been used to guide catheter-based AF ablation procedures.[17,18]

The cardiac fiber orientation accounts for the anisotropic tissue conductivity and defines the conductivity tensor of the monodomain model. Rule-based methods, like the one employed here, play important roles in assigning fiber vectors within computational tissue models, where experimental data (e.g. DT-MRI) are not available.[95,96] The Laplace method used in this work was able to represent the fiber architecture in the isthmus at a macroscopic scale (gross anatomy). Conduction velocities along the axes of the Pectinate muscles were in good agreement with mean experimental data (0.83 ± 0.36 m/s in Fig. 5.6). Computed LCVs also fall within the range of recorded values. However, unlike the distribution of experimentally recorded extracellular potentials, where CFAEs were found to be about 36% of the measured signals,[126] simulated UAEs dominated (96% of the signals). Electrogram fractionation were due to either the proximity to the stimulus site or to delays in the wavefront in adjacent structures as shown in Fig. 5.7, p. 74. Functional heterogeneities, i.e., differences in ionic currents and AP morphology, had no influence on the fractionation of electrograms.

---

[*]Institute of Biophysics, Medical University of Graz, Austria.

Microscopic Model

Due to the limited effectiveness and associated risks of traditional pharmacological approaches,[138] minimal invasive procedures guided by endocardially recorded electrograms have been of great value in the treatment AFL and AF.[18] Complex fractionated atrial electrograms consisting of two or more discrete deflections may point to areas where conduction is impaired due to the formation of connective tissue and fiber disarray.[6, 139] As discussed previously, macroscopic models failed to reproduce CFAEs during normal pacing rhythm since they do not account for details at the microscopic level. CFAEs and their relation to the cardiac microstructure have been previously investigated via computational modeling.[24, 136, 140] To date, most studies have considered only the case where collagenous septa is aligned with the cardiac fibers. Jacquemet and Henriquez[24] demonstrated that CFAEs appeared in regions of severe degree of fibrotic tissue. However, simulations have also shown that not only amount of fibrosis, but also its texture may play a role in conduction slowing and arrhythmias.[7] This study presents two-dimensional tissue simulations of electrical excitation in the right atrial isthmus of the rabbit heart. The models incorporate detailed anatomical structures, fiber orientations, and electrical heterogeneities of distinctive regions of the CT, PMs and the VE. Despite the fact that they do not account for effects of subsequent layers of tissue in 3D, the models developed here distinguish themselves from other simplified[141, 142] and detailed atrial models[4, 72, 73] in the following aspects: 1) finer spatial resolution ($\sim 10\,\mu$m) and, as a result, more precise anatomical structures at the macro- and microscopic levels; 2) incorporation of fiber orientation obtained from individual 2D image slices using a gradient-intensity method; and 3) inclusion of newer atrial cellular models accounting for electrical heterogeneity in the isthmus.

The computed spread of activity in the microscopic tissue (Fig. 5.11) model (pectinate muscles) was in line with the experimental measurements of $0.83 \pm 0.36\,\text{m/s}$ as well as with values of 0.5-$0.8\,\text{m/s}$ found in the literature.[126, 143, 144] Local conduction velocities, on the other hand, were shown to vary up to $6\,\text{m/s}$ (see results from PM1 in Fig. 5.11). These high values result from complex wave curvature and direction of propagation at this observation point.

The correlation between the complex extracellular recordings and the activation of electrophysiologically identifiable structures has been topic of research since the 70's.[144] The results obtained with the histologically detailed model showed that CFAEs are associated with the presence of uncoupling structures (microfibrosis as well as interstitial clefts). Distribution of FI in pectinate muscles (Fig. 5.12 in p. 78) reveals that propagation is mainly uniform, with dominance of UAEs, despite the presence of uncoupling structures. This finding is supported by analysis of extracellularly measured potentials also shown in Fig. 5.12 (right column). However, the distribution of signals computed in

the CT, see Fig. 5.13, completely differed from experimental data. There are two reasons that could explain the discrepancies between simulations and experiments. First, the experimental data in Fig. 5.13 was obtained from extracellular signals measured in both lower and upper part of the Crista Terminalis. The lower part of the CT is mainly characterized by well coupled cardiac tissue as can be seen in Fig. 5.9, whereas the upper part of the CT, closer to the SAN, contains more uncoupling structures. Since the simulations were performed using the microscopic model built based on a micrograph containing only the lower part of the CT (Fig. 5.9), it is expected that uniform electrograms would appear more frequently due to well coupled nature of the tissue. Second, all simulations were carried out with a stimulus being applied at a fixed position in the CT. However, this is not the case in experiments since the SAN is distributed over a wide area along the CT. Thus, the SAN pacing activity does not correspond to a discrete pacing site. Therefore, the dependence of electrogram morphology on the direction of wavefronts arising from different parts of CT should be taken into account. In Sect. 5.3, directional dependence of FI on the wavefront is investigated.

Limitations

Due to the 3D anatomy of the isthmus, 2D models are not able to capture the full extent of connectivity in the CT/PM network. Nevertheless, such models have been shown to reproduce patterns of activation in the CT and the PM network with fairly good accuracy when compared to full 3D models.[73] The 2D macroscopic model developed here represents the anatomy of the ROI with considerable precision while keeping the computational overhead tractable. Once atrial cell models able to reproduce rapid heart rates relevant tachycardias are made available, the model presented here could be a potentially powerful tool for studying functional and structural isthmus-dependent arrhythmias.

5.3 Electro-Anatomical Characterization of Fibrosis

5.3.1 Multisite Pacing

The microscopic model developed based on Fig. 5.8 B, p. 75, was used to study the dependence of fractionated electrograms on the direction of the electrical wavefront. To do so, four simulations were carried out after applying a stimulus current at different locations as shown in Fig. 5.14.
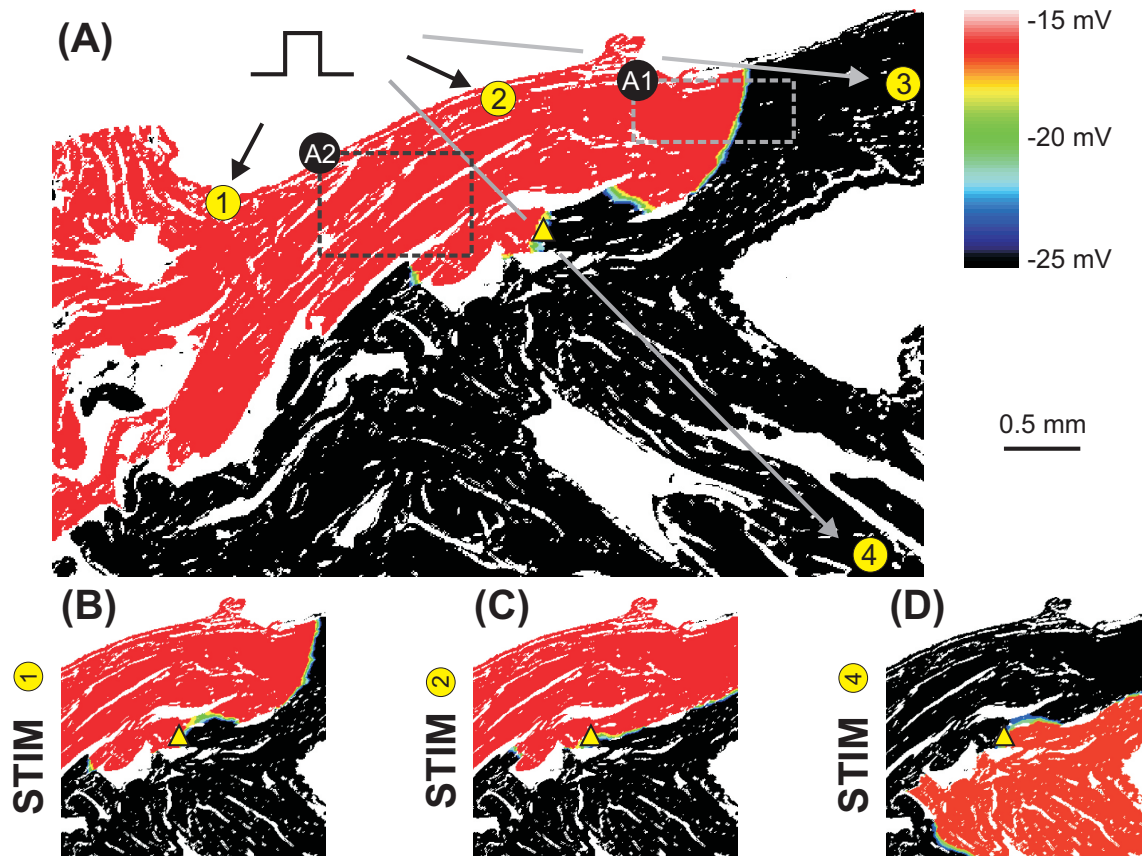
Figure 5.14: (A) Depolarization wavefront at 18.62 ms after STIM1 (black and red mean resting and depolarized states, respectively). (B), (C) and (D) Arrival of the three simulated wavefronts at the observation point **P** (yellow triangle) at 18.62 ms (STIM1), 10.08 ms (STIM2) and 14.3 ms (STIM4), respectively. Results obtained with STIM3 are omitted for visualization purposes.

Fig. 5.14 A presents the depolarization wavefront at 18.62 ms (instant when the wave crosses the point of observation **P** indicated by an yellow triangle) after delivering a stimulus at position STIM1. Color coding refers to depolarized (red) and quiescent (black) cells. Fig. 5.14 B-D depicts the arrival of the wavefronts at **P** according to STIM1, STIM2 and STIM4, respectively. Results obtained with STIM3 are omitted for visualization purposes. Note that collisions happen close to **P** during STIM1 and STIM2, but not when retrograde conduction arises (STIM4).

Fig. 5.15 presents the distribution of FI for all four simulations. It can be seen that signals with only one deflection are the majority, meaning that uniform conduction following the clear direction of parallel fibers is dominant and independent of the stimulus site. However, this whole tissue quantification is likely to cover some specific areas of complex local conduction. For instance, CFAEs are expected to appear more frequently in zones of very complex microstructure (e.g. subregion A2 in Fig. 5.14 A). Indeed, Fig. 5.16 illustrates the time derivative of the electrograms computed at point **P** for simulations with stimuli STIM1, STIM2 and STIM4. Note that during STIM1 two events can be readily seen in $\dot{\phi}_e$. STIM2 generates a fairly uniform peak meaning that there is only one dominant wavefront arriving at **P**. STIM4, on the other hand, produces the most CFAE at **P** (three peaks). The depolarization wavefront at the instants of each of the three peaks (LAT1, LAT2 and LAT3) is also depicted on the right hand side of Fig. 5.16. The time instant of most prominent peak in Fig. 5.16 C corresponds to the arrival of the wavefront at **P** (Fig. 5.16 E), while the other two peaks relate to distal events (Fig. 5.16 D and Fig. 5.16 F).
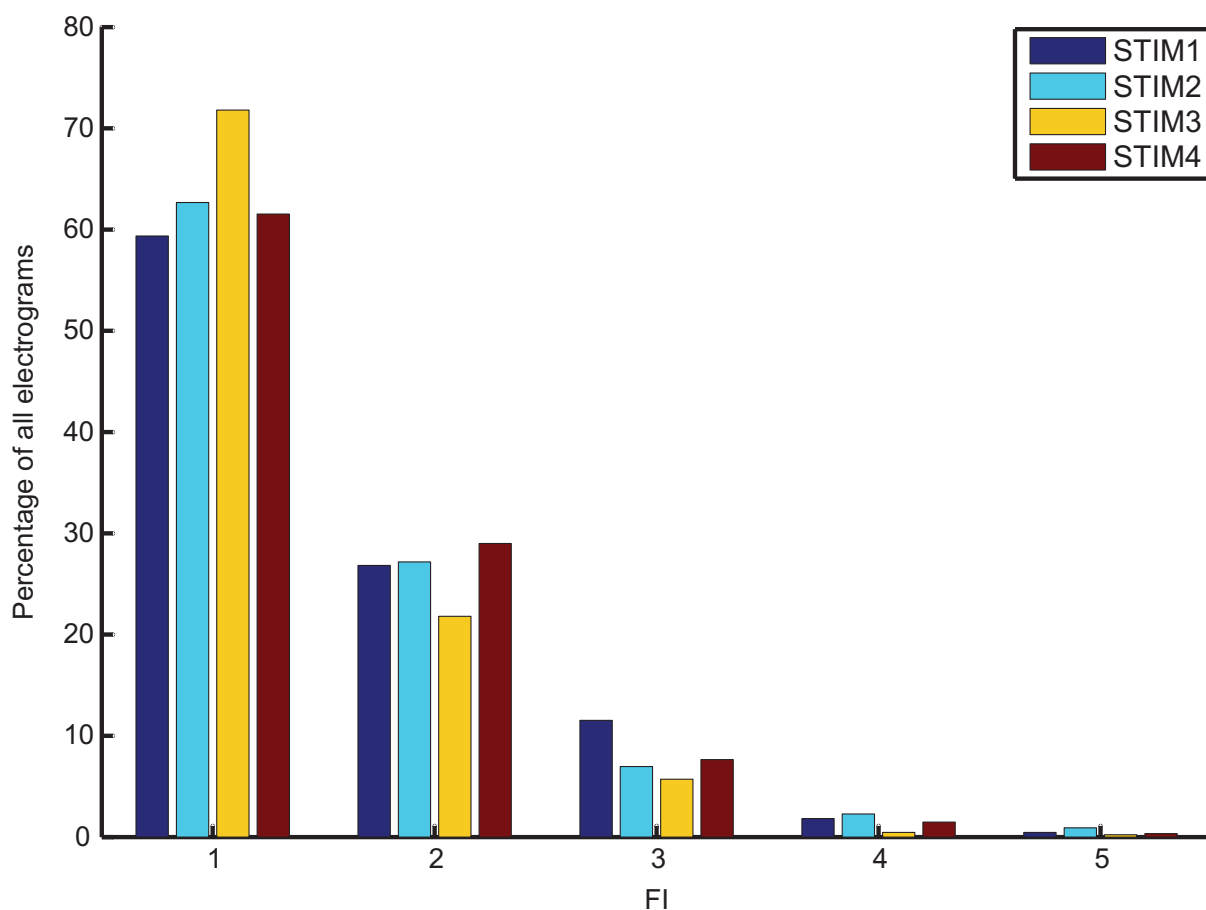
Figure 5.15: Histogram of the Fractionation Index (FI) for all four stimulus sites. Signal analysis performed with the help of Thomas Wiener[†].

[†]Institute of Biophysics, Medical University of Graz, Austria.
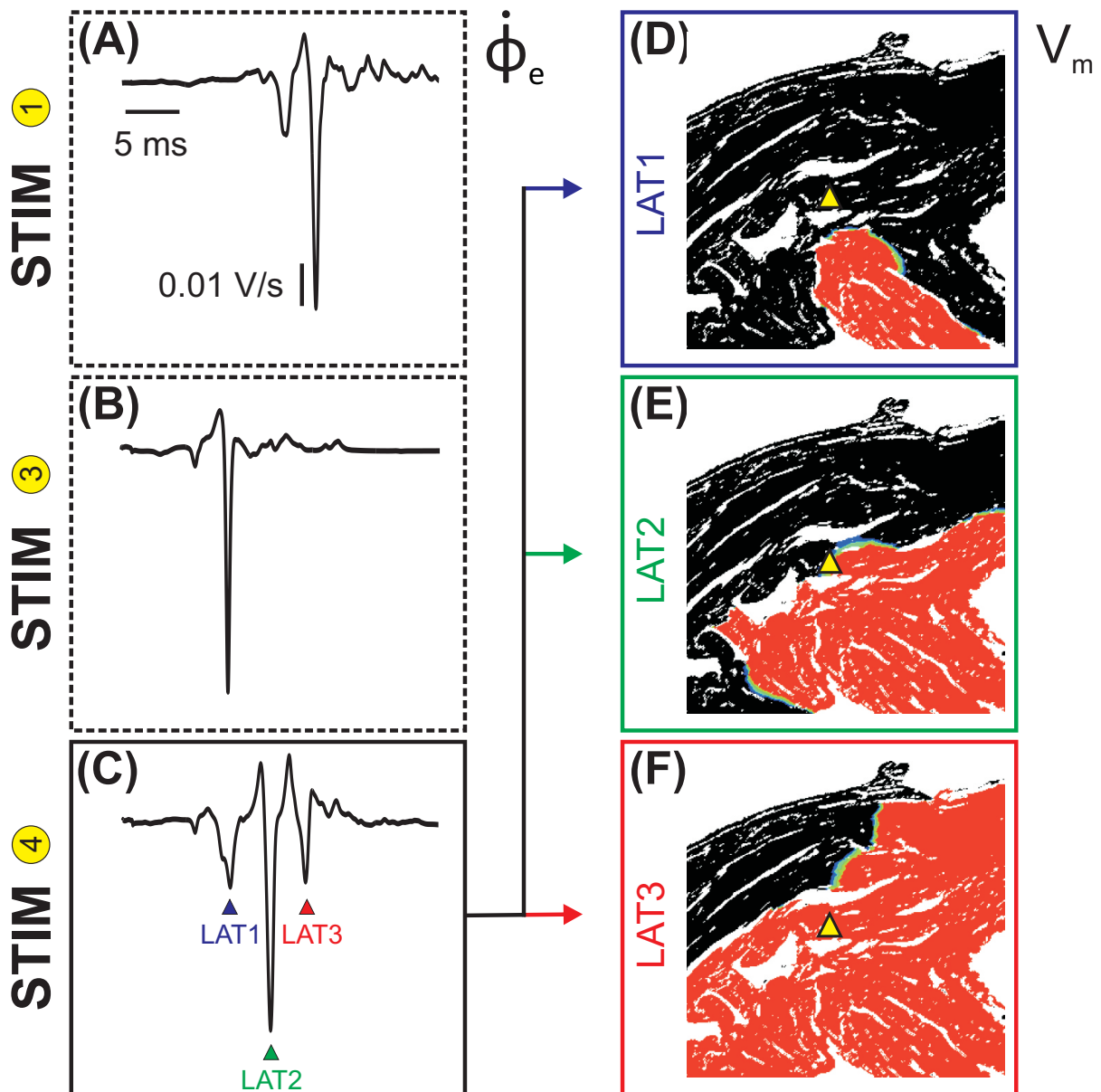
Figure 5.16: Time derivatives $\dot{\phi}_e$ computed at the observation point **P** (yellow triangle) during STIM1 (A), STIM2 (B) and STIM4 (C). Depolarization wavefront during STIM4 at instants LAT1 (D), LAT2 (E) and LAT3 (F) indicated in (C).

The behavior of electrograms as well as CNF signals in two subregions A1 and A2 (see Fig. 5.14 A) are presented in Figs. 5.17-5.18. These regions were chosen because they represent different spatial organization of microstructure.
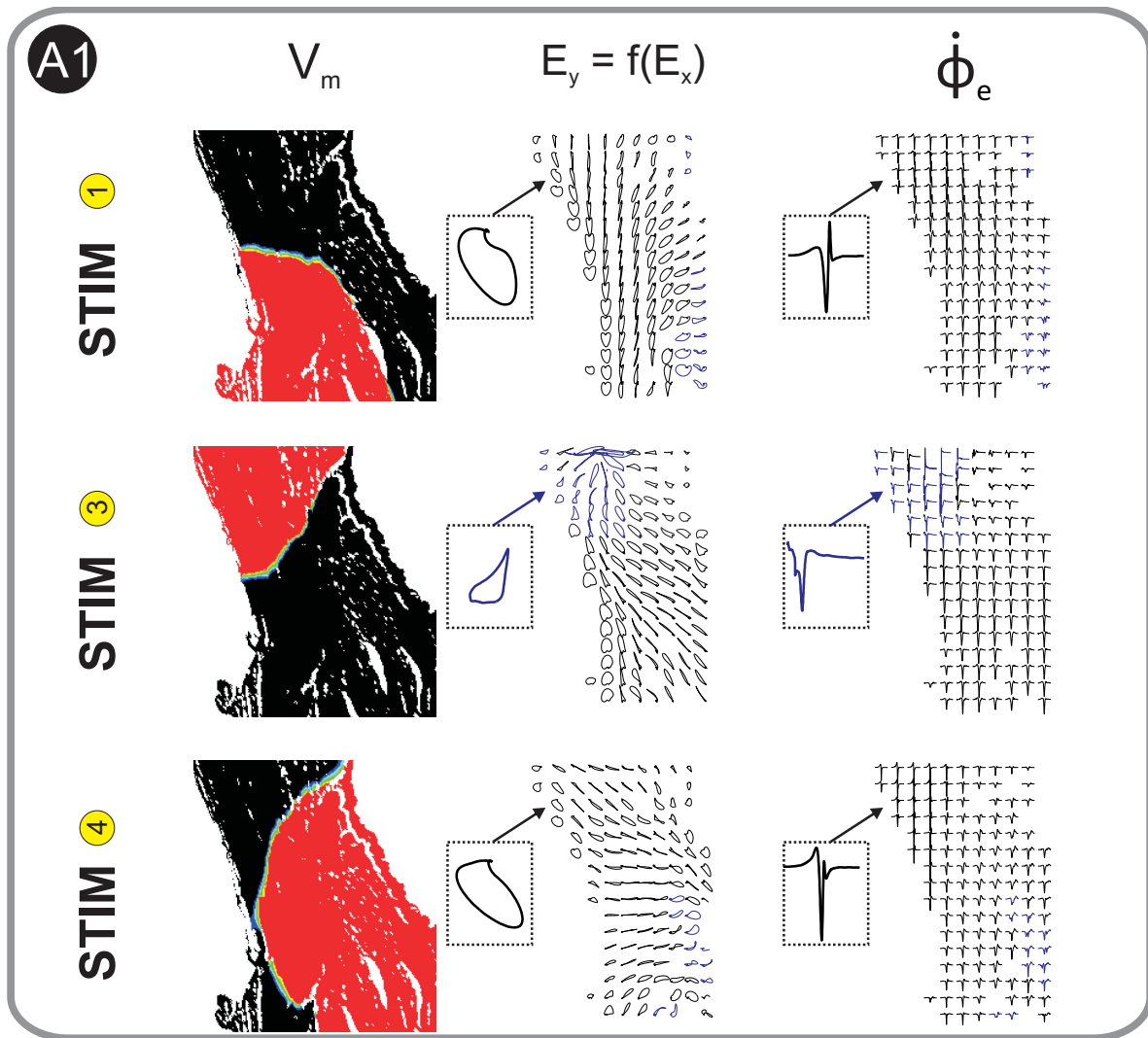
Figure 5.17: Depolarization wavefronts (left panel) traveling through subregions A1 from three different stimulus sites: STIM1, STIM3 and STIM4 (see Fig. 5.14 A). STIM1 and STIM2 led essentially to the same results, thus, STIM2 is omitted. Color coding refers to V_m (black and red mean resting state depolarized states, respectively). The images are rotated in 90°in relation to Fig. 5.14 A. Vector-loops of $\mathbf{E}$ (middle panel) and $\dot{\phi}_e$ (right panel) are also shown: colors refer to the degree of fractionation FI = 1 (black) and 2 (blue). Inset: highlighting of directional effects of the wavefront on $\mathbf{E}$ and $\dot{\phi}_e$.

Fig. 5.17 (left panel) shows how the wavefronts initiated from three different pacing sites propagate into subregion A1 (since the results obtained with STIM1 and STIM2 were very similar, STIM2 was omitted). Note that regardless the origin of the activation, the wavefront enters A1 always with a low curvature. It can be seen that conduction is longitudinal antegrade in STIM1 and longitudinal retrograde in STIM3 whereas pacing at STIM4 induces transverse conduction in A1. This is also demonstrated in the vector-loops of $\mathbf{E}$ depicted in Fig. 5.17 (middle panel), whose peaks are pointing in the opposite direction to local propagation spread. Table 5.1 (p. 88) and Figure 5.17 (right panel)
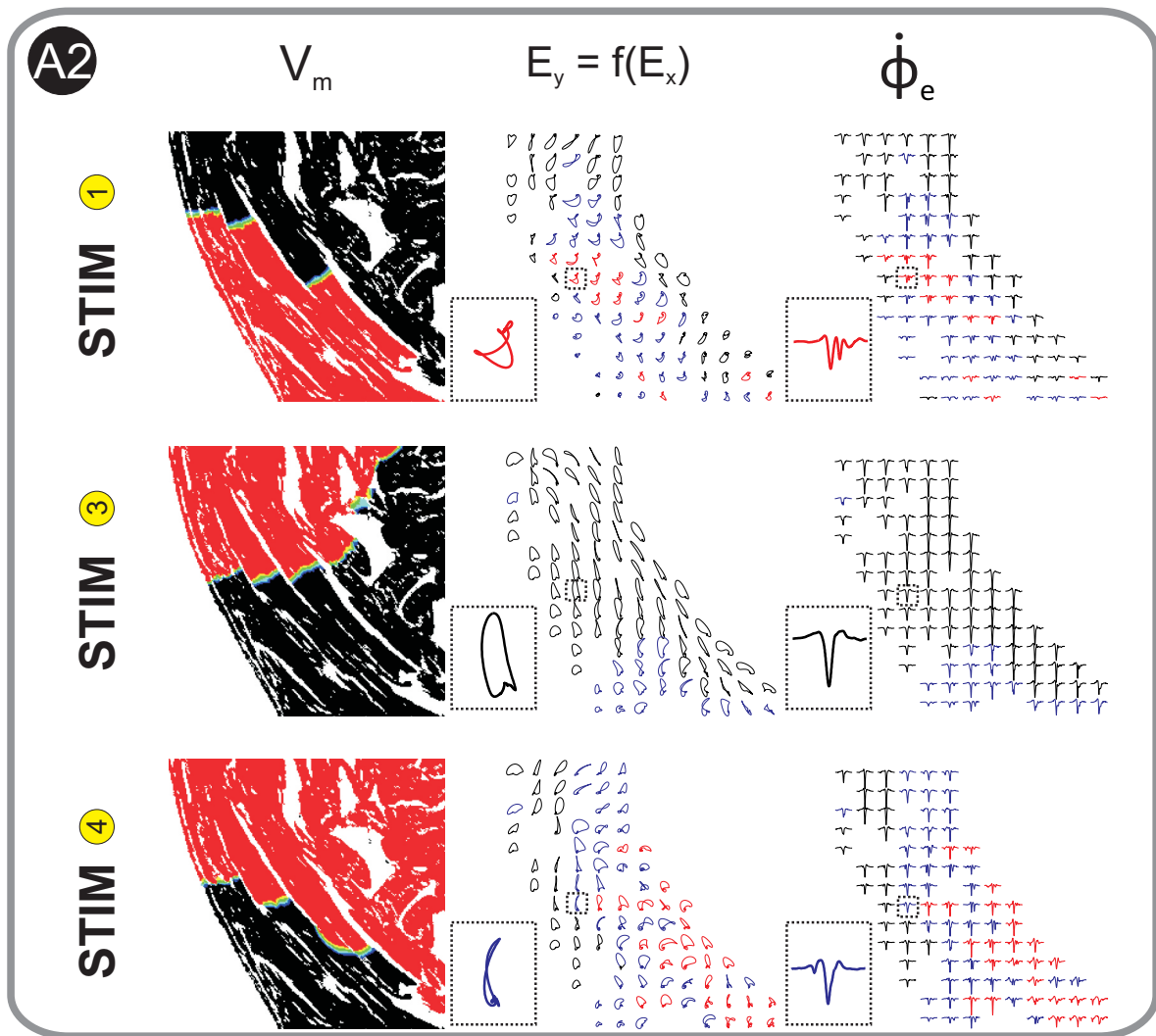
Figure 5.18: Depolarization wavefronts (left panel) traveling through subregions A2 from three different stimulus sites: STIM1, STIM3 and STIM4. Vector-loops of $\mathbf{E}$ (middle panel) and $\dot{\phi}_e$ (right panel) are also shown: colors refer to the degree of fractionation FI = 1 (black), 2 (blue) and 3 or more (red). Inset: highlight of directional effects.

demonstrate that conduction in A1 is quite uniform with dominance of UAE (with at least 54 out of 56 recording sites) due to its electrically well coupled structure. $\hat{\dot{\phi}}_e$ and $\hat{E}$ are similar during antegrade and retrograde longitudinal conduction (STIM1 and STIM3) whereas during transverse conduction both parameters are decreased (STIM4).

Regarding A2, considerable delays of the wavefronts among three muscle bundles were detected (see Fig. 5.18 - left panel) when pacing in STIM1 and STIM4, respectively, but not when the activation was started in STIM3. In STIM1, this is expressed by CFAE as shown in Fig. 5.18 (right panel). The number of fractionated electrograms (N2 and N3+) account for 72% of the signals (Table 5.2) and $\hat{\dot{\phi}}_e$ as well as $\hat{E}$ are smaller when compared with the other two pacing sites. However, when the wavefront starts from STIM3, the profile changes and the UAE dominates again (Fig. 5.18 and Table 5.2). STIM3 produces

Table 5.1: Changes of conduction parameters in subregion A1. Fractionation index FI = 1 (N1), 2 (N2) and more than 3 (N3+), mean μ and standard deviation σ of $\hat{\phi}_e$ and $\hat{E}$. Signal analysis performed with the help of Thomas Wiener[‡].

Stimulus	FI			$\hat{\phi}_e$ (N = 56)		$\hat{E}$ (N = 56)	
site	N1	N2	N3+	μ	σ	μ	σ
STIM1	56	0	0	70.45	14.08	84.36	9.610
STIM3	52	1	3	64.98	11.13	82.92	10.03
STIM4	53	3	0	54.14	12.71	71.95	9.370

Table 5.2: Changes of conduction parameters in subregion A2.

Stimulus	FI			$\hat{\phi}_e$ (N = 76)		$\hat{E}$ (N = 76)	
site	N1	N2	N3+	μ	σ	μ	σ
STIM1	22	33	21	24.59	10.81	34.73	10.89
STIM3	57	17	2	60.05	20.63	66.98	18.77
STIM4	25	37	14	47.51	15.42	47.48	12.42

less complex vector-loops and $\hat{\phi}_e$ as well as $\hat{E}$ are twice as large than in STIM1. Because results obtained with STIM2 and STIM3 were very similar, STIM2 was again omitted.

5.3.2 Classification of Microfibrosis

Subregions of $1\,\mathrm{mm}^2$ cardiac tissue representing three types of spatial organization of the microstructure were sought by visual inspection of Fig. 4.8 in p. 57. In total, six subregions were chosen for the classification procedures. First, image processing techniques were applied in order to obtain a quantitative definition of three types of microstructural organization listed below. Subsequently, computer simulations were conducted aiming to classify the same six subregions through inspection of recovered extracellular electrograms. Characteristics of electrograms (details in Sect. 4.5.2, p. 53) computed within all subregions were considered for analysis. Furthermore, as shown in the previous section, electrogram waveform depends not only on the structure of the subjacent tissue but also on the direction of the activation wavefront. Therefore, the tissue was sequentially stimulated at multiple sites arranged on a virtual circle around the area under investigation (stimulation protocol is described in Sect. 4.4.3, p. 51). From the set of electrograms obtained from each simulation, appropriate features were extracted, as de-

---

[‡]Institute of Biophysics, Medical University of Graz, Austria.

scribed in Sect. 4.5.5, p. 58, and related to the following types of cardiac microstructure:

- Well coupled densely packed tissue (WCDP)

- Uncoupled tissue with uncoupling structures oriented parallel to the cardiac fibers (UCPO)

- Uncoupled tissue with multidirectional arrangement of uncoupling structures (UCMO)

Image Processing

In order to estimate the degree of fibrosis, the percentage amount of myocytes, connective tissue and interstitial clefts was calculated in each of the six subregions selected in Fig. 4.8, p. 57. Fig. 5.19 presents the results obtained. Well coupled densely packed tissue (WCDP) is characterized by a large amount of myocytes ($> 75\%$) in comparison to the uncoupling structures. In uncoupled tissue, on the other hand, the amount of fibrosis as well as interstitial clefts increases significantly. Note that in the case where the collagen fibers are aligned with the myofibers (UCPO), myocytes still account for about 50% of the $1\,\text{mm}^2$ area of tissue. The largest amount of fibrosis was found in the second case of uncoupled tissue with multidirectional arrangement of uncoupling structures (UCMO2). This is due a large patch of fibrotic tissue (22% of the area) as can be seen in Fig. 4.8 (p. 57, lower panel, right column).
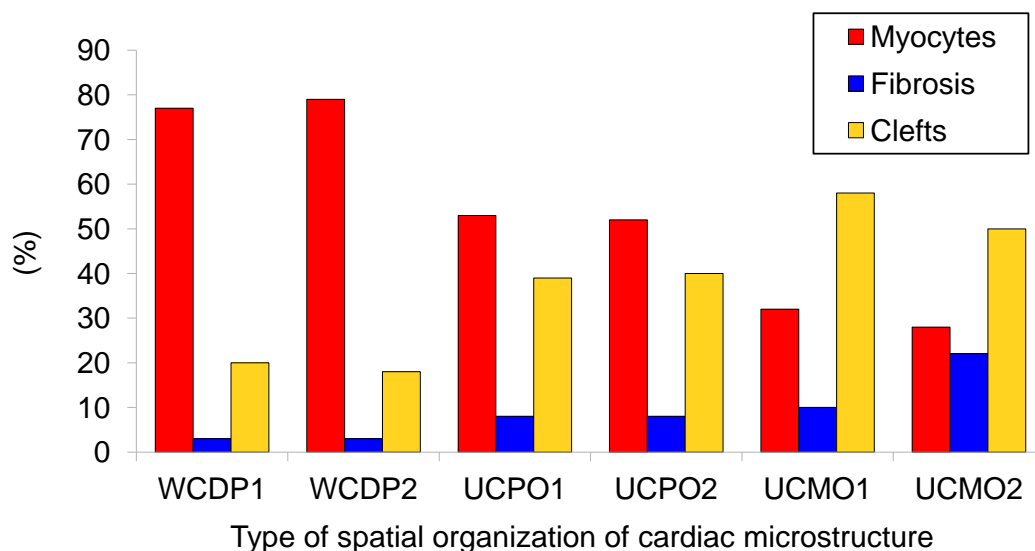
Figure 5.19: Amount of myocytes, connective tissue (fibrosis) and interstitial clefts within the six subregions ($1\,\text{mm}^2$) of cardiac tissue shown in Fig. 4.8, p. 57: well coupled densely packed tissue (WCDP), uncoupled tissue with uncoupling structures oriented parallel to the cardiac fibers (UCPO), and uncoupled tissue with multidirectional arrangement of uncoupling structures (UCMO).

In addition to the degree of uncoupling, the deviation between the average of angles of the cardiac myofibers and collagen fibers within subregions with uncoupling structures was computed. This measure was considered to quantify the spatial organization of microfibrosis in relation to the cardiac fibers. According to Tab. 5.3, the angular deviation is small (~ 0) when both cardiac and collagen fibers are aligned and increases in the case of multidirectional arrangement of uncoupling structures (> 0.1).

Table 5.3: Deviation between angles formed by the cardiac (θ_1) and collagen (θ_2) fibers within subregions with uncoupling structures as shown in Fig. 4.8, p. 57.

Type of cardiac microstructure	Angle deviation $||\theta_1 - \theta_2||$
UCPO1	0.04
UCPO2	0.00
UCMO1	0.21
UCMO2	0.32

Thus, thresholds for both degree and spatial orientation of the cardiac microstructure can be set. For instance, a $1\,\mathrm{mm}^2$ portion of cardiac tissue can be said to be well coupled if at least 60% of this area is composed by myocytes. Regarding the orientation of uncoupling structures, angular deviations between cardiac and collagen fibers larger than 0.1 are associated with subregions, where uncoupling structures show multidirectional arrangements.

Extracellular Potentials

The multisite pacing technique presented previously was used to further investigate the dependence of the electrogram's waveform on the underlying microstructure as well as on the direction of the depolarization wavefront. Different from Sect. 5.3.1, where only four stimuli were applied at different sites, here stimulus currents were applied to the tissue according to the circumferential protocol described in Sect. 4.4.3, p. 51. In total, twelve simulations were performed for each of the six areas under investigation. Fig. 5.20 A, p. 92, shows a schematic view of how the 12 stimuli were arranged in $30°$ in a circumference around an area of well coupled densely packed tissue (WCDP1).

Fig. 5.20 B-C, p. 92, present the mean of fractionation index (FI) μ_{FI} and mean amplitudes μ_{amp} of the 121 electrograms computed within the subregion for each of the 12 stimuli. Note that regardless the direction of the depolarization wavefront (stimulus site) the μ_{FI} is close to 1 (ΔFI small), i.e., UAEs dominate. The amplitudes of the signals on the other hand, change substantially according to the direction of the wavefront.

Wavefronts initiated at stimulus sites positioned at 30°and 240°, for instance, enter the area of observation transverse to the cardiac fibers. Stimulation at positions 120°and 330°, on the other hand, induce longitudinal propagation. The differences in amplitudes are due to the strong anisotropy of the tissue (conductivities are higher along the fibers). Similar results were obtained applying the circumferential protocol to the second example of well coupled densely packed tissue (WCDP2) as shown in Fig. 5.21, p. 92.

Figs. 5.22-5.23, p. 93, present the results obtained with circumferential stimulation protocol in 1 mm^2 areas of uncoupled tissue with uncoupling structures oriented parallel to the cardiac fibers (UCPO). In contrast with the well coupled tissue, the directional effects of the wavefront on FI is more pronounced. In Fig. 5.22, stimulation at 30° - 90° give rise to UAEs, i.e., electrograms with only one peak (FI = 1). When a stimulus is delivered at position 330°, for example, conduction follows a tortuous course around the collagen fiber. This change in conduction resulted in CFAEs, i.e., FI > 1. Signal amplitudes are smaller than in the well coupled case due to slow conduction caused by the presence of uncoupling structures. Anisotropy also accounts for the changes in amplitudes from stimulus to stimulus (note a symmetry in Fig. 5.22 C and Fig.5.23 C, p. 93).

The morphology of electrograms was also analyzed in areas where microstructure is characterized by uncoupled tissue with multidirectional arrangement of uncoupling structures (UCMO), see Figs. 5.24-5.25, p. 94. Unlike the cases where the uncoupling structures have a preferential orientation, fractionation occurs despite the origin of the wavefront. Note in Fig 5.25 B that $2 \leq$ FI ≤ 3 due to a large patch of fibrotic tissue, which impairs conduction. The amplitudes also do not change from stimulus to stimulus.

The results in Figs. 5.20-5.25, pp. 92-94 were lumped into three features: m_{FI}, ΔFI and ξ_{amp} (see Sect. 4.5.5, p. 58). Fig. 5.26 in p. 95 shows 3D and 2D scatter-plots of the selected features. The clustering of the objects in the feature space suggests a good separability into the three classes considered in this thesis: WCDP, UCPO and UCMO. Tab. 5.4 in p. 95 presents the classification accuracies for each of the three classes (acc_1 for WCDP, acc_2 for UCPO, and acc_3 for UCMO) as well as the overall accuracy acc_{tot} (see Eqs. 4.14-4.15 in Sect. 4.5.5, p. 58), achieved by the linear discriminant analysis (LDA). Tab. 5.5 and Tab. 5.6, in p. 96, present the results for $s = 6$ (the number of stimulus sites) and $s = 3$, respectively.
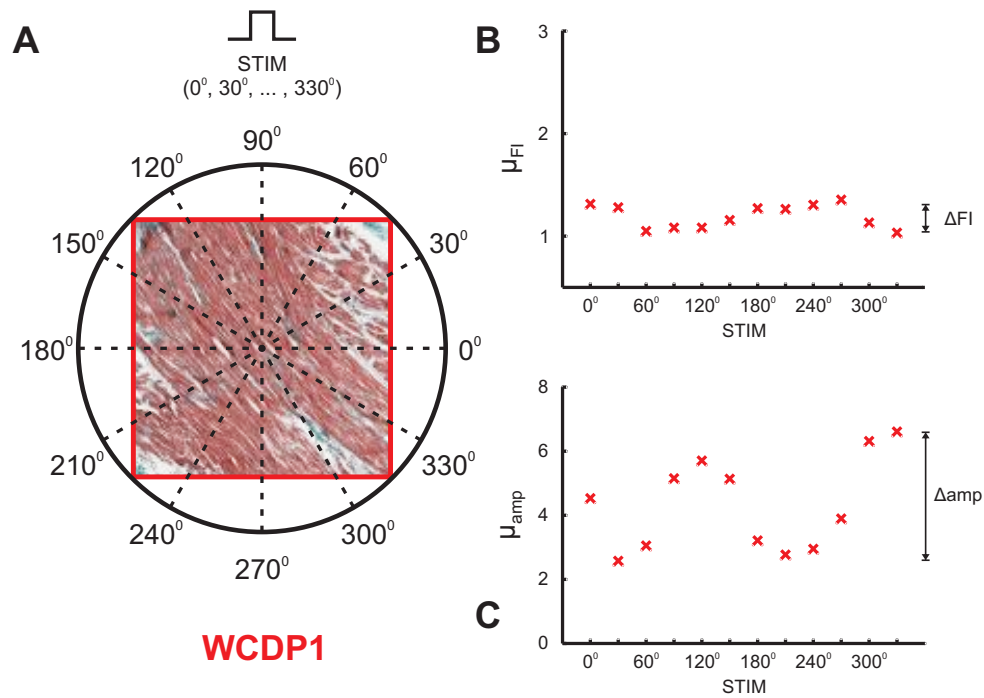
Figure 5.20: Results obtained stimulating around a $1\,\text{mm}^2$ area of well coupled densely packed tissue 1 (WCDP1). (A) Schematic representation of how each of the 12 stimuli (from 0°to 330°) were applied. (B) Mean fractionated indexes μ_{FI} and (C) Mean amplitudes μ_{amp} of 121 electrograms computed in a square grid spaced by $100\,\mu\text{m}$ for each stimulus. ΔFI and Δamp are the ranges of FI and amplitudes, respectively.
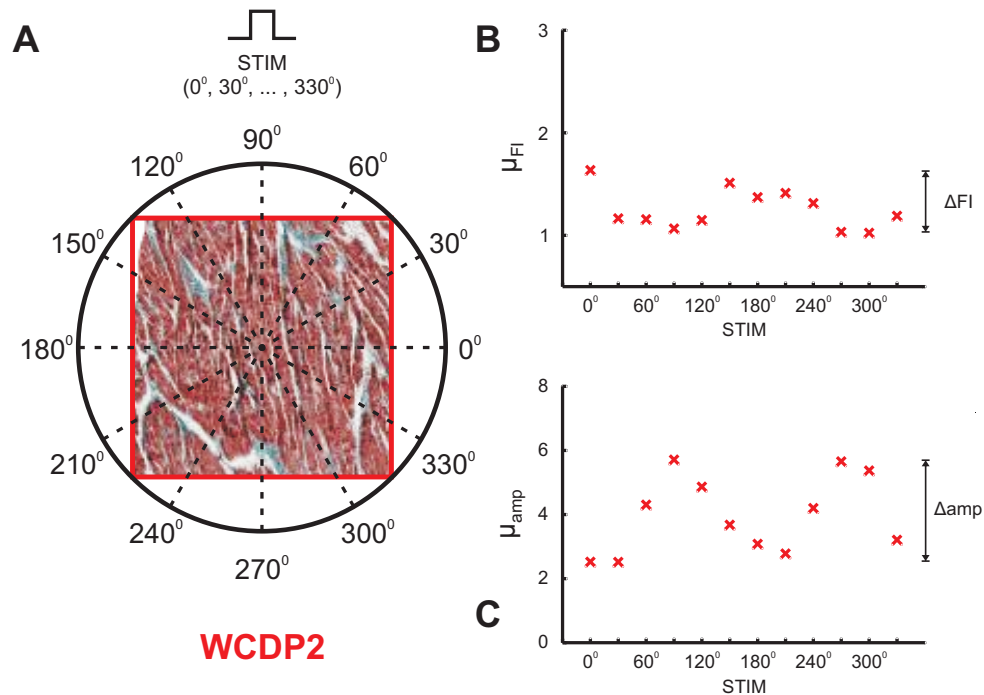
Figure 5.21: Results obtained stimulating around a $1\,\text{mm}^2$ area of well coupled densely packed tissue 2 (WCDP2).
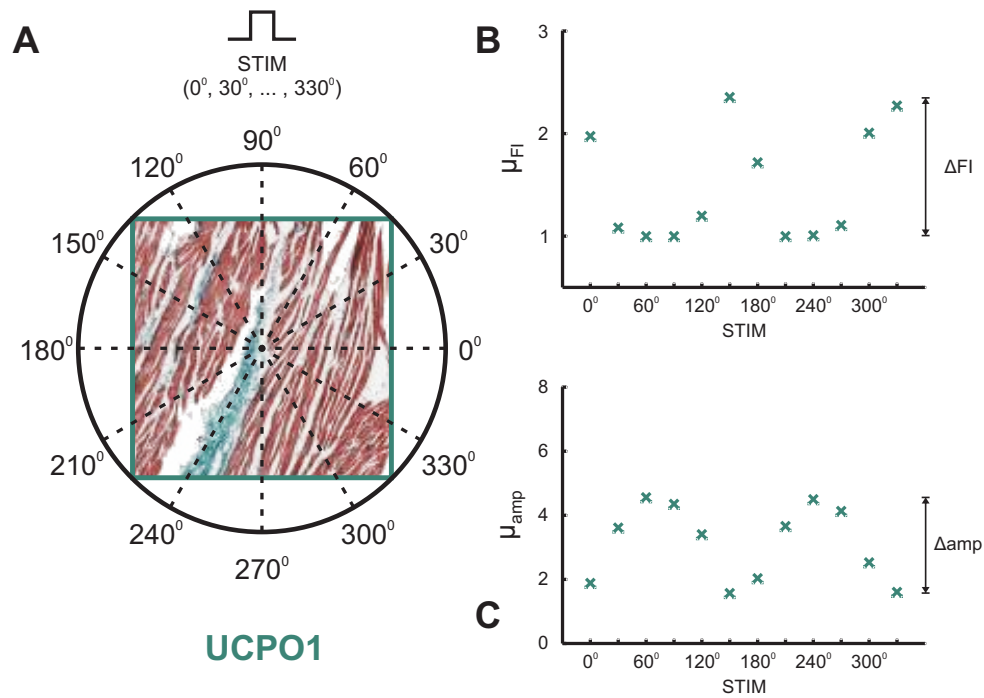
Figure 5.22: Results obtained stimulating around a $1\,\mathrm{mm}^2$ area of uncoupled tissue with uncoupling structures oriented parallel to the cardiac fibers 1 (UCPO1). (A) Schematic representation of how each of the 12 stimuli (from 0°to 330°) were applied. (B) Mean fractionated indexes μ_{FI} and (C) Mean amplitudes μ_{amp} of 121 electrograms computed in a square grid spaced by $100\,\mu\mathrm{m}$ for each stimulus.
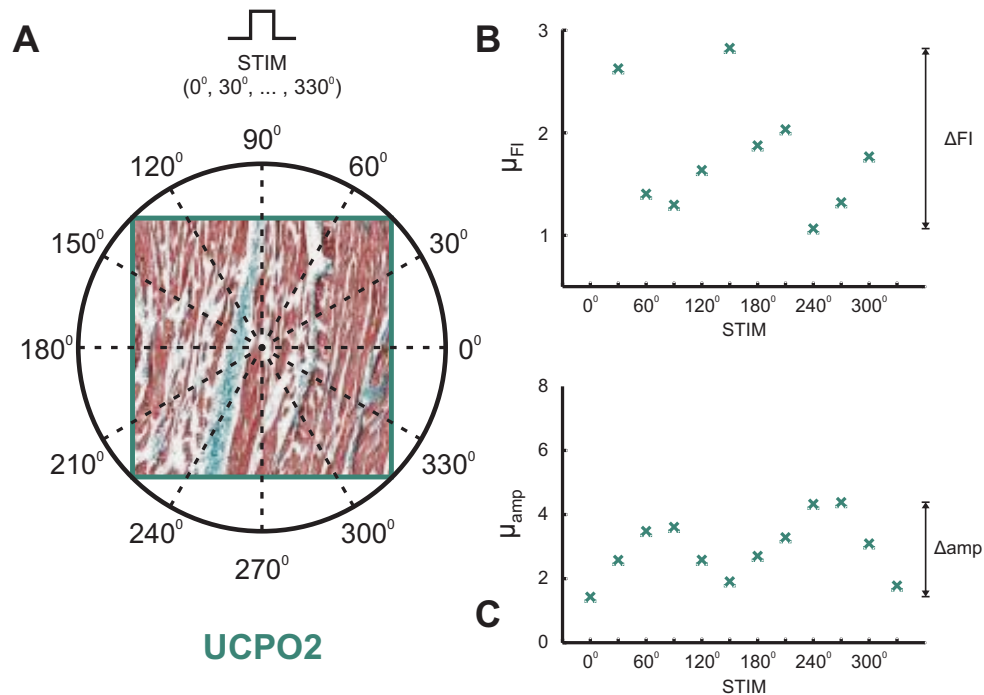
Figure 5.23: Results obtained stimulating around a $1\,\mathrm{mm}^2$ area of uncoupled tissue with uncoupling structures oriented parallel to the cardiac fibers 2 (UCPO2).
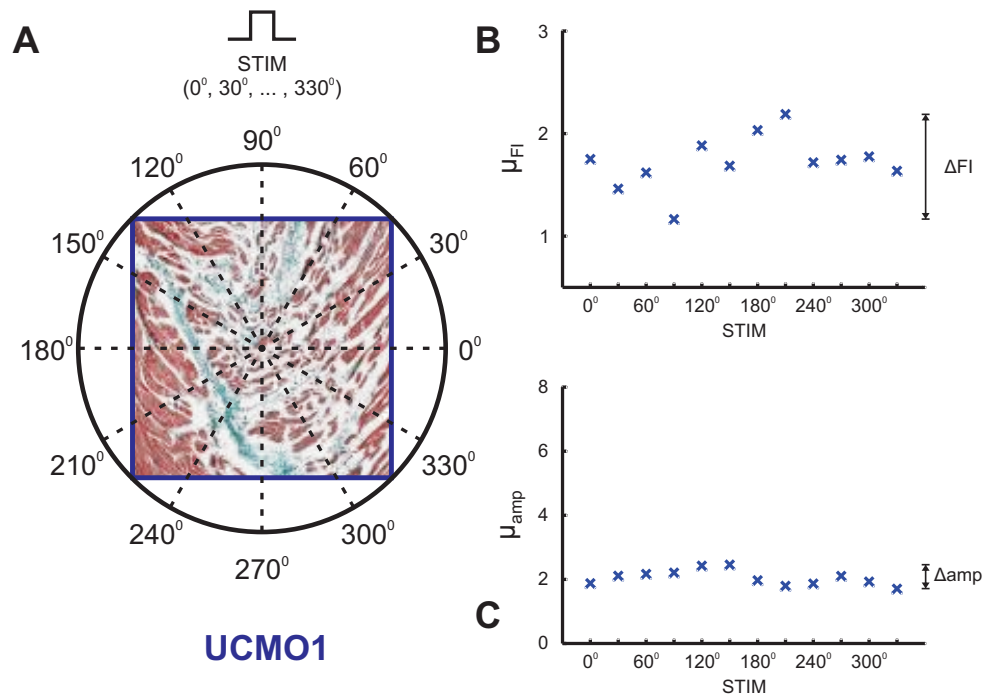
Figure 5.24: Results obtained stimulating around a $1\,\text{mm}^2$ area of uncoupled tissue with multidirectional arrangement of uncoupling structures 1 (UCMO1). (A) Schematic representation of how each of the 12 stimuli (from 0°to 330°) were applied. (B) Mean fractionated indexes μ_{FI} and (C) Mean amplitudes μ_{amp} of 121 electrograms computed in a square grid spaced by $100\,\mu$m for each stimulus.
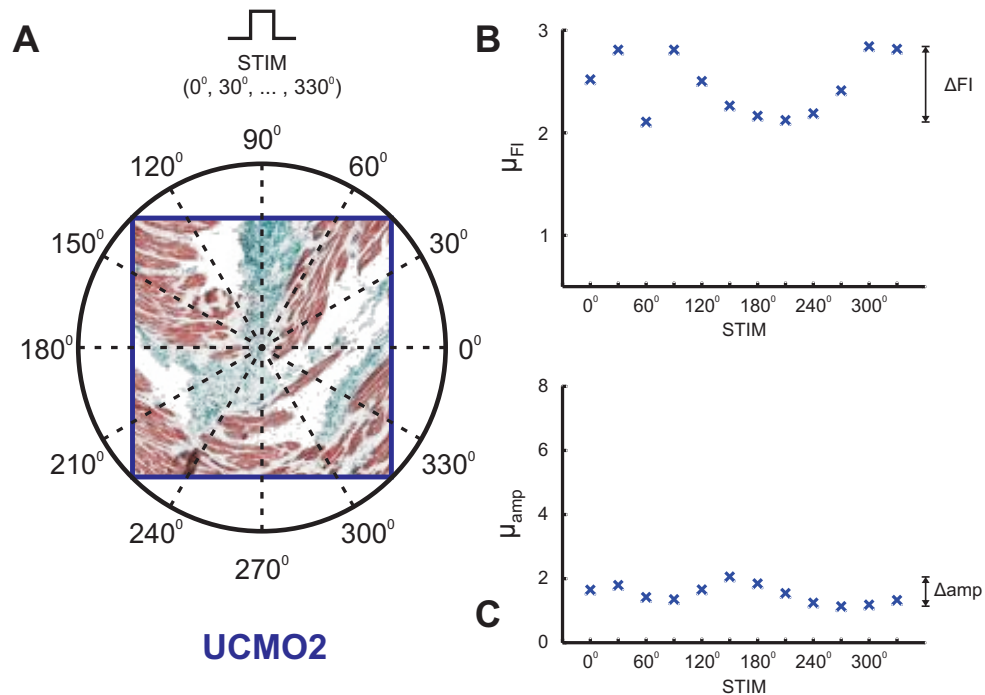
Figure 5.25: Results obtained stimulating around a $1\,\text{mm}^2$ area of uncoupled tissue with multidirectional arrangement of uncoupling structures 2 (UCMO2).
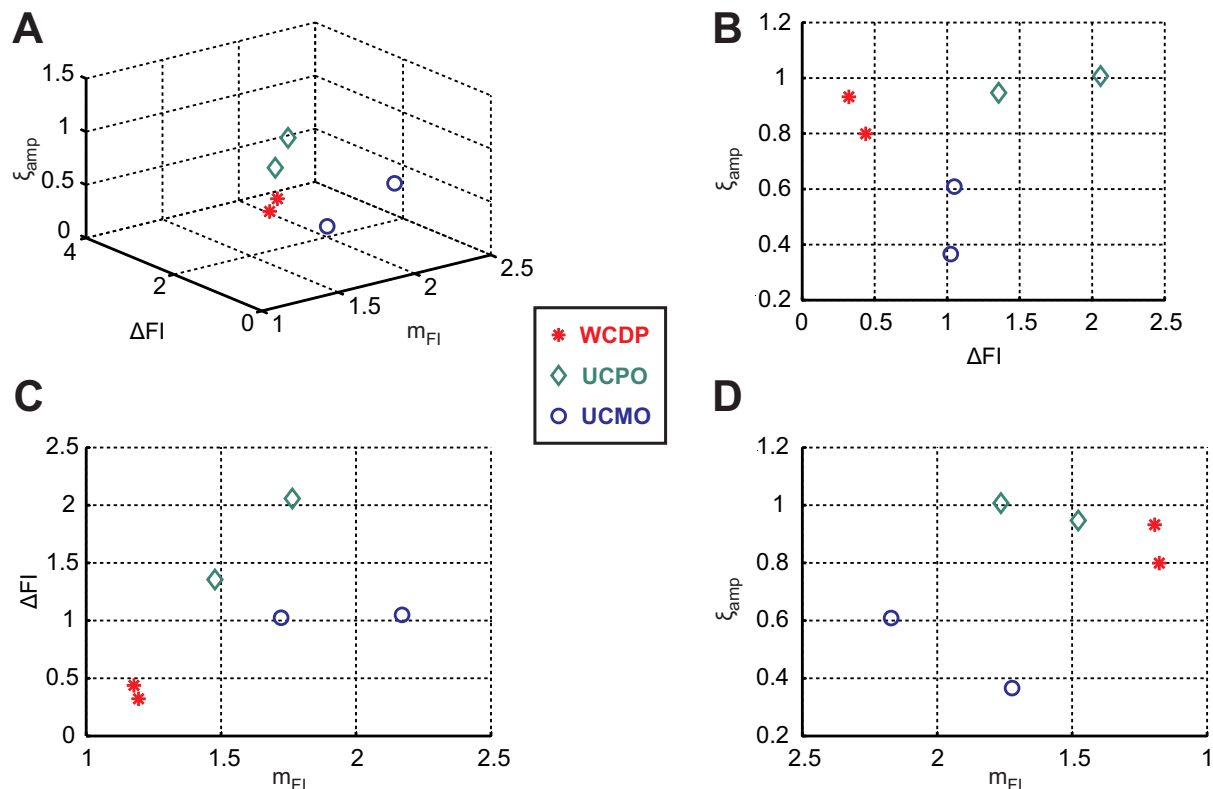
Figure 5.26: Features selected for the classification procedure. (A) 3D plot of m_{FI}, ΔFI and (ξ_{amp}) from all measurement sites and for all stimulus sites. (B) 2D plot of ΔFI vs. ξ_{amp}. (C) 2D plot of m_{FI} vs. ΔFI. (D) 2D plot of m_{FI} vs. ξ_{amp}.

Table 5.4: Classification results for $s = 12$ stimulus sites, for features obtained from electrograms recorded in a grid with varying length d. Classification accuracies, i.e., the fraction of correctly classified samples are given for each of the three classes (acc_1 for WCDP, acc_2 for UCPO, and acc_3 for UCMO) as well as the overall accuracy acc_{tot} (details in Sect. 4.5.5). Signal analysis and classification were performed with the help of Thomas Wiener[§].

d μm	Recording sites	acc_1	acc_2	acc_3	acc_{tot}
100	121	1.00	1.00	1.00	1.00
200	36	1.00	1.00	1.00	1.00
300	15	1.00	1.00	1.00	1.00
400	9	0.97	0.97	1.00	0.98
600	4	0.93	0.91	0.99	0.94

[§]Institute of Biophysics, Medical University of Graz, Austria.

Table 5.5: Classification results for $s = 6$. Classification was performed with the help of Thomas Wiener[¶].

d μm	Recording sites	acc_1	acc_2	acc_3	acc_{tot}
100	121	1.00	1.00	1.00	1.00
200	36	1.00	1.00	1.00	1.00
300	15	0.96	0.96	1.00	0.97
400	9	0.98	0.98	1.00	0.98
600	4	0.90	0.87	0.99	0.92

Table 5.6: Classification results for $s = 3$.

d μm	Recording sites	acc_1	acc_2	acc_3	acc_{tot}
100	121	1.00	0.83	0.83	0.89
200	36	1.00	0.87	0.88	0.92
300	15	1.00	0.87	0.89	0.92
400	9	0.99	0.84	0.87	0.90
600	4	0.90	0.70	0.85	0.82

5.3.3 Discussion

In this thesis, a histologically detailed computer model accounting for the complex spatial organization of microfibrosis was established. The occurrence of CFAEs and their relation to the degree as well as the spatial organization of microfibrosis have been investigated. Different regions representing three types of tissue microstructure in the right atrial isthmus were analyzed: well coupled densely packed tissue; uncoupled tissue with uncoupling structures oriented parallel to the cardiac fibers; and uncoupled tissue with multidirectional arrangement of uncoupling structures (Fig. 4.8). Previous modeling studies have demonstrated that the presence of CFAEs also depends on the direction of propagation with respect to the fiber orientation.[136,140] In this work, the direction of the wavefront was induced via multi-site pacing in order to obtain information about spatial organization of microfibrosis.

[¶]Institute of Biophysics, Medical University of Graz, Austria.

Feature Selection and Classification

The results obtained with the histologically detailed model demonstrated that amplitudes of the signals, as shown in Fig. 5.20 (left panel), are influenced by tissue anisotropy. A new approach to characterizing tissue microstructure through extracellular electrograms is to take the directional dependence of signal amplitude and fractionation into account. CFAEs occurred in areas with uncoupling structures running parallel to the cardiac fibers when the wavefront entered the area of observation perpendicularly to the fiber orientation (Fig. 5.22). Longitudinal propagation, i.e. wavefront traveling along fiber direction, gave rise to UAEs. In contrast, areas with multidirectional arrangement of microfibrosis showed complex signals with smaller amplitudes regardless the origin of the wavefront.

The set of features (m_{FI}, ΔFI, ξ_{amp}) describing the objects were taken as lumped information based on conduction parameters obtained from sets of electrograms (Sect. 4.5.2) computed after applying the circumferential protocol. The choice of features based on FI and signal amplitudes is supported by observations of these two quantities in previous computer simulation and experimental studies.[3,140] Additional features, as for instance, the local activation time (LAT) dispersion within fractionated electrograms might improve the classification accuracy. However, an increase in the number of features does not necessarily lead to higher accuracies.

The use of LDA was the first attempt to classify tissue microstructure based on features extracted from sets of electrograms. It was chosen because scatter plots of the three-dimensional feature space suggested a good separability by planes. Nevertheless, other classifiers may lead to a higher classification accuracies.

The leave-one-out method for cross-validation was chosen because only two samples per class (6 samples of tissue subregions in total) were available. Other cross-validation methods would presumably deselect all samples of a certain class (e.g. all WCDP) from the set of training data or test data, respectively, and thus lead to a biased result of classification accuracy.

Number of Stimulus Sites and Number of Measurements

During experiments as well as catheter ablation procedures, the number of measurements is restricted by the mapping system. The relevance of the results for reduced number of stimulus and recording sites was examined. Tabs. 5.4, 5.5, and 5.6 reveal that the number of stimulus sites plays a major role in characterization of microfibrosis. The reduction of the number of stimulus sites had a stronger impact on the classification accuracy than the reduction of the grid density of recording electrodes. The results suggest that electrode arrays, arranged in a circumferential geometry, capable of measuring and stimulating in multiple locations could be useful tools to obtain information about the underlying tissue. The chosen values for the number of stimulus sites, the grid size, and

the number of recording electrodes are considered as technically feasible for *in vitro* experiments. Arrays with 32 electrodes with interelectrode spacing of $300\,\mu$m are available (*FlexMEA36; Multichannel Systems*, Reutlingen, Germany) in the market. In addition to that, electrode arrays capable of measuring multiple unipolar electrograms as well as stimulating tissue at different sites have been used[145] previously in *in vivo* experiments. Nonetheless, the results obtained in this work still depend upon the development of a new dedicated sensor* with a different geometry from those commercially available. Such sensor should be able to measure as well as stimulate in the same manner as the circumferential protocol.

Limitations

The 2D computer model used in this work is based on a single histological image of the rabbit right atrial isthmus. Although it accounts for structural heterogeneities due to microfibrosis and interstitial clefts, it does not represent effects of subsequent layers of tissue in 3D. The shunting layer used here is a rough approximation aiming to alleviate this shortcoming. The choice of $1\,\text{mm}^2$ was based on the fact that the tissue was obtained from an adult rather than an old rabbit. Thus, fibrotic tissue is found in a lesser degree. The human atria, on the other hand, are much larger and collagen may be found in large amounts. With regard to the limited number of tissue samples (2 samples per class, 6 samples in total) and the fact that the chosen sections represent clear examples of the respective class, the obtained classification accuracies might be too optimistic. Nevertheless, the results suggest conducting a continuative experimental study.

Furthermore, only point-like unipolar electrodes were considered in this study. Although systems capable of measuring electrograms at a very fine scale are available for experimental studies,[22] the variation in electrode size was shown to influence electrogram complexity due to spatial averaging aspects.[24]

---

*In progress at the Institute of Biophysics, Medical University of Graz, Austria.

5.4   Performance of a Cardiac Cell Solver on Modern Graphic-hardware

In this section, the numerical results obtained solving the systems of ODEs describing the electrical activity in atrial myocytes are presented. Simulations were performed using the Lindblad model[83] on graphics processing units through NVIDIA CUDA environment and on a CPU using OpenMP as described in Sect. 4.6.2. Simulations on the CPU were launched with 32 cores (eight Quad-Core AMD Opteron$^{\text{TM}}$ 8386 SE 2.8 GHz processors) and compared against simulations running on a single GPU (a NVIDIA GeForce GTX 260 graphic-hardware). All results, in terms of total execution time, are a mean of 10 simulations.

5.4.1   Multi-core CPU

Initially, the performance of the CPU implementation (using OpenMP) was studied with different number of processor cores. The same number of cell models needed to solve both macro (116 048 nodes) and micro (2 695 299 nodes) models of the ROI were simulated using up to 32 cores. Fig. 5.27 A presents the elapsed time to solve the ODEs. Using a single core, 540.91 s are required to solve all 116 048 systems of ODEs relative to the macroscopic model. As can be seen, the microscopic model is more computationally demanding since about 2.5 million cell models comprising of a system of 27 ODEs have to be solved at every time step. Indeed, 4 058.19 s are necessary to solve all equations using one processor core, meaning that the micro model is about 10 times slower than the macro model. Regarding scalability, both models achieved a linear parallel speedup (execution time on 1 processor/execution time) up to 4 cores as shown in Fig. 5.27 B. The macroscopic model achieved a better scalability on more than 8 processor cores. When using 32 cores, 10.69 s and 132.18 s were necessary to integrate the systems of ODEs in both macro- and microscopic models, respectively. This results in parallel gains of about 50 times (macro) and 30 times (micro) compared to simulations using a single core.
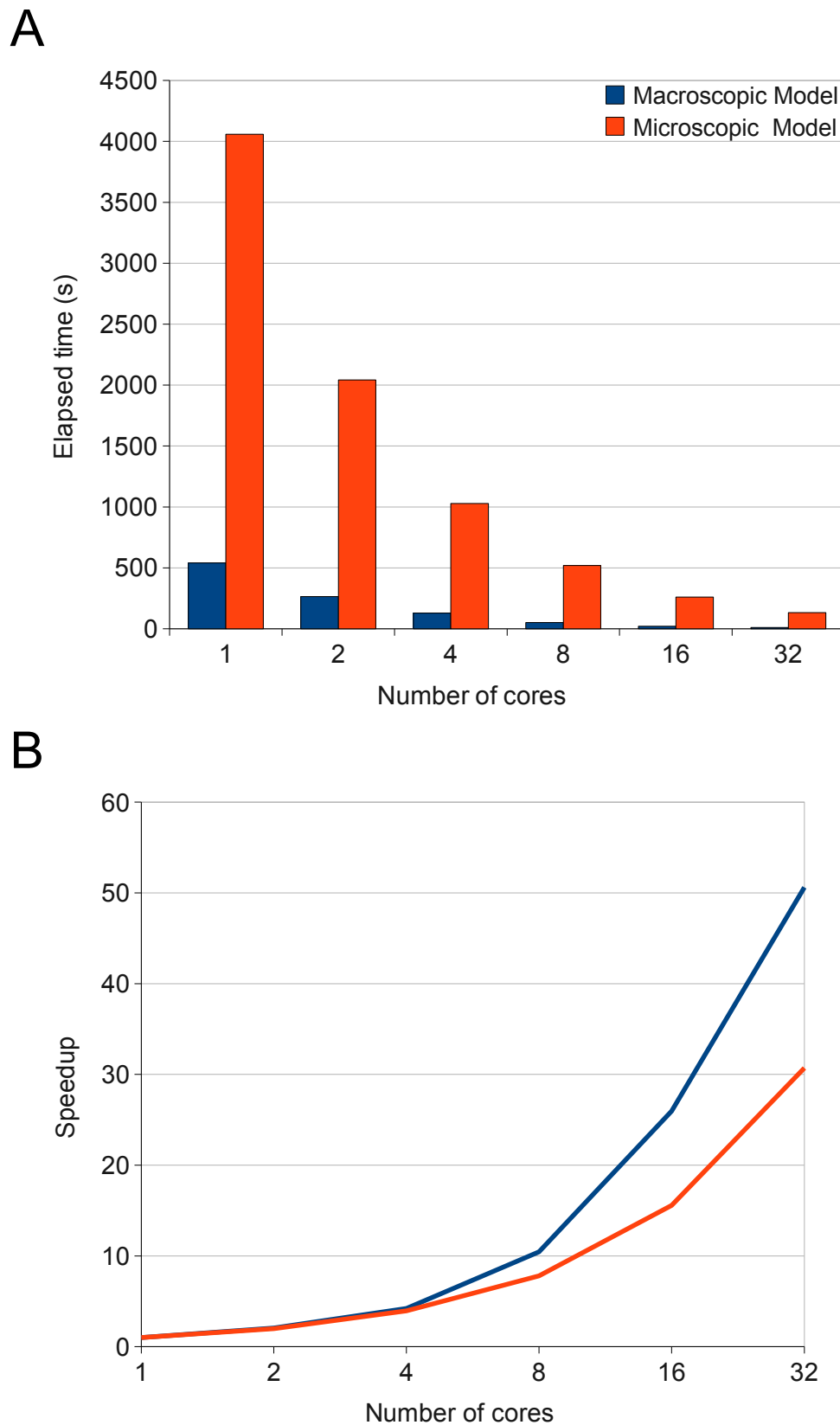
Figure 5.27: (A) Total execution times required to solve n atrial cell models needed to simulate the Macro- ($n = 116\,048$ nodes) and Microscopic ($n = 2\,695\,299$ nodes) models of the ROI using OpenMP with different number of processors (up to 32 cores). (B) Parallel speedup relative to a single core execution time.

5.4.2 GPU vs Multi-core CPU

CPU and GPU implementations were compared by means of elapsed time required to integrate the ODE systems associated with both tissue models. Fig. 5.28 shows the execution times for the ODE solvers. Clearly, the GPU achieved a better performance than the CPU (32 cores) in both models. In the simulation of the macro model, the GPU was 5 times faster than the CPU with 32 cores, which took about $10\,$s to execute, whereas on the GPU it took about $2\,$s to complete. Regarding the simulation with the microscopic model, where the solution of $2\,695\,299$ cells are required, a speedup factor of about 7-fold was achieved, i.e., the CPU took $132.18\,$s to integrate the systems of ODEs, whereas the GPU performed the same number of calculations within $20\,$s. If the execution times of the GPU are compared to only one of the eight Quad-Core AMD Opteron processors, i.e. considering 4 cores (Fig. 5.27 A), speedups of 67 times (macro model) and 53 times (micro model) are observed.
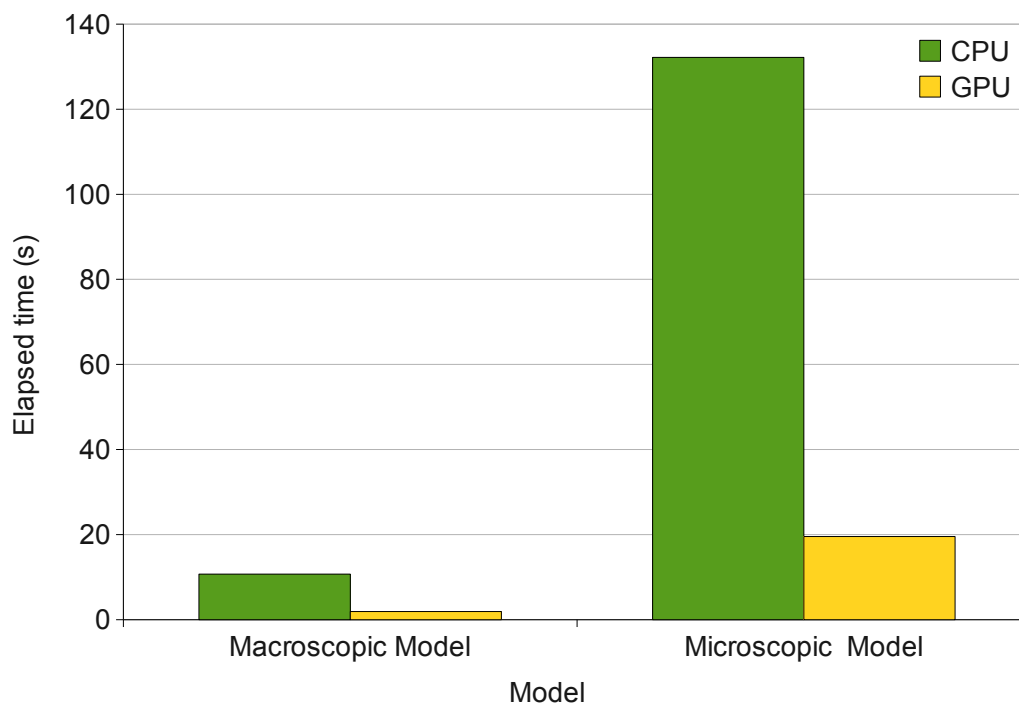
Figure 5.28: Total execution times required to solve n atrial cell models needed to simulate the macro ($n = 116\,048$) and micro ($n = 2\,695\,299$) models of the ROI using the multi-core CPU (32 cores) and GPU.

In order to check for possible deviations in the numerical solutions due to the use of single precision in the arithmetic operations, the results obtained using single precision were compared against one computed using double precision through the relative root-mean-square norm. The RRMS error produced was very small (less than 0.5%).

5.4.3 Discussion

Electrical activity at a cellular level in the heart is commonly modeled by systems of ODEs. The stiffness properties of these systems as well as the number of cell models required to build up a tissue mesh can dramatically affect the total computational work of a simulation. The performance of CPU and GPU solvers for the ODE systems describing the cellular dynamics in the atrial tissue models proposed in this thesis was evaluated. The classic Rush-Larsen method was considered for the integration of the ODEs and the performance was measured in terms of execution time (in seconds).

It was shown that, regardless the tissue model (macro or micro), the GPU performed better than a small CPU cluster (32 cores) during the integration of the ODE systems, where speedups of about 5-fold were obtained for the microscopic model. When compared to only one Quad-Core processor, astonishing speedups of more than 50-fold are observed. This represents the gain of a GPU costing \$ 100,00 over a still very powerful multi-core processor, which costs about \$ 400,00. Furthermore, the single precision used in the simulations did not influence the accuracy of numerical solutions. The presented results show that GPUs are a promising alternative to clusters of CPUs for simulating the electrical activity in the heart. The GPU allows to increase complexity and dimensions of the problem that can be modeled, and also represents a parallel system with high performance computing capabilities for relatively low costs in comparison to a cluster of CPUs needed to achieve the same performance.

5.4.4 Limitations

Important limitations of this work are: 1) the fact that only an atrial cell model was used to draw the conclusions, whereas many other models (from different regions of the heart) with different stiffness characteristics as well as number of ODEs are available in the literature; 2) there are more suitable solvers for stiff problems that may not scale well in GPU due to their complexities; 3) only the simulation of the equations associated to the atrial cellular dynamics were considered during the performance tests. However, not only the system of ODEs, but also the large systems of linear equations arising from the discretization of the monodomain/bidomain models are known to be computationally burdensome.[10, 26, 27]

Chapter 6

Conclusions and Outlook

During the course of this thesis, several aspects within the modeling of the electrical activity in the rabbit right atrial isthmus have been investigated:

A preliminary study was carried out aiming to assess the limitations of superfusion as a method to provide the tissue with proper oxygen supply and waste removal. Moreover, the impact of superfusion-induced heterogeneities (ischemia) occurring in the depth of the tissue upon signals measured on superficial layers was quantified. It has been shown that despite the numerous significant changes in electrophysiological properties, the extracellular potential field close to the surface of superfused preparations remains virtually unaffected. Depending on the question under study, superfused preparations have to be used with care, particularly with regard to repolarization. Despite some limitations, simulation results suggest that superfusion techniques are perfectly adequate when studying impulse propagation on thin-walled tissue preparations.

Subsequently, 2D models of the rabbit right atrial isthmus, the region of interest (ROI), accounting for functional as well as structural heterogeneities were established. These models were employed to simulate atrial activation sequences at the macroscopic (anatomy of the ROI) as well as at the microscopic scales. Conduction velocities computed in specific regions (pectinate muscles) were found to be in agreement with values obtained in experiments. The macroscopic model failed to reproduce electrogram fractionation. This was because changes in electrogram morphology were mainly caused by the presence of uncoupling structures (fibrosis and interstitial clefts) at the microscopic scale. The distribution of fractionated electrograms in pectinate muscles was similar to the distribution obtained in experiments. Electrogram morphology was also shown to change according to the direction of the electrical wavefront. Computed CNFs were able to provide information about the direction of the wavefront depending on the tissue microstructure.

Furthermore, a circumferential stimulation protocol was designed and employed in simulations with the microscopic model in order to characterize electrically the under-

lying tissue microstructure. The findings support the hypothesis that microstructural organization of fibrosis and the direction of the electrical wavefront are linked to CFAEs. Changes in electrogram morphology suggest that changing the site of stimulus allows to distinguish among different types of fractionation patterns of propagation, namely those arising from uncoupling structures oriented parallel to the cardiac fibers from others associated with multidirectional arrangement of uncoupling structures. Electrogram fractionation and amplitude were shown to be useful measurements to characterize spatial organization of microfibrosis. The ability of distinguishing among different types of microfibrosis represents an important step towards understanding the mechanisms behind AF.

Finally, a solver to accelerate the simulations of cellular dynamics in the atrial models proposed in this thesis was designed to run onto the graphical processing units (GPUs). Performance tests demonstrated that the GPU implementation runs about 50 times faster than a parallel CPU implementation running with 4 threads on a quad-core machine.

The resultant models reconstruct, at different levels of detail, the complex electrical activation in the rabbit right atrial isthmus. In particular, the microscopic models proposed in this thesis distinguish themselves from other atrial models known in the literature due to the spatial resolution ($\sim 10\,\mu$m) achieved through the use of histological images. To the best of our knowledge, these models are the first to be used to study the relation between realistic tissue structures at the microscopic scale. It was also shown that newer graphic-hardware is a fast and cheap alternative to cluster of computers to accelerate the simulations of cellular dynamics in cardiac tissue models. In conclusion, there are still numerous open questions concerning conduction inhomogeneities and isthmus-related arrhythmias. Computational modeling has been proven an indispensable complement to experimental studies over the past decades. Therefore, this thesis has advanced the state-of-the-art and helped to push forward the knowledge of conduction in the ROI. The associated increase in model complexity is one of many steps towards the clinical use of diagnostic tools of arrhythmia analysis for future minimal-invasive catheter techniques.

6.1 Future Work

Computer simulations performed with the high-resolution tissue models developed in this thesis could also be combined with future experimental measurements to get a better understanding towards structural mechanisms of atrial conduction in healthy as well as in diseased hearts. The models proposed serve as a starting point for future investigation of the following aspects.

6.1.1   Structure- and Age-Related Atrial Arrhythmias

Experimentally, age-related conduction behavior can be quantified through analysis of signals measured in the ROI from young, adult and aged animals. Extracellulary measured potentials combined with histological examinations performed *post experimentum* can provide information of how connective tissue in the old specimen has altered the network of coupled myocytes. The framework presented in this thesis would be an ideal complement to such experimental study. It would represent a first approach to establish structure-related computer models of the ROI allowing *in silico* studies of how aging affects the formation of AF and AFL.

6.1.2   Improvement of Catheter Ablation Procedures

The simulation results presented showed that electrode arrays capable of measuring and stimulating in multiple locations could be useful tools to obtain information about the tissue microstructure. The findings suggest a continuative experimental study to evaluate the feasibility of a sensor with such electrodes *in vitro* (in progress at the Medical University of Graz). If proven feasible, the sensor could be built in a catheter allowing clinicians to identify and characterize areas of fibrotic tissue during ablation procedures. Modeling studies could then be carried out to elucidate whether the presence of CFAEs represents legitimate targets for catheter ablation.

6.1.3   Ectopic Foci and Atrial Fibrosis

The mechanisms behind cardiac arrhythmias can be divided into those due to abnormalities of either impulse formation or impulse conduction.[146] During the course of this thesis, only fibrosis as a substrate of slow impulse conduction was studied. However, a common mechanism, believed to underlie a variety of arrhythmias in the first category, is the presence of ectopic focal excitations in the heart. Many experimental studies have shown that abnormal calcium (Ca) cycling, at the single cell level, plays an essential role in the formation of these focal excitations.[147] Ca cycling occurs when voltage sensitive L-type Ca channels on the cell membrane trigger Ca sensitive Ryanodine receptor channels, which control the flow of Ca through the sarcoplasmic reticulum (SR). However, Ca can be released from the SR independently due to Ryanodine receptor fluctuations.[147] This efflux of Ca, referred to as spontaneous Ca release (SCR), can be arrhythmogenic because Ca released into the cytosol will stimulate Ca-sensitive membrane currents, such as the sodium-calcium exchanger I_{NaCa}, which can induce sufficient inward current to form delayed after-depolarizations (DADs). In cardiac tissue these events can summate to trigger ill-timed ectopic beats, leading to arrhythmogenic triggered activity.[148] Nevertheless, for an ectopic beat to propagate, the source (cells eliciting DADs) current density

must be sufficient to bring the sink (quiescent cells) to its activation threshold. Reduction in tissue coupling as a result of structural remodeling (either reduced gap-junction coupling or fibrosis) has been shown to modulate local source-sink mismatches, promoting the propagation of DADs.[148] The computational framework presented here could also be used to explore how atrial fibrosis influences the properties of Ca-mediated ectopic foci. In particular, whether the spatial distribution of fibrosis can dictate the location and morphology of ectopic foci.

Bibliography

1. A. C. Guyton and J. E. Hall, *Textbook of Medical Physiology (10 Edition)*. Saunders, 2000.

2. S. Nattel, "New ideas about atrial fibrillation 50 years on." *Nature*, vol. 415, no. 6868, pp. 219–26, 2002.

3. E. Hofer, D. Sanchez-Quintana, G. Plank, and M. Tischler, "Normal and fractionated cardiac near fields and their relation to microstructure - an experimental approach." *Conf Proc IEEE Eng Med Biol Soc*, vol. 1, pp. 51–54, 2003.

4. O. V. Aslanidi, M. R. Boyett, H. Dobrzynski, J. Li, and H. Zhang, "Mechanisms of transition from normal to reentrant electrical activity in a model of rabbit atrial tissue: interaction of tissue heterogeneity and anisotropy." *Biophys J*, vol. 96, no. 3, pp. 798–817, 2009.

5. M. S. Spach and J. M. Kootsey, "Relating the sodium current and conductance to the shape of transmembrane and extracellular potentials by simulation: effects of propagation boundaries." *IEEE Trans Biomed Eng*, vol. 32, no. 10, pp. 743–55, 1985.

6. J. M. de Bakker and F. H. Wittkampf, "The pathophysiologic basis of fractionated and complex electrograms and the impact of recording techniques on their detection and interpretation." *Circ Arrhythm Electrophysiol*, vol. 3, no. 2, pp. 204–13, 2010.

7. S. de Jong, T. A. van Veen, H. V. van Rijen, and J. M. de Bakker, "Fibrosis and cardiac arrhythmias." *J Cardiovasc Pharmacol*, vol. 57, no. 6, pp. 630–8, 2011.

8. R. Plonsey and R. C. Barr, *Bioelectricity: A Quantitative Approach (3rd Edition)*. Springer, 1998.

9. A. L. Hodgkin and A. F. Huxley, "A quantitative description of membrane current and its application to conduction and excitation in nerve." *J Physiol*, vol. 117, no. 4, pp. 500–44, 1952.

10. E. J. Vigmond, R. Weber dos Santos, A. J. Prassl, M. Deo, and G. Plank, "Solvers for the cardiac bidomain equations." *Prog Biophys Mol Biol*, vol. 96, no. 1-3, pp. 3–18, 2008.

11. F. O. Campos, T. Wiener, A. J. Prassl, H. Ahammer, G. Plank, R. Weber dos Santos, D. Sánchez-Quintana, and E. Hofer, "A 2D-computer model of atrial tissue based on histographs describes the electro-anatomical impact of microstructure on endocardiac potentials and electric near-fields." in *Conf Proc IEEE Eng Med Biol Soc*, vol. 1, 2010, pp. 2541–4.

12. B. M. Rocha, F. O. Campos, R. M. Amorim, G. Plank, R. W. dos Santos, M. Liebmann, and G. Haase, "Accelerating cardiac excitation spread simulations using graphics processing units." *Concurrency Computat.: Pract. Exper.*, vol. 23, pp. 708–720, 2010.

13. W. M. Feinberg, J. L. Blackshear, A. Laupacis, R. Kronmal, and R. G. Hart, "Prevalence, age distribution, and gender of patients with atrial fibrillation. Analysis and implications." *Arch Intern Med*, vol. 155, no. 5, pp. 469–73, 1995.

14. M. Gottwald, E. Gottwald, and S. Dhein, "Age-related electrophysiological and histological changes in rabbit hearts: age-related changes in electrophysiology." *Int J Cardiol*, vol. 62, no. 2, pp. 97–106, 1997.

15. L. Protas, R. V. Oren, C. E. Clancy, and R. B. Robinson, "Age-dependent changes in Na current magnitude and TTX-sensitivity in the canine sinoatrial node." *J Mol Cell Cardiol*, vol. 48, no. 1, pp. 172–80, 2010.

16. M. S. Spach, J. F. Heidlage, P. C. Dolber, and R. C. Barr, "Mechanism of origin of conduction disturbances in aging human atrial bundles: experimental and model study." *Heart Rhythm*, vol. 4, no. 2, pp. 175–85, 2007.

17. K. Nademanee, J. McKenzie, E. Kosar, M. Schwab, B. Sunsaneewitayakul, T. Vasavakul, C. Khunnawat, and T. Ngarmukos, "A new approach for catheter ablation of atrial fibrillation: mapping of the electrophysiologic substrate." *J Am Coll Cardiol*, vol. 43, no. 11, pp. 2044–53, 2004.

18. K. Nademanee, M. C. Schwab, E. M. Kosar, M. Karwecki, M. D. Moran, N. Visessook, A. D. Michael, and T. Ngarmukos, "Clinical outcomes of catheter substrate ablation for high-risk patients with atrial fibrillation." *J Am Coll Cardiol*, vol. 51, no. 8, pp. 843–9, 2008.

19. D. Sanchez-Quintana, R. H. Anderson, J. A. Cabrera, V. Climent, R. Martin, J. Farre, and S. Y. Ho, "The terminal crest: morphological features relevant to electrophysiology." *Heart*, vol. 88, no. 4, pp. 406–11, 2002.

20. T. R. Betts, S. Y. Ho, D. Sanchez-Quintana, P. R. Roberts, R. H. Anderson, and J. M. Morgan, "Three-dimensional mapping of right atrial activation during sinus rhythm and its relationship to endocardial architecture." *J Cardiovasc Electrophysiol*, vol. 13, no. 11, pp. 1152–9, 2002.

21. J. A. Cabrera, D. Sanchez-Quintana, J. Farre, J. M. Rubio, and S. Y. Ho, "The inferior right atrial isthmus: further architectural insights for current and coming ablation technologies." *J Cardiovasc Electrophysiol*, vol. 16, no. 4, pp. 402–8, 2005.

22. E. Hofer, F. Keplinger, T. Thurner, T. Wiener, D. Sanchez-Quintana, V. Climent, and G. Plank, "A new floating sensor array to detect electric near fields of beating heart preparations." *Biosens Bioelectron*, vol. 21, no. 12, pp. 2232–9, 2006.

23. R. A. Burton, G. Plank, J. E. Schneider, V. Grau, H. Ahammer, S. L. Keeling, J. Lee, N. P. Smith, D. Gavaghan, N. Trayanova, and P. Kohl, "Three-dimensional models of individual cardiac histoanatomy: tools and challenges." *Ann N Y Acad Sci*, vol. 1080, pp. 301–19, 2006.

24. V. Jacquemet and C. S. Henriquez, "Genesis of complex fractionated atrial electrograms in zones of slow conduction: a computer model of microfibrosis." *Heart Rhythm*, vol. 6, no. 6, pp. 803–10, 2009.

25. K. Tanaka, S. Zlochiver, K. L. Vikstrom, M. Yamazaki, J. Moreno, M. Klos, A. V. Zaitsev, R. Vaidyanathan, D. S. Auerbach, S. Landas, G. Guiraudon, J. Jalife, O. Berenfeld, and J. Kalifa, "Spatial distribution of fibrosis governs fibrillation wave dynamics in the posterior left atrium during heart failure." *Circ Res*, vol. 101, no. 8, pp. 839–47, 2007.

26. G. Plank, M. Liebmann, R. Weber dos Santos, E. J. Vigmond, and G. Haase, "Algebraic multigrid preconditioner for the cardiac bidomain model." *IEEE Trans Biomed Eng*, vol. 54, no. 4, pp. 585–96, 2007.

27. R. Weber dos Santos, G. Plank, S. Bauer, and E. J. Vigmond, "Parallel multigrid preconditioner for the cardiac bidomain model." *IEEE Trans Biomed Eng*, vol. 51, no. 11, pp. 1960–8, 2004.

28. D. Bers, *Excitation-Contraction Coupling and Cardiac Contractile Force (2nd Edition)*. Springer, 2001.

29. S. Nattel, "Experimental evidence for proarrhythmic mechanisms of antiarrhythmic drugs." *Cardiovasc Res*, vol. 37, no. 3, pp. 567–77, 1998.

30. A. S. Go, E. M. Hylek, K. A. Phillips, Y. Chang, L. E. Henault, J. V. Selby, and D. E. Singer, "Prevalence of diagnosed atrial fibrillation in adults: national implications for rhythm management and stroke prevention: the AnTicoagulation and Risk Factors in Atrial Fibrillation (ATRIA) Study." *JAMA*, vol. 285, no. 18, pp. 2370–5, 2001.

31. J. B. Morton, P. Sanders, A. Das, J. K. Vohra, P. B. Sparks, and J. M. Kalman, "Focal atrial tachycardia arising from the tricuspid annulus: electrophysiologic and electrocardiographic characteristics." *J Cardiovasc Electrophysiol*, vol. 12, no. 6, pp. 653–9, 2001.

32. J. Keener and J. Sneyd, *Mathematical Physiology.* Springer, 1998.

33. R. W. Dos Santos, F. Otaviano Campos, L. Neumann Ciuffo, A. Nygren, W. Giles, and H. Koch, "ATX-II effects on the apparent location of M cells in a computational model of a human left ventricular wedge." *J Cardiovasc Electrophysiol*, vol. 17 Suppl 1, pp. S86–S95, 2006.

34. D. Fedida and W. R. Giles, "Regional variations in action potentials and transient outward current in myocytes isolated from rabbit left ventricle." *J Physiol*, vol. 442, pp. 191–209, 1991.

35. R. Weber dos Santos, A. Nygren, F. Otaviano Campos, H. Koch, and W. R. Giles, "Experimental and theoretical ventricular electrograms and their relation to electrophysiological gradients in the adult rat heart." *Am J Physiol Heart Circ Physiol*, vol. 297, no. 4, pp. H1521–34, 2009.

36. M. R. Boyett, H. Honjo, M. Yamamoto, M. R. Nikmaram, R. Niwa, and I. Kodama, "Downward gradient in action potential duration along conduction path in and around the sinoatrial node." *Am J Physiol*, vol. 276, no. 2 Pt 2, pp. H686–98, 1999.

37. A. Qi, J. A. Yeung-Lai-Wah, J. Xiao, and C. R. Kerr, "Regional differences in rabbit atrial repolarization: importance of transient outward current." *Am J Physiol*, vol. 266, no. 2 Pt 2, pp. H643–9, 1994.

38. T. Yamashita, T. Nakajima, H. Hazama, E. Hamada, Y. Murakawa, K. Sawada, and M. Omata, "Regional differences in transient outward current density and inhomogeneities of repolarization in rabbit right atrium." *Circulation*, vol. 92, no. 10, pp. 3061–9, 1995.

39. J. Feng, L. Yue, Z. Wang, and S. Nattel, "Ionic mechanisms of regional action potential heterogeneity in the canine right atrium." *Circ Res*, vol. 83, no. 5, pp. 541–51, 1998.

40. S. Y. Ho, R. H. Anderson, and D. Sanchez-Quintana, "Atrial structure and fibres: morphologic bases of atrial conduction." *Cardiovasc Res*, vol. 54, no. 2, pp. 325–36, 2002.

41. T. Yamashita, H. Inoue, A. Nozaki, and T. Sugimoto, "Role of anatomic architecture in sustained atrial reentry and double potentials." *Am Heart J*, vol. 124, no. 4, pp. 938–46, 1992.

42. J. M. Kalman, J. E. Olgin, M. R. Karch, M. Hamdan, R. J. Lee, and M. D. Lesh, ""Cristal tachycardias": origin of right atrial tachycardias from the crista terminalis identified by intracardiac echocardiography." *J Am Coll Cardiol*, vol. 31, no. 2, pp. 451–9, 1998.

43. M. S. Spach and J. F. Heidlage, "The stochastic nature of cardiac propagation at a microscopic level. Electrical description of myocardial architecture and its application to conduction." *Circ Res*, vol. 76, no. 3, pp. 366–80, 1995.

44. A. G. Kléber and Y. Rudy, "Basic mechanisms of cardiac impulse propagation and associated arrhythmias." *Physiol Rev*, vol. 84, no. 2, pp. 431–88, 2004.

45. F. B. Sachse, *Computational Cardiology.* Springer, 2004.

46. R. J. Schilling, N. S. Peters, and D. W. Davies, "Simultaneous endocardial mapping in the human left ventricle using a noncontact catheter: comparison of contact and reconstructed electrograms during sinus rhythm." *Circulation*, vol. 98, no. 9, pp. 887–98, 1998.

47. M. S. Spach, W. T. Miller, 3rd, P. C. Dolber, J. M. Kootsey, J. R. Sommer, and C. E. Mosher, Jr, "The functional role of structural complexities in the propagation of depolarization in the atrium of the dog. Cardiac conduction disturbances due to discontinuities of effective axial resistivity." *Circ Res*, vol. 50, no. 2, pp. 175–91, 1982.

48. J. M. de Bakker and H. M. van Rijen, "Continuous and discontinuous propagation in heart muscle." *J Cardiovasc Electrophysiol*, vol. 17, no. 5, pp. 567–73, 2006.

49. S. Sato, M. Ashraf, R. W. Millard, H. Fujiwara, and A. Schwartz, "Connective tissue changes in early ischemia of porcine myocardium: an ultrastructural study." *J Mol Cell Cardiol*, vol. 15, no. 4, pp. 261–75, 1983.

50. P. Whittaker, D. R. Boughner, and R. A. Kloner, "Role of collagen in acute myocardial infarct expansion." *Circulation*, vol. 84, no. 5, pp. 2123–34, 1991.

51. J. P. Boineau, C. B. Miller, R. B. Schuessler, W. R. Roeske, L. J. Autry, A. C. Wylds, and D. A. Hill, "Activation sequence and potential distribution maps demonstrating multicentric atrial impulse origin in dogs." *Circ Res*, vol. 54, no. 3, pp. 332–47, 1984.

52. G. Plank and E. Hofer, "Model study of vector-loop morphology during electrical mapping of microscopic conduction in cardiac tissue." *Ann Biomed Eng*, vol. 28, no. 10, pp. 1244–52, 2000.

53. A. Bussek, E. Wettwer, T. Christ, H. Lohmann, P. Camelliti, and U. Ravens, "Tissue slices from adult mammalian hearts as a model for pharmacological drug testing." *Cell Physiol Biochem*, vol. 24, no. 5-6, pp. 527–36, 2009.

54. J. Kockskamper, D. von Lewinski, M. Khafaga, A. Elgner, M. Grimm, T. Eschenhagen, P. A. Gottlieb, F. Sachs, and B. Pieske, "The slow force response to stretch in atrial and ventricular myocardium from human heart: functional relevance and subcellular mechanisms." *Prog Biophys Mol Biol*, vol. 97, no. 2-3, pp. 250–67, 2008.

55. D. H. Lau, L. Mackenzie, N. J. Shipp, P. Kuklik, H. Dimitri, B. L. Lobb, M. Alasady, H. S. Lim, D. R. Kelly, A. G. Brooks, D. A. Saint, and P. Sanders, "Feasibility of high-density electrophysiological study using multiple-electrode array in isolated small animal atria." *Clin Exp Pharmacol Physiol*, vol. 37, no. 10, pp. 1023–7, 2010.

56. S. Sicouri, B. Gianetti, A. C. Zygmunt, J. M. Cordeiro, and C. Antzelevitch, "Antiarrhythmic effects of simvastatin in canine pulmonary vein sleeve preparations." *J Am Coll Cardiol*, vol. 57, no. 8, pp. 986–93, 2011.

57. H. G. Zimmer, "The isolated perfused heart and its pioneers." *News Physiol Sci*, vol. 13, pp. 203–210, 1998.

58. W. J. Hucker, V. Sharma, V. P. Nikolski, and I. R. Efimov, "Atrioventricular conduction with and without AV nodal delay: two pathways to the bundle of His in the rabbit heart." *Am J Physiol Heart Circ Physiol*, vol. 293, no. 2, pp. H1122–30, 2007.

59. S. Lemoine, P. E. Puddu, C. Durand, O. Lepage, G. Babatasi, C. Ivascau, M. Massetti, J. L. Gerard, and J. L. Hanouz, "Signaling pathways involved in postconditioning-induced cardioprotection of human myocardium, in vitro." *Exp Biol Med (Maywood)*, vol. 235, no. 6, pp. 768–76, 2010.

60. C. J. Barclay, "Modelling diffusive O(2) supply to isolated preparations of mammalian skeletal and cardiac muscle." *J Muscle Res Cell Motil*, vol. 26, no. 4-5, pp. 225–35, 2005.

61. N. F. Paradise, J. L. Schmitter, and J. M. Surmitis, "Criteria for adequate oxygenation of isometric kitten papillary muscle." *Am J Physiol*, vol. 241, no. 3, pp. H348–53, 1981.

62. S. Raman, M. A. Kelley, and P. M. Janssen, "Effect of muscle dimensions on trabecular contractile performance under physiological conditions." *Pflugers Arch*, vol. 451, no. 5, pp. 625–30, 2006.

63. C. B. Riegger, G. Alperovich, and A. G. Kléber, "Effect of oxygen withdrawal on active and passive electrical properties of arterially perfused rabbit ventricular muscle." *Circ Res*, vol. 64, no. 3, pp. 532–41, 1989.

64. A. J. Prassl, F. Kickinger, H. Ahammer, V. Grau, J. E. Schneider, E. Hofer, E. J. Vigmond, N. A. Trayanova, and G. Plank, "Automatically generated, anatomically accurate meshes for cardiac electrophysiology problems." *IEEE Trans Biomed Eng*, vol. 56, no. 5, pp. 1318–30, 2009.

65. G. Plank, R. A. Burton, P. Hales, M. Bishop, T. Mansoori, M. O. Bernabeu, A. Garny, A. J. Prassl, C. Bollensdorff, F. Mason, F. Mahmood, B. Rodriguez, V. Grau, J. E. Schneider, D. Gavaghan, and P. Kohl, "Generation of histo-anatomically representative models of the individual heart: tools and application." *Philos Transact A Math Phys Eng Sci*, vol. 367, no. 1896, pp. 2257–92, 2009.

66. G. Plank, L. Zhou, J. L. Greenstein, S. Cortassa, R. L. Winslow, B. O'Rourke, and N. A. Trayanova, "From mitochondrial ion channels to arrhythmias in the heart: computational techniques to bridge the spatio-temporal scales." *Philos Transact A Math Phys Eng Sci*, vol. 366, no. 1879, pp. 3381–409, 2008.

67. R. Weber dos Santos, U. Steinhoff, E. Hofer, D. Sánchez-Quintana, and H. Koch, "Modelling the electrical propagation in cardiac tissue using detailed histological data," *Biomedizinische Technik. Biomedical Engineering*, vol. 48, p. 476â479, 2003.

68. R. Killmann, P. Wach, and F. Dienstl, "Three-dimensional computer model of the entire human heart for simulation of reentry and tachycardia: gap phenomenon and Wolff-Parkinson-White syndrome." *Basic Res Cardiol*, vol. 86, no. 5, pp. 485–501, 1991.

69. N. Virag, J. M. Vesin, and L. Kappenberger, "A computer model of cardiac electrical activity for the simulation of arrhythmias." *Pacing Clin Electrophysiol*, vol. 21, no. 11 Pt 2, pp. 2366–71, 1998.

70. D. Harrild and C. Henriquez, "A computer model of normal conduction in the human atria." *Circ Res*, vol. 87, no. 7, pp. E25–36, 2000.

71. E. J. Vigmond, R. Ruckdeschel, and N. Trayanova, "Reentry in a morphologically realistic atrial model." *Cardiovasc Electrophysiol*, vol. 12, pp. 1046–1054, 2001.

72. G. Seemann, C. Hoper, F. B. Sachse, O. Dossel, A. V. Holden, and H. Zhang, "Heterogeneous three-dimensional anatomical and electrophysiological model of human atria." *Philos Transact A Math Phys Eng Sci*, vol. 364, no. 1843, pp. 1465–81, 2006.

73. J. Zhao, M. L. Trew, I. J. Legrice, B. H. Smaill, and A. J. Pullan, "A tissue-specific model of reentry in the right atrial appendage." *J Cardiovasc Electrophysiol*, vol. 20, no. 6, pp. 675–84, 2009.

74. R. Plonsey and R. C. Barr, "Mathematical modeling of electrical activity of the heart." *J Electrocardiol*, vol. 20, no. 3, pp. 219–26, 1987.

75. C. M. Armstrong and F. Bezanilla, "Inactivation of the sodium channel. II. Gating current experiments." *J Gen Physiol.*, vol. 70, no. 5, pp. 567–590, 1977.

76. R. W. Aldrich, D. P. Corey, and C. F. Stevens, "A reinterpretation of mammalian sodium channel gating based on single channel recording." *Nature*, vol. 306, no. 5942, pp. 436–441, 1983.

77. C. Clancy and Y. Rudy, "Linking a genetic defect to its cellular phenotype in a cardiac arrhythmia." *Nature*, vol. 400, no. 6744, pp. 566–569, 1999.

78. V. E. Bondarenko, G. P. Szigeti, G. C. Bett, S. J. Kim, and R. L. Rasmusson, "Computer model of action potential of mouse ventricular myocytes." *Am J Physiol Heart Circ Physiol.*, vol. 287, no. 3, pp. H1378–403, 2004.

79. A. Mahajan, Y. Shiferaw, D. Sato, A. Baher, R. Olcese, L. H. Xie, M. J. Yang, P. S. Chen, J. G. Restrepo, A. Karma, A. Garfinkel, Z. Qu, and J. N. Weiss, "A rabbit ventricular action potential model replicating cardiac dynamics at rapid heart rates." *Biophys J*, vol. 94, no. 2, pp. 392–410, 2008.

80. G. W. Beeler and H. Reuter, "Reconstruction of the action potential of ventricular myocardial fibres." *J Physiol*, vol. 268, no. 1, pp. 177–210, 1977.

81. S. S. Demir, J. W. Clark, C. R. Murphey, and W. R. Giles, "A mathematical model of a rabbit sinoatrial node cell." *Am J Physiol*, vol. 266, no. 3 Pt 1, pp. C832–52, 1994.

82. D. DiFrancesco and D. Noble, "A model of cardiac electrical activity incorporating ionic pumps and concentration changes." *Philos Trans R Soc Lond B Biol Sci*, vol. 307, no. 1133, pp. 353–98, 1985.

83. D. S. Lindblad, C. R. Murphey, J. W. Clark, and W. R. Giles, "A model of the action potential and underlying membrane currents in a rabbit atrial cell." *Am J Physiol*, vol. 271, no. 4, pp. H1666–96, 1996.

84. C. H. Luo and Y. Rudy, "A dynamic model of the cardiac ventricular action potential. I. Simulations of ionic currents and concentration changes." *Circ Res*, vol. 74, no. 6, pp. 1071–96, 1994.

85. A. Nygren, C. Fiset, L. Firek, J. W. Clark, D. S. Lindblad, R. B. Clark, and W. R. Giles, "Mathematical model of an adult human atrial cell: the role of K+ currents in repolarization." *Circ Res*, vol. 82, no. 1, pp. 63–81, 1998.

86. B. Hille, *Ion Channels of Excitable Membranes (3rd Edition)*. Sinauer Associates, 2001.

87. D. B. Geselowitz and W. T. Miller, 3rd, "A bidomain model for anisotropic cardiac muscle." *Ann Biomed Eng*, vol. 11, no. 3-4, pp. 191–206, 1983.

88. H. Dobrzynski, J. Li, J. Tellez, I. D. Greener, V. P. Nikolski, S. E. Wright, S. H. Parson, S. A. Jones, M. K. Lancaster, M. Yamamoto, H. Honjo, Y. Takagishi, I. Kodama, I. R. Efimov, R. Billeter, and M. R. Boyett, "Computer three-dimensional reconstruction of the sinoatrial node." *Circulation*, vol. 111, no. 7, pp. 846–54, 2005.

89. J. Sundnes, G. T. Lines, and A. Tveito, "An operator splitting method for solving the bidomain equations coupled to a volume conductor model for the torso." *Math Biosci*, vol. 194, no. 2, pp. 233–48, 2005.

90. A. E. Pollard, N. Hooke, and C. S. Henriquez, "Cardiac propagation simulation." *Crit Rev Biomed Eng*, vol. 20, no. 3-4, pp. 171–210, 1992.

91. J. Sundnes, B. F. Nielsen, K. A. Mardal, X. Cai, G. T. Lines, and A. Tveito, "On the computational complexity of the bidomain and the monodomain models of electrophysiology." *Ann Biomed Eng*, vol. 34, no. 7, pp. 1088–97, 2006.

92. J. Clark and R. Plonsey, "A mathematical evaluation of the core conductor model." *Biophys J*, vol. 6, no. 1, pp. 95–112, 1966.

93. M. J. Bishop and G. Plank, "Representing Cardiac Bidomain Bath-loading Effects by an Augmented Monodomain Approach: Application to Complex Ventricular Models." *IEEE Trans Biomed Eng*, vol. 58, no. 4, pp. 1066–75, 2011.

94. W. J. Karlon, J. W. Covell, A. D. McCulloch, J. J. Hunter, and J. H. Omens, "Automated measurement of myofiber disarray in transgenic mice with ventricular expression of ras." *Anat Rec*, vol. 252, no. 4, pp. 612–25, 1998.

95. M. J. Bishop, G. Plank, R. A. Burton, J. E. Schneider, D. J. Gavaghan, V. Grau, and P. Kohl, "Development of an anatomically detailed MRI-derived rabbit ventricular model and assessment of its impact on simulations of electrophysiological function." *Am J Physiol Heart Circ Physiol*, vol. 298, no. 2, pp. H699–718, 2010.

96. M. J. Bishop, P. M. Boyle, G. Plank, D. G. Welsh, and E. J. Vigmond, "Modeling the role of the coronary vasculature during external field stimulation." *IEEE Trans Biomed Eng*, vol. 57, no. 10, pp. 2335–45, 2010.

97. W. J. Karlon, P. P. Hsu, S. Li, S. Chien, A. D. McCulloch, and J. H. Omens, "Measurement of orientation and distribution of cellular alignment and cytoskeletal organization." *Ann Biomed Eng*, vol. 27, no. 6, pp. 712–20, 1999.

98. S. Niederer, L. Mitchell, N. Smith, and G. Plank, "Simulating human cardiac electrophysiology on clinical time-scales." *Front Physiol*, vol. 2, p. 14, 2011.

99. A. E. Pollard, W. E. Cascio, V. G. Fast, and S. B. Knisley, "Modulation of triggered activity by uncoupling in the ischemic border. A model study with phase 1b-like conditions." *Cardiovasc Res*, vol. 56, no. 3, pp. 381–92, 2002.

100. R. M. Shaw and Y. Rudy, "Electrophysiologic effects of acute myocardial ischemia: a theoretical study of altered cell excitability and action potential duration." *Cardiovasc Res*, vol. 35, no. 2, pp. 256–72, 1997.

101. D. L. Weiss, M. Ifland, F. B. Sachse, G. Seemann, and O. Dossel, "Modeling of cardiac ischemia in human myocytes and tissue including spatiotemporal electrophysiological variations." *Biomed Tech (Berl)*, vol. 54, no. 3, pp. 107–25, 2009.

102. J. R. de Groot and R. Coronel, "Acute ischemia-induced gap junctional uncoupling and arrhythmogenesis." *Cardiovasc Res*, vol. 62, no. 2, pp. 323–34, 2004.

103. B. Rodriguez, J. M. Ferrero, Jr, and B. Trenor, "Mechanistic investigation of extracellular K+ accumulation during acute myocardial ischemia: a simulation study." *Am J Physiol Heart Circ Physiol*, vol. 283, no. 2, pp. H490–500, 2002.

104. O. Bernus, C. W. Zemlin, R. M. Zaritsky, S. F. Mironov, and A. M. Pertsov, "Alternating conduction in the ischaemic border zone as precursor of reentrant arrhythmias: a simulation study." *Europace*, vol. 7 Suppl 2, pp. 93–104, 2005.

105. J. M. Ferrero, Jr, J. Saiz, J. M. Ferrero, and N. V. Thakor, "Simulation of action potentials from metabolically impaired cardiac myocytes. Role of ATP-sensitive K+ current." *Circ Res*, vol. 79, no. 2, pp. 208–21, 1996.

106. M. M. Bersohn, "Sodium pump inhibition in sarcolemma from ischemic hearts." *J Mol Cell Cardiol*, vol. 27, no. 8, pp. 1483–9, 1995.

107. E. Carmeliet, "Cardiac ionic currents and acute ischemia: from channels to arrhythmias." *Physiol Rev*, vol. 79, no. 3, pp. 917–1017, 1999.

108. A. E. Doering and W. J. Lederer, "The mechanism by which cytoplasmic protons inhibit the sodium-calcium exchanger in guinea-pig heart cells." *J Physiol*, vol. 466, pp. 481–99, 1993.

109. C. R. Malloy, D. C. Buster, M. M. Castro, C. F. Geraldes, F. M. Jeffrey, and A. D. Sherry, "Influence of global ischemia on intracellular sodium in the perfused rat heart." *Magn Reson Med*, vol. 15, no. 1, pp. 33–44, 1990.

110. A. G. Kléber, C. B. Riegger, and M. J. Janse, "Electrical uncoupling and increase of extracellular resistance after induction of ischemia in isolated, arterially perfused rabbit papillary muscle." *Circ Res*, vol. 61, no. 2, pp. 271–9, 1987.

111. J. Tranum-Jensen, M. J. Janse, W. T. Fiolet, W. J. Krieger, C. N. D'Alnoncourt, and D. Durrer, "Tissue osmolality, cell swelling, and reperfusion in acute regional myocardial ischemia in the isolated porcine heart." *Circ Res*, vol. 49, no. 2, pp. 364–81, 1981.

112. J. G. Stinstra, S. Shome, B. Hopenfeld, and R. S. MacLeod, "Modelling passive cardiac conductivity during ischaemia." *Med Biol Eng Comput*, vol. 43, no. 6, pp. 776–82, 2005.

113. W. E. Cascio, G. X. Yan, and A. G. Kléber, "Passive electrical properties, mechanical activity, and extracellular potassium in arterially perfused and ischemic rabbit ventricular muscle. Effects of calcium entry blockade or hypocalcemia." *Circ Res*, vol. 66, no. 6, pp. 1461–73, 1990.

114. Z. G. Guo, R. Levi, L. M. Aaronson, and W. A. Gay, "The isolated human pectinate muscle: a reliable preparation of human cardiac tissue." *J Pharmacol Methods*, vol. 9, no. 2, pp. 127–35, 1983.

115. A. G. Kléber and C. B. Riegger, "Electrical constants of arterially perfused rabbit papillary muscle." *J Physiol*, vol. 385, pp. 307–24, 1987.

116. H. L. Tan and M. J. Janse, "Contribution of mechanical activity and electrical activity to cellular electrical uncoupling in ischemic rabbit papillary muscle." *J Mol Cell Cardiol*, vol. 26, no. 6, pp. 733–42, 1994.

117. H. L. Tan, P. Mazon, H. J. Verberne, M. E. Sleeswijk, R. Coronel, T. Opthof, and M. J. Janse, "Ischaemic preconditioning delays ischaemia induced cellular electrical uncoupling in rabbit myocardium by activation of ATP sensitive potassium channels." *Cardiovasc Res*, vol. 27, no. 4, pp. 644–51, 1993.

118. F. B. Sachse, B. W. Steadman, J. H. B Bridge, B. B. Punske, and B. Taccardi, "Conduction velocity in myocardium modulated by strain: measurement instrumentation and initial results." *Conf Proc IEEE Eng Med Biol Soc*, vol. 5, pp. 3593–6, 2004.

119. R. Coronel, J. W. Fiolet, F. J. Wilms-Schopman, A. F. Schaapherder, T. A. Johnson, L. S. Gettes, and M. J. Janse, "Distribution of extracellular potassium and its relation to electrophysiologic changes during acute myocardial ischemia in the isolated perfused porcine heart." *Circulation*, vol. 77, no. 5, pp. 1125–38, 1988.

120. A. F. Schaapherder, C. A. Schumacher, R. Coronel, and J. W. Fiolet, "Transmural inhomogeneity of extracellular [K+] and pH and myocardial energy metabolism in the isolated rat heart during acute global ischemia; dependence on gaseous environment." *Basic Res Cardiol*, vol. 85, no. 1, pp. 33–44, 1990.

121. R. L. Wilensky, J. Tranum-Jensen, R. Coronel, A. A. Wilde, J. W. Fiolet, and M. J. Janse, "The subendocardial border zone during acute ischemia of the rabbit heart: an electrophysiologic, metabolic, and morphologic correlative study." *Circulation*, vol. 74, no. 5, pp. 1137–46, 1986.

122. B. Rodriguez, N. Trayanova, and D. Noble, "Modeling cardiac ischemia." *Ann N Y Acad Sci*, vol. 1080, pp. 395–414, 2006.

123. J. M. de Bakker, F. J. van Capelle, M. J. Janse, S. Tasseron, J. T. Vermeulen, N. de Jonge, and J. R. Lahpor, "Slow conduction in the infarcted human heart. 'Zigzag' course of activation." *Circulation*, vol. 88, no. 3, pp. 915–26, 1993.

124. X. Jie and N. Trayanova, "Mechanisms for initiation of reentry in acute regional ischemia phase 1B." *Heart Rhythm*, vol. 7, no. 3, pp. 879–86, 2010.

125. S. Rush and H. Larsen, "A practical algorithm for solving dynamic membrane equations." *IEEE Trans Biomed Eng*, vol. 25, no. 4, pp. 389–92, 1978.

126. R. Arnold, T. Wiener, D. Sánchez-Quintana, and E. Hofer, "Topology and conduction in the inferior right atrial isthmus measured in rabbit hearts," in *Conf Proc IEEE Eng Med Biol Soc*, 2011, pp. 247–250.

127. P. V. Bayly, B. H. KenKnight, J. M. Rogers, R. E. Hillsley, R. E. Ideker, and W. M. Smith, "Estimation of conduction velocity vector fields from epicardial mapping data." *IEEE Trans Biomed Eng*, vol. 45, no. 5, pp. 563–71, 1998.

128. R. O. Duda, P. E. Hart, and S. D. G., *Pattern Classification (2nd Edition)*. Wiley-Interscience, 2000.

129. A. Schlögl, J. Kronegg, J. Huggins, and S. G. Mason, "Evaluation Criteria for BCI Research," *In Toward Brain-computer Interfacing*, pp. 327–342, 2007.

130. CARP, "Cardiac Arrhythmia Research Package," http://carp.medunigraz.at/, 2007.

131. M. C. Maclachlan, J. Sundnes, and R. J. Spiteri, "A comparison of non-standard solvers for ODEs describing cellular reactions in the heart." *Comput Methods Biomech Biomed Engin*, vol. 10, no. 5, pp. 317–26, 2007.

132. J. Sundnes, G. T. Lines, and A. Tveito, "Efficient solution of ordinary differential equations modeling electrical activity in cardiac cells." *Math Biosci*, vol. 172, no. 2, pp. 55–72, 2001.

133. N. Corporation, "NVIDIA CUDA Programming Guide," 2009.

134. T. OpenMP API specification for parallel programming, "OpenMP," www.openmp.org, 2010.

135. R. M. Shaw and Y. Rudy, "Electrophysiologic effects of acute myocardial ischemia. A mechanistic investigation of action potential conduction and conduction failure." *Circ Res*, vol. 80, no. 1, pp. 124–38, 1997.

136. G. Plank and E. Hofer, "Use of cardiac electric near-field measurements to determine activation times." *Ann Biomed Eng*, vol. 31, no. 9, pp. 1066–76, 2003.

137. J. Daut and G. Elzinga, "Heat production of quiescent ventricular trabeculae isolated from guinea-pig heart." *J Physiol*, vol. 398, pp. 259–75, 1988.

138. B. Burstein and S. Nattel, "Atrial fibrosis: mechanisms and clinical relevance in atrial fibrillation." *J Am Coll Cardiol*, vol. 51, no. 8, pp. 802–809, 2008.

139. P. I. Gardner, P. C. Ursell, J. J. J. Fenoglio, and A. L. Wit, "Electrophysiologic and anatomic basis for fractionated electrograms recorded from healed myocardial infarcts." *Circulation*, vol. 72, no. 3, pp. 596–611, 1985.

140. G. Plank, E. Vigmond, L. J. Leon, and E. Hofer, "Cardiac near-field morphology during conduction around a microscopic obstacle–a computer simulation study." *Ann Biomed Eng*, vol. 31, no. 10, pp. 1206–12, 2003.

141. S. R. Kuo and N. A. Trayanova, "Action potential morphology heterogeneity in the atrium and its effect on atrial reentry: a two-dimensional and quasi-three-dimensional study." *Philos Transact A Math Phys Eng Sci*, vol. 364, no. 1843, pp. 1349–66, 2006.

142. S. V. Pandit, O. Berenfeld, J. M. Anumonwo, R. M. Zaritski, J. Kneller, S. Nattel, and J. Jalife, "Ionic determinants of functional reentry in a 2-d model of human atrial cells during simulated chronic atrial fibrillation." *Biophys J*, vol. 88, no. 6, pp. 3806–21, 2005.

143. W. H. Litchenberg, L. W. Norman, A. K. Holwell, K. L. Martin, K. W. Hewett, and R. G. Gourdie, "The rate and anisotropy of impulse propagation in the post-natal terminal crest are correlated with remodeling of cx43 gap junction pattern." *Cardiovasc Res*, vol. 45, no. 2, pp. 379–87, 2000.

144. M. O. Masuda and A. Paes de Carvalho, "Sinoatrial transmission and atrial invasion during normal rhythm in the rabbit heart." *Circ Res*, vol. 37, no. 7, pp. 414–21, 1975.

145. S. Rossi, S. Baruffi, A. Bertuzzi, M. Miragoli, D. Corradi, R. Maestri, R. Alinovi, A. Mutti, E. Musso, A. Sgoifo, D. Brisinda, R. Fenici, and E. Macchi, "Ventricular activation is impaired in aged rat hearts." *Am J Physiol Heart Circ Physiol*, vol. 295, no. 6, pp. H2336–47, 2008.

146. D. P. Zipes and H. J. Wellens, "What have we learned about cardiac arrhythmias?" *Circulation*, vol. 102, pp. IV52–7, 2000.

147. W. Chen, G. Aistrup, J. A. Wasserstrom, and Y. Shiferaw, "A mathematical model of spontaneous calcium release in cardiac myocytes." *Am J Physiol Heart Circ Physiol*, vol. 300, no. 5, pp. H1794–805, 2011.

148. Y. Xie, D. Sato, A. Garfinkel, Q. Z, and J. N. Weiss, "So little source, so much sink: requirements for afterdepolarizations to propagate in tissue." *Biophys J.*, vol. 99, no. 5, pp. 1408–15, 2010.